CHAPTER 3

DATA ANALYSIS

3.1 Overview

Data were taken in experiment E154 in October and November of 1995. The deep inelastic data were taken at the beam energy of 48.3 GeV and at three nominal beam currents: $3 \cdot 10^{10}$, $5 \cdot 10^{10}$, and $9 \cdot 10^{10}$ electrons per pulse. Nine polarized target cells and four reference cells were used through the course of the experiment. The typical electron rate was 0.5 electrons per pulse in the 2.75° spectrometer and varied from 0.07 to 0.2 electrons per pulse in the 5.5° spectrometer. The data were collected in runs which were each typically 200,000 spills long (or approximately half an hour). The data set consisted of more than 1800 runs that included asymmetry data (in parallel and perpendicular target polarization configurations), reference cell runs to determine the dilution factor, runs with the magnet polarity reversed to measure the charge symmetric backgrounds, and miscellaneous calibration and test runs. About 1.4 TBytes of data were stored on magnetic tapes. After all cuts, about 100 million deep inelastic events were used in the analysis.

The analysis was done in two steps. First, the raw data tapes were analyzed and the Data Summary Tapes (DSTs) were produced. The DST tapes contained the information about the Cherenkov hits, shower clusters, and tracks found in each spectrometer, as well as beam information. The DST production took seven weeks on four DEC Alpha 600 5/266 computers. A separate program was used to process the DST tapes and place electron events in x and Q^2 bins for each beam helicity. The summary files produced in this process were used to calculate the physics asymmetries and structure functions.

The analysis was done independently by two groups based at SLAC and Caltech[1]. The results of both groups agree to a very high degree, and for the publications we have chosen to average the results of two groups. We will primarily present the analysis and results obtained at Caltech, and describe the main differences with the SLAC analysis. After first describing the analysis of the raw data, our attention will be turned to the DST analysis and physics results.

3.2 Coordinate system

In the following discussion, we will use the "analysis" coordinate system that is related to the central trajectory in the spectrometer. This is a natural system since trajectories of all particles in the detector hut are roughly symmetric around the central ray. The $\hat{z}$ axis of the analysis frame coincides with the central ray in the detector hut which is pitched up by $\phi_{\rm cr} = 0.81°$ (2.65°) and offset down by $\Delta y_{\rm cr} = 104.9$ cm (114.3 cm) in the 2.75° (5.5°) spectrometer relative to the regular "spectrometer" system (*cf.* Section 2.6.2). The rotation is around the $\hat{x}$ axis, so it is the same in both frames. The origin of the is chosen in such a way that the target is at $z = 0$ in the new frame. Hence, the transformation from the spectrometer to the analysis frame is given by

$$\begin{pmatrix} x \\ y \\ z \end{pmatrix}_{\rm analysis} = \begin{pmatrix} 1 & 0 & 0 \\ 0 & \cos\phi_{\rm cr} & -\sin\phi_{\rm cr} \\ 0 & \sin\phi_{\rm cr} & \cos\phi_{\rm cr} \end{pmatrix} \begin{pmatrix} x \\ y \\ z \end{pmatrix}_{\rm spec} + \begin{pmatrix} 0 \\ \Delta y_{\rm cr} \\ 0 \end{pmatrix} . \qquad (3.1)$$

Two coordinate systems are illustrated in Fig. 3.1.

3.3 Cherenkov analysis

In E154, each of the four Cherenkov counters was equipped with a Flash ADC (FADC) to digitize the phototube pulses. The four channels of the FADC, running

[1]The "off-site" analysis based at Caltech was a collaborative effort of physicists from Caltech, UMass, Princeton, Syracuse University, and Temple University.

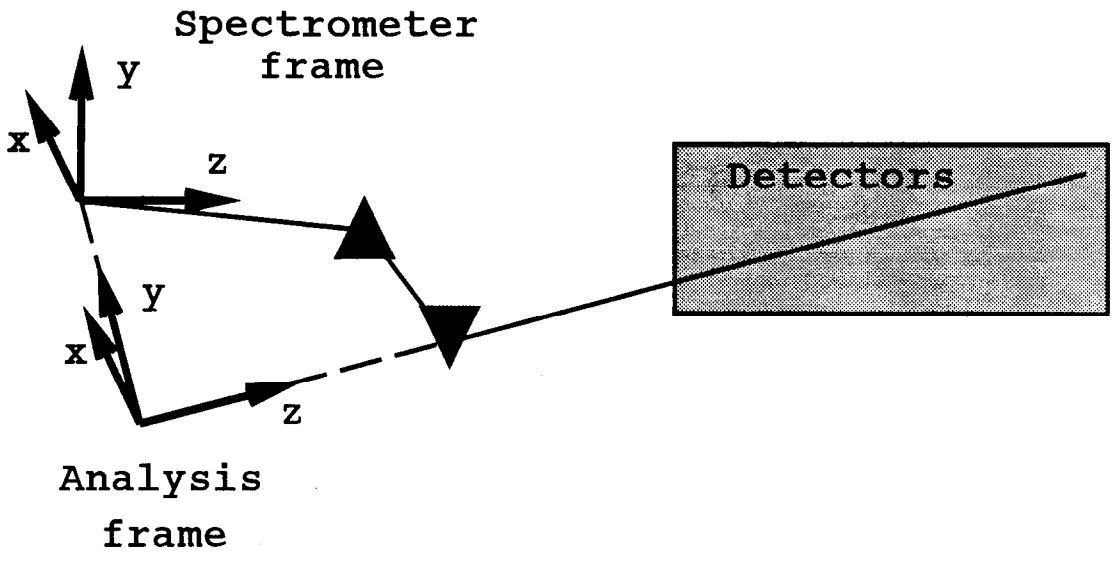

Fig. 3.1. The "spectrometer" and "analysis" coordinate systems. The prisms denote the dipole magnets.

with internal clock frequency of 250 MHz, were interleaved to produce effective time bins of 1 nsec. An example of the waveform recorded by a Flash ADC is shown in Fig. 3.2. The primary purpose of the Cherenkov code was to single out separate phototube pulses and determine their time and amplitude (or total charge) which is proportional to the total number of photoelectrons emitted from the cathode of the phototube.

A brief outline of the algorithm follows. First, we calculate the time derivative of the waveform and find all local maxima. Then, we determine the flat background for the waveform in the regions sufficiently far from all pulses and subtract it from the waveform. For each pulse found, we determine the pulse height (later to be related to the number of photoelectrons) and integrate the pulse to find the total charge. Corrections are made, if necessary, to account for saturated pulses (pulses higher than FADC range of 255 bits (about 2 V) are truncated to 255 bits), truncated pulses (that are late in the spill so the full charge is not recorded), and overlaps. The time

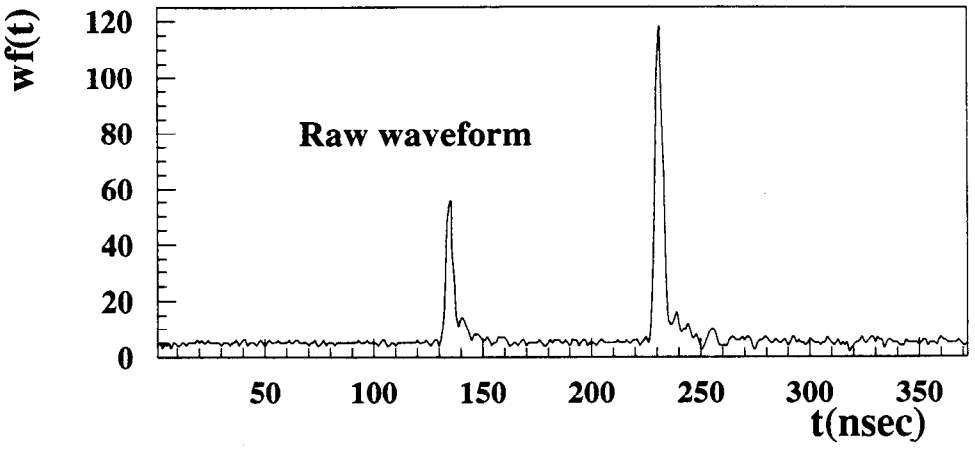

Fig. 3.2. A typical event (spill) in the Cherenkov detector recorded by a Flash ADC.

of the pulse is determined by the time at the half height. The average signal shape, scaled by the height of the processed pulse, is used to separate overlapping pulses.

The time resolution of the Cherenkov FADCs was found to be $\approx$ 1.3 ns (see Fig. 3.3, left). This is quite below par for the Hamamatsu R1584-01 phototubes, and is explained by the time jitter of the FADC clock. The clocks of each FADC, running at 250 MHz, were not synchronized. This produced a random jitter of 4 nsec and contributed $\approx 4/\sqrt{12} = 1.2$ nsec[2] to the time resolution. The solution,[113] implemented in the Caltech analysis[3], was to use TDCs clocked at 1 GHz to synchronize the FADCs. The resolution improved to $\approx$ 0.8 nsec (Fig. 3.3, right), reducing the accidental background in tracking and thus helping to reduce the pion contamination.

The algorithm was found to be reasonably robust with an intrinsic dead time of less than 5 nsec. A typical response of a Cherenkov counter to electrons and pions is shown in Fig. 3.4. The response to electrons (the average number of photoelectrons)

[2]We here loosely use the RMS of the uniform distribution that is given by $4/\sqrt{12}$ for a fixed width of 4.

[3]The problem was solved too late to be implemented in the SLAC DST production.

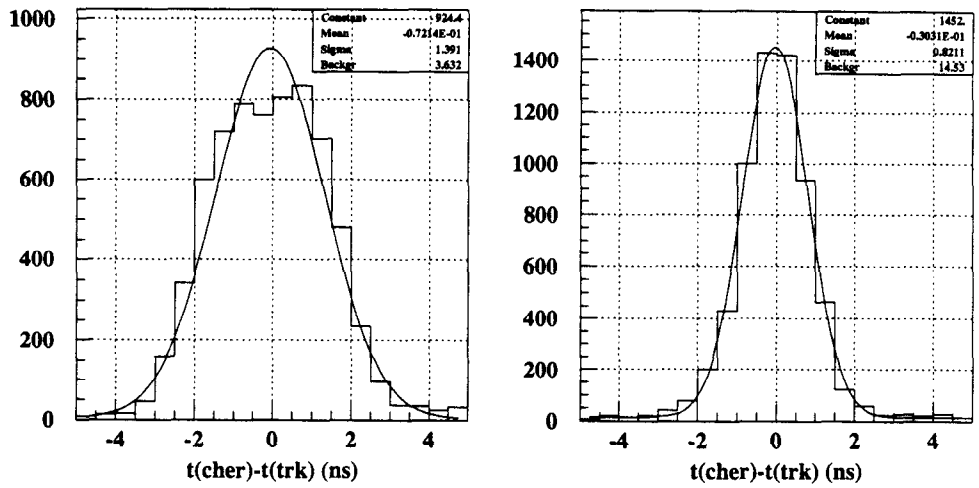

Fig. 3.3. Time resolution for a FADC alone (left), and for a FADC with TDC synchronization (right).

Table 3.1. Average Cherenkov response to electrons.

Tank	2C1	2C2	5C1	5C2
# of photoelectrons	5.7	5.1	6.2	5.0
C_{v2pe}	16.8	14.1	12.1	13.6

of all counters is summarized in Table 3.1.[114] The relation between the Cherenkov peak voltage and number of photoelectrons is given by

$$V_{\text{peak}} = C_{\text{v2pe}}(\text{tank})PE\ , \tag{3.2}$$

where coefficients C_{v2pe} are also given in Table 3.1.

The Cherenkov efficiency for electrons was found to be $\approx 95\%$[115] and was limited by the intrinsic pulse height cutoff of the algorithm (4–6 FADC units) and Cherenkov dead time. Efficiency for a typical Cherenkov cut used in the analysis (see Section 3.7.3.2) is about 90%.

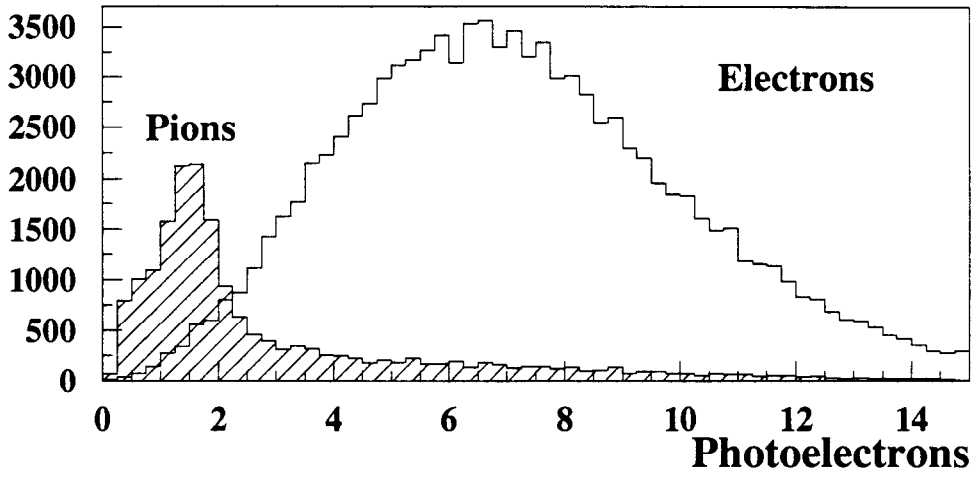

Fig. 3.4. Typical Cherenkov response to electrons (open) and pions (hatched).

3.4 Shower analysis

3.4.1 Introduction

The shower code is one of the major parts of the raw analysis that was different from the one used in the SLAC DST production. The shower counters provide electron identification via energy, E/p, and shower profile (shape, neural net) cuts. The cluster information is the basis for the tracking algorithm (see Section 3.5); in addition, the shower position resolution directly affects momentum and angular resolution. The shower analysis meets certain challenges in the high rate environment of E154 due to the overlaps of the electron and pion clusters (Fig. 3.5). Such overlaps create rate-dependent biases in energy and position reconstruction and calorimeter-based electron identification, and thus have a potential to alter experimental asymmetries. It is important to have an analysis algorithm that is robust in the high rate environment; it is also necessary to study and correct for any possible rate dependence.

The code benefited greatly from the experience with the existing SLAC code.[116] At the same time, it was an entirely new code, and therefore provided an important

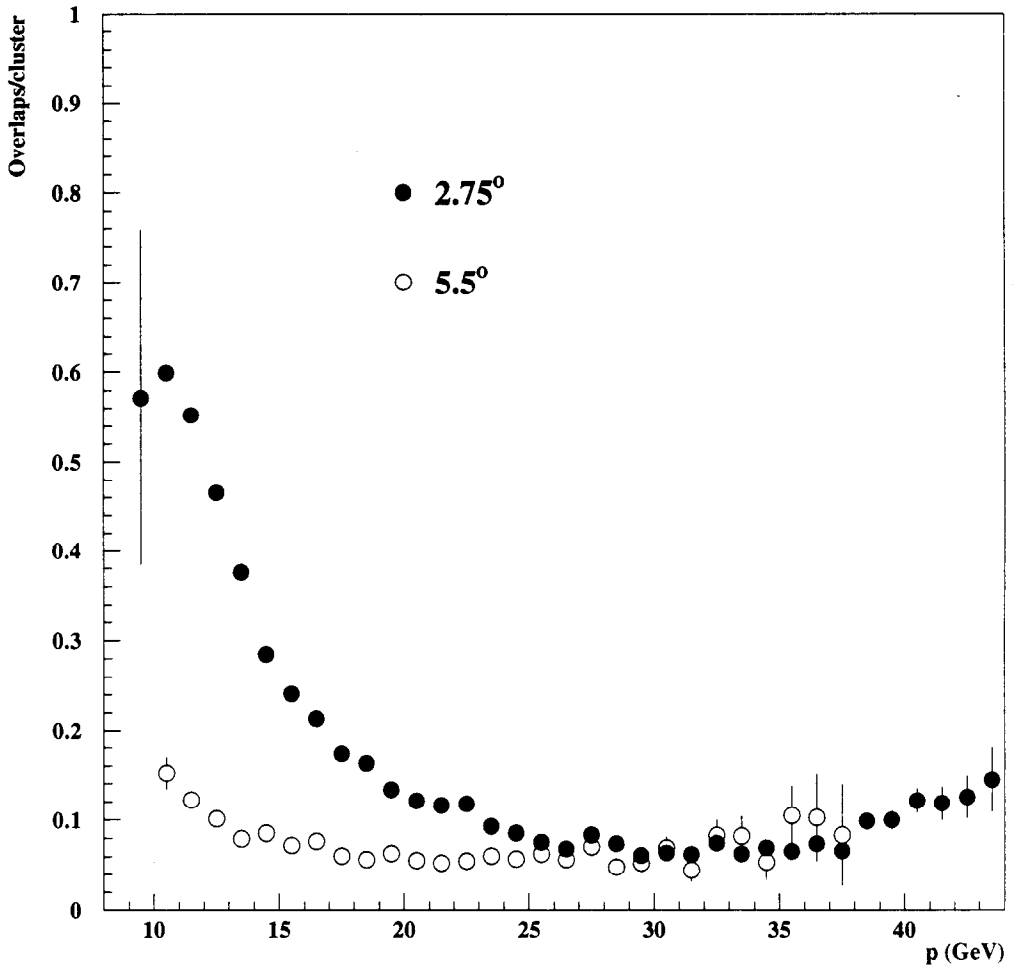

Fig. 3.5. Number of overlaps per electron cluster versus momentum of the electron in 2.75° (closed circles) and 5.5° (open circles) spectrometers for the typical running conditions (run 3366, beam current of $5 \cdot 10^{10}$ electrons/spill). A sharp rise at low momenta corresponds to increasing pion production rate.

cross-check of the existing algorithm. In addition, the spatial and timing resolutions were improved, and biases in the cluster position and energy reconstruction were eliminated. Also, as an alternative to the neural network used in the SLAC analysis, a particle identification (ID) method based on the information about the lateral shower profile was developed (the "shape cut"). The clustering algorithm and the shape analysis will be discussed in the following pages.

In this Section, we follow the definitions adopted in the SLAC shower code.[116,117] An elementary *cell* is a signal induced by one particle in one block. Each cell is characterized by its *time* and *energy*. We record times of both leading (LE) and trailing edges (TE) of the photomultiplier pulses. Cell time is determined by its LE time. Cell energy is determined by the difference between TE and LE times as will be discussed below. Energies of all cells in one block always add up to the total energy deposited in that block in one spill. If a block does not have any TDC hits within one spill, we create one cell which carries full energy deposited in the block; the time of such a cell is undefined. A cell with a definite time is required to have a LE, but it does not always have a TE (misses of TE happen less than 1% of the time). A *cluster* is a collection of cells with common time that are grouped according to the set of rules to be discussed below.

3.4.2 Clustering algorithm

3.4.2.1 5×5 *clusters*

Contrary to the standard SLAC analysis which employs the *cellular automaton*[118] technique, we have chosen a simpler and faster method sometimes referred to as "vector approach".[118] As a first step, after the data from the TDCs and ADCs are copied into the local common blocks, we search the 10×20 shower array for the local energy maxima ("central blocks") that pass the following criteria:

1. There is at least 1 TDC hit in the central block;

2. The sum over 9 blocks around the central block

$$\sum_{3\times3} E_i > E_{cut} = C_{\rm cut} p_{\rm min}({\rm row}).$$

The first requirement ensures that the cluster candidate has timing information. Electron energy deposition in the central block is always higher than the TDC threshold; the lack of a timing hit signals either a DAQ failure or an event affected by an overlap. Such clusters cannot be used in the further analysis. The second requirement provides a simple and effective pion rejection at the very early stage of the analysis. The value $p_{\rm min}({\rm row})$ is determined by the lowest momentum of electrons that hit the particular block after passing through the spectrometer. This value is in principle different for every row (and is increasing from top to bottom of the calorimeter). In practice the value of 9 GeV was used for every block. The constant $C_{\rm cut}$ was chosen to be 0.7, safely below any reasonable E/p cut value[4]. Thus, most pions that deposit energy of less than 6.3 GeV are cut before the main clustering and tracking started, significantly reducing the precessing time.

Having found the central block, we share its energy among its cells. The cluster is started with the highest energy cell of the central block. We add to the cluster cells from the surrounding 5×5 matrix that

- among 8 blocks closest to the center and
  1. Are in time with the central block, or
  2. Have no TDC hits
- among the outer 16 blocks and
  1. Are in time with the central block, or
  2. Have no TDC hits and no other cluster nearby

[4]For the dedicated pion DST production, this value was lowered to 0.05.

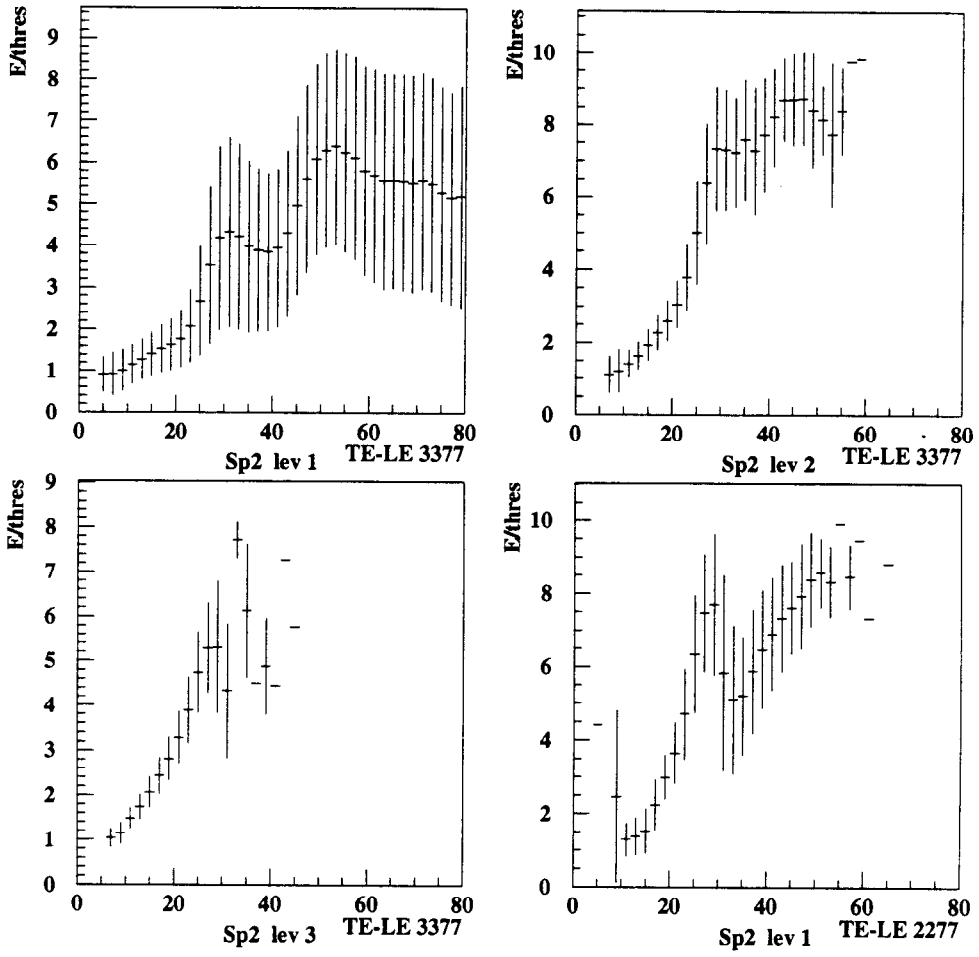

Fig. 3.6. The pulse height as a function of the difference between the leading and trailing edge times for different discriminator levels. The error bars represent the RMS of the distribution.

The time window is set to be $|\Delta t| \leq 5$ nsec.

3.4.2.2 Energy sharing

When two or more particles hit one block, energies are added in the ADC. To separate them, we use the correlation between the pulse height and the time difference between the leading (LE) and trailing edges (TE) of the pulse (Fig. 3.6). For all pairs of leading and trailing edges (*cells*), we calculate the expected energy

$e_i = f(t_i^{TE} - t_i^{LE})$ and error σ_i. We then minimize

$$\chi^2 = \sum_i \left(\frac{E_i - e_i}{\sigma_i} \right)^2 \tag{3.3}$$

with a constraint

$$\sum_i E_i = E_{tot} \,, \tag{3.4}$$

where E_{tot} is the full energy deposit in the block, and solve for cell energies E_i. The benefit of such an approach is obvious. For any TDC level, the dynamical range for the energy sharing is limited; from Fig. 3.6 one can see that the meaningful information can only be extracted if the ratio of the pulse height to threshold $E/E_{thres} \leq 4$. Electron pulses are often much higher than that, especially for the low thresholds [5]. Pion pulses, on the contrary, are predominantly small. Thus, combining the pion and electron information reduces the error in electron energy determination. This is important to minimize the rate dependence associated with the E/p cut.

3.4.2.3 Cluster time and position

An energy-weighted average used by SLAC analysis

$$x = \frac{\sum_{blocks} x_i E_i}{\sum_{blocks} E_i} \tag{3.5}$$

is known[119] to give a biased estimate of the cluster position due to the relatively coarse transverse segmentation of the calorimeter. It results in a bias towards the coordinate of the central block, as could be clearly seen in Fig. 3.7 which shows the difference between the cluster position and the position of an associated track for the SLAC code. The position offset is as large as 1 cm, and maximizes when electrons hit the boundary of the block ($x_{\rm tr} - x_{\rm sh} = \pm 32$ mm). Alternatively, we

[5]The values of the discriminator thresholds are summarized in Table 3.2. Note the thresholds were set in mV, and the spread of thresholds in GeV corresponds to the spread of calibration constants.

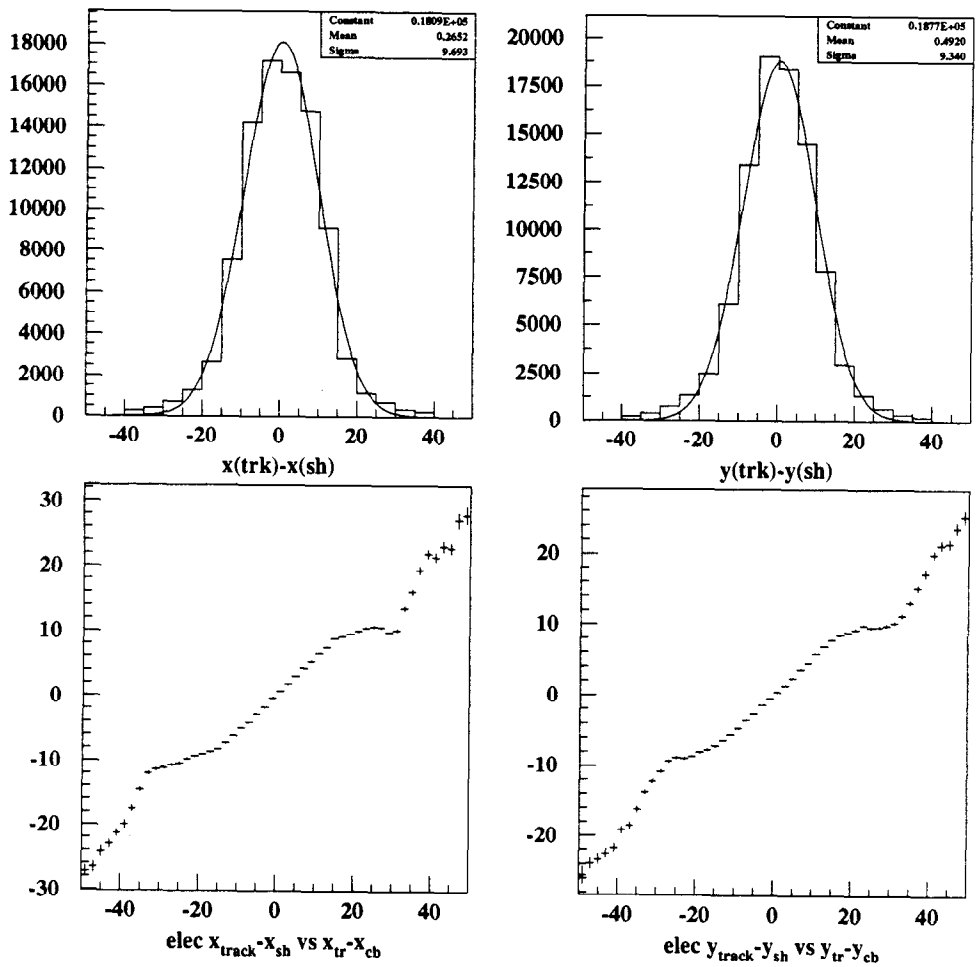

Fig. 3.7. Performance of the SLAC shower code. (top) Shower position resolution. (bottom) Cluster spatial offset versus the position of the track relative to the center of the central block. All numbers are in mm.

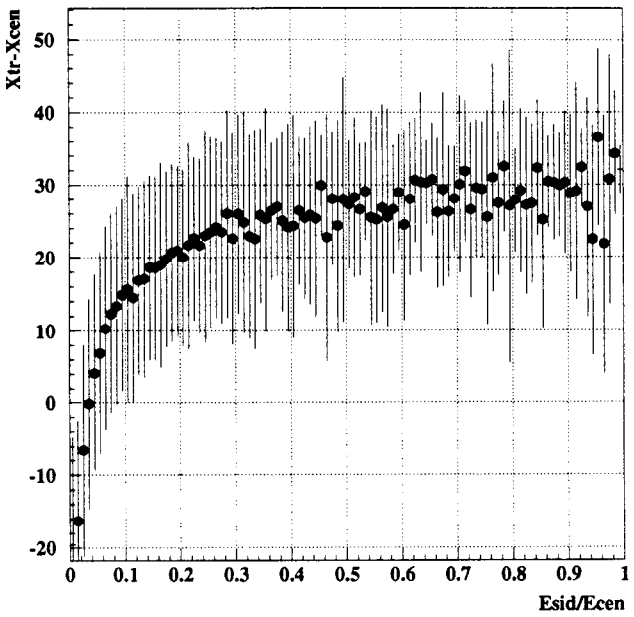

Fig. 3.8. Cluster position versus the ratio of energies in the side and central blocks. Error bars represent the RMS of the distribution.

(5.5°), and in y direction the resolution is 7.5 mm (2.75°) and 7.9 mm (5.5°). This is to be compared to $\sigma_x = 9.7$ mm and $\sigma_y = 9.3$ mm for the SLAC code (see Fig. 3.7, top). The improvement in the position resolution results in a better angular and momentum resolution (see Section 3.5). Note that the resolution was determined by comparing the coordinate of the shower cluster with the coordinate of the electron track at the z position of the shower counter. The tracking spatial resolution without cluster constraints (*i.e.* for class 3 tracks used to determine the resolution) is expected to be $4-5$ mm at the shower counter, so the actual position resolution of the clustering might be even better than the numbers quoted above. The wings of the distribution are due to effects of accidental and correlated (delta rays) backgrounds in tracking. Figure 3.10 shows the distribution of the electron clusters in the calorimeter and the difference between the track position and the cluster position plotted versus the position of the track. Notice that there are no significant biases in either x or y direction (*cf.* Fig. 3.7, bottom).

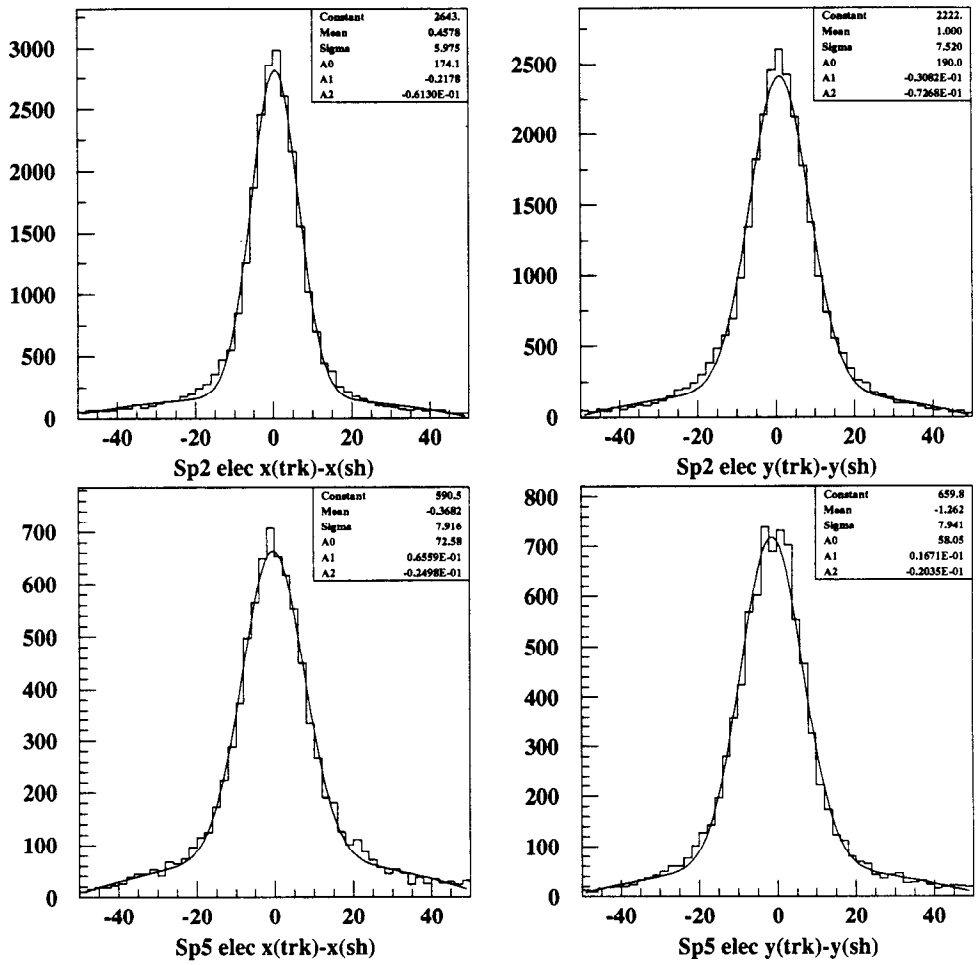

Fig. 3.9. The position resolution for electrons in 2.75° (top) and 5.5° (bottom) calorimeters. The fit is Gaussian with quadratic background. All numbers are in mm.

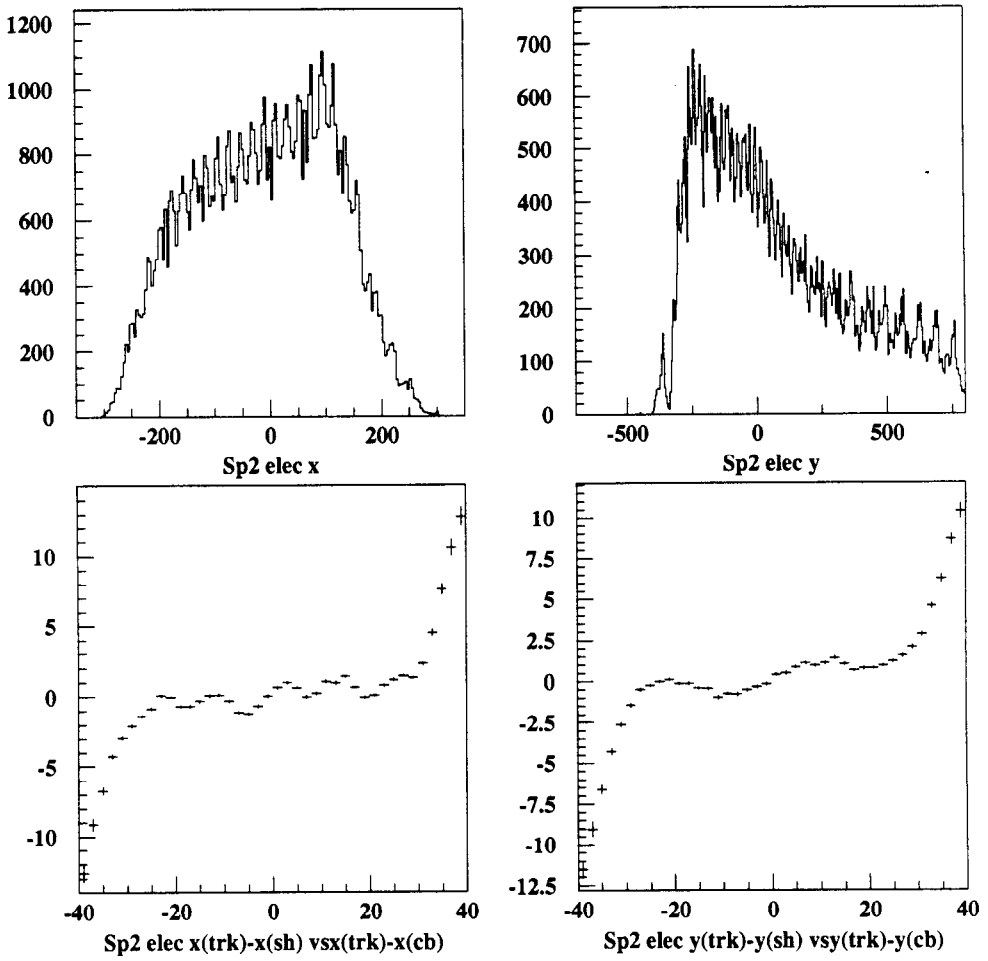

Fig. 3.10. (top) Cluster position distribution in the 2.75° shower counter for Caltech analysis. (bottom) The cluster spatial offset versus the position of the track relative to the center of the central block. The error bars are statistical.

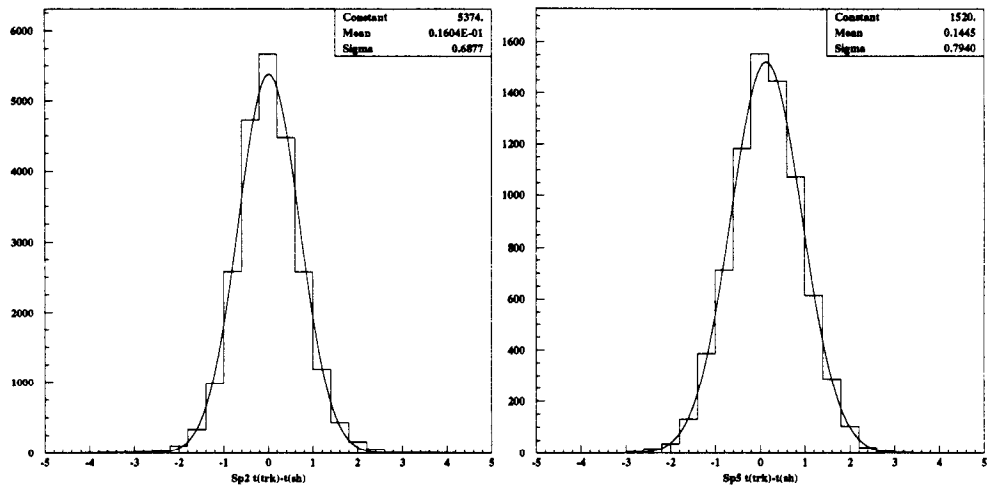

Fig. 3.11. Time resolution (in ns) for electrons in 2.75° (left) and 5.5° (right) calorimeters. The fit is gaussian.

The time of the cluster was determined by averaging TDC times of all blocks for which the energy deposited was at least 10% of the central block energy:

$$t = \frac{\sum_i t_i/\sigma^2(t_i)}{\sum_i 1/\sigma^2(t_i)} , \tag{3.7}$$

where $\sigma(t_i)$ is the time uncertainty for each block. The energy cut minimized the effect of timing jitter for the small pulses. Another potential problem with using blocks with small energy deposit is that they are usually on the tails of the shower and the effective z position of the particles in the shower tail is significantly deeper than the core of the shower. The light from the shower tails reaches the phototube earlier than the light from the core (since the shower develops with the speed of light in the vacuum c whereas the light propagation speed is c/n with the index of refraction $n = 1.62$. The energy cut minimizes this effect so no correction is necessary.

The time resolution of both calorimeters is shown in Fig. 3.11. With the technique described above we achieved the resolution of $\approx$ 0.7 nsec (for electrons), compared to $\approx$ 0.9 nsec for the SLAC code.

3.4.2.4 Shower shape

The differences in the transverse profiles of the showers produced by electrons and pions (to which we will loosely refer as electron or pion "shapes") are frequently used to separate the particles in the electromagnetic calorimeter. While the electrons develop electromagnetic showers, the pions undergo the strong interactions that lead to the hadronic showers, wider and less symmetric than electromagnetic ones. Charged pions may also convert to the neutral pions via the charge exchange $\pi^- p \rightarrow \pi^0 n$, where the π^0 decays instantly into two photons. In that case the shower is electromagnetic and its profile is almost indistinguishable from the electron shower. However, even in this case (and in case of the hadronic showers), pions rarely deposit their full energy in the electromagnetic form, and a simple E/p cut can be used to separate them from electrons.

The standard measure of the electromagnetic shower cross section is the scaling variable referred to as the Moliére radius R_m[119]; for ASP(F2) lead glass used in our calorimeters $R_m \approx 5$ cm. For electromagnetic showers, 90% and 95% of the shower energy are contained in the cylinders with radii R_m and $2R_m$ respectively. A simple approximation of the lateral shower profile is a single-exponential form[119]

$$A(R) = A(0)\exp(-R/R_0)\ , \tag{3.8}$$

where R is the transverse shower dimension and $R_0 = 0.25R_m$ is the damping constant. A more realistic model is a double-exponential shape[120]

$$A(R) = A_1\exp(-R/R_1) + A_2\exp(-R/R_2)\ , \tag{3.9}$$

where the first exponent describes the narrow shower core, and the second corresponds to a longer tail of soft electrons and photons. For a finite calorimeter block of size $2s$, one can calculate the energy deposited from the shower centered at (x_0, y_0):

$$E = E_0 \int_{-s}^{s}\int_{-s}^{s} dxdy\, a\left(\sqrt{(x-x_0)^2+(y-y_0)^2}\right)\ , \tag{3.10}$$

Table 3.4. Parameters of the shower shape in Eq. (3.11).

s (mm)	h	r	R_1 (mm)	R_2 (mm)	p
34.0	0.872	0.3	4.0	19.0	2.9

where $a(R)$ is a normalized shower profile of Equations (3.8) or (3.9) and E_0 is the total cluster energy. The resulting distribution is fitted to the following functional form:

$$\frac{E}{E_0} = \mathcal{S}(x - x_0, y - y_0) = \begin{cases} h\{\,[1 - \exp(-s/R_1)\cosh(d/R_1)] + \\ \quad r[1 - \exp(-s/R_2)\cosh(d/R_2)]\,\} & |d| \le s \\ h\{\,\sinh(s/R_1)\exp(-d/R_1) + \\ \quad r\sinh(s/R_2)\exp(-d/R_2)\,\} & |d| > s\,, \end{cases} \tag{3.11}$$

where

$$d = (|x - x_0|^p + |y - y_0|^p)^{1/p}\,, \tag{3.12}$$

(x, y) is the center of a given block, and (x_0, y_0) is the shower position. The electron shower profile is shown in Fig. 3.12. The parameters of Eq. (3.11) are given in Table 3.4. The pion hadronic showers are wider on average (Fig. 3.12), and the individual pion clusters are much less symmetric than the electron ones.

3.4.2.5 Iterating the cluster shape

The energy sharing using the LE and TE information is not always perfect. First of all, it has a limited dynamic range. Pions with energy deposit below threshold are not detected by TDCs. Secondly, if electron energy deposit in one block is much bigger than the threshold, the time information is not reliable and leads to large errors in energy sharing. The latter effect is potentially more important: if the energy of the cluster is underestimated due to energy sharing, the event may not pass the E/p cut (typically, $E/p > 0.8$ cut is a part of electron definition). Another important factor is the cluster position bias due to overlaps that translates into the error in

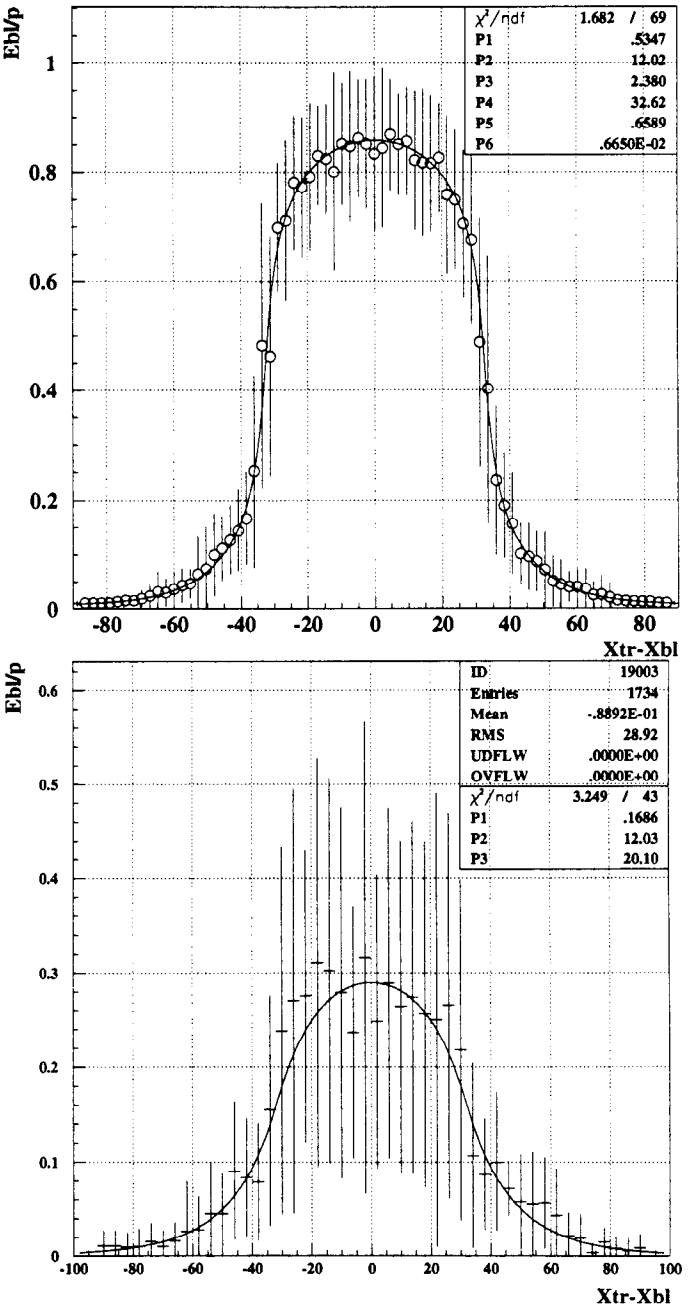

Fig. 3.12. Average shapes of the showers for electrons (top) and pions (bottom). Error bars represent the spread of the distributions.

momentum reconstruction. All these effects are rate-dependent and thus can bias the measured asymmetry.

In order to further reduce the rate-dependent effects in the cluster energy and position reconstruction, we developed an iterative procedure using the typical electron shape of Eq. (3.11)[6]. It works in two steps. First, we calculate the cluster position (x_0, y_0) using Eq. (3.6) and the initial estimate of the cluster energy

$$E^{(0)} = \frac{E_c}{\mathcal{S}(x_c - x_0, y_c - y_0)} , \tag{3.13}$$

where E_c and (x_c, y_c) are the energy and position of the central cell. We then calculate

$$\chi^2 = \sum_i \left(\frac{E_i^{(0)} - E^{(0)}\mathcal{S}(x_i - x_0, y_i - y_0) - E_{\text{back}}}{\sigma_i} \right)^2 \tag{3.14}$$

where the sum is over all cell in the cluster. Here $E_i^{(0)}$ is the initial energy of each cell determined as described in Section 3.4.2.2. $E_{\text{back}} = 50$ MeV is the average background noise, and σ_i is the uncertainty of the block energy given by

$$\sigma_i^2 = a^2 + \left(bE_i + c\sqrt{E_i} \right)^2 + \sigma_{\text{share}}^2 , \tag{3.15}$$

where σ_{share} is the uncertainty in energy sharing. A fit to the data yields $a = 0.15$ GeV, $b = 0$, and $c = 0.2$.

Minimizing χ^2, we find a new estimate of energy $E = E^{(1)}$ and position $(x_0, y_0)^{(1)}$ (we linearize the problem by treating $\Delta x = x_0^{(1)} - x_0^{(0)}$ as a perturbation). The energies of each cell E_i are allowed to vary within their uncertainties. The cell is "frozen" (*i.e.* its energy is fixed) if change in its energy exceeds the uncertainty. The χ^2 minimization is repeated with new cell energies $E_i^{(1)}$. The iterations converge if one of the following conditions is met:

- Cluster position does not change

[6]It is not used for special pion DST production.

- All cells are frozen
- Number of iterations exceeds 10

The convergence is typically achieved in 1–2 iterations. Cluster position $(x_0^{(n)}, y_0^{(n)})$ and its uncertainty are copied to the output common block and used in tracking.

After a track has been associated with the cluster, the electron coordinates at the shower counter are determined quite accurately. We can now fix the cluster position (x_0, y_0) in Eq. (3.14) to be the track position at the shower counter, and minimize shape residuals varying only the cluster energy E.

3.4.2.6 Energy measurement

Three energy variables and corresponding uncertainties are reported by the shower code and are written to DSTs:

- $\mathbf{E_9}$: Sum of cells in 3×3 matrix around the central block.
- $\mathbf{E_4}$: Sum of four most energetic blocks in the cluster (the central block, the most energetic blocks in x and y directions, and 1 diagonal block). The sum is scaled by a factor of 1.05 to normalize it to E_9.
- $\mathbf{E_1}$: energy determined in iterative process (after tracking).

The ratios E_1/E_9 and E_4/E_9 and their momentum dependence are shown in Fig. 3.13. E_9 is a basic energy definition and is used for shower calibration. The advantage of E_4 and E_1 over E_9 is reduced sensitivity to overlaps. E_4 samples a smaller number of blocks than E_9 and therefore the pileup probability for E_4 is lower. The drawback is that E_4 is an approximation that is reasonably good up to energies of ≈ 30 GeV. At higher energies, the shower broadens and energy deposit into other blocks of the 3×3 matrix becomes increasingly important. This is evident from Fig. 3.13:

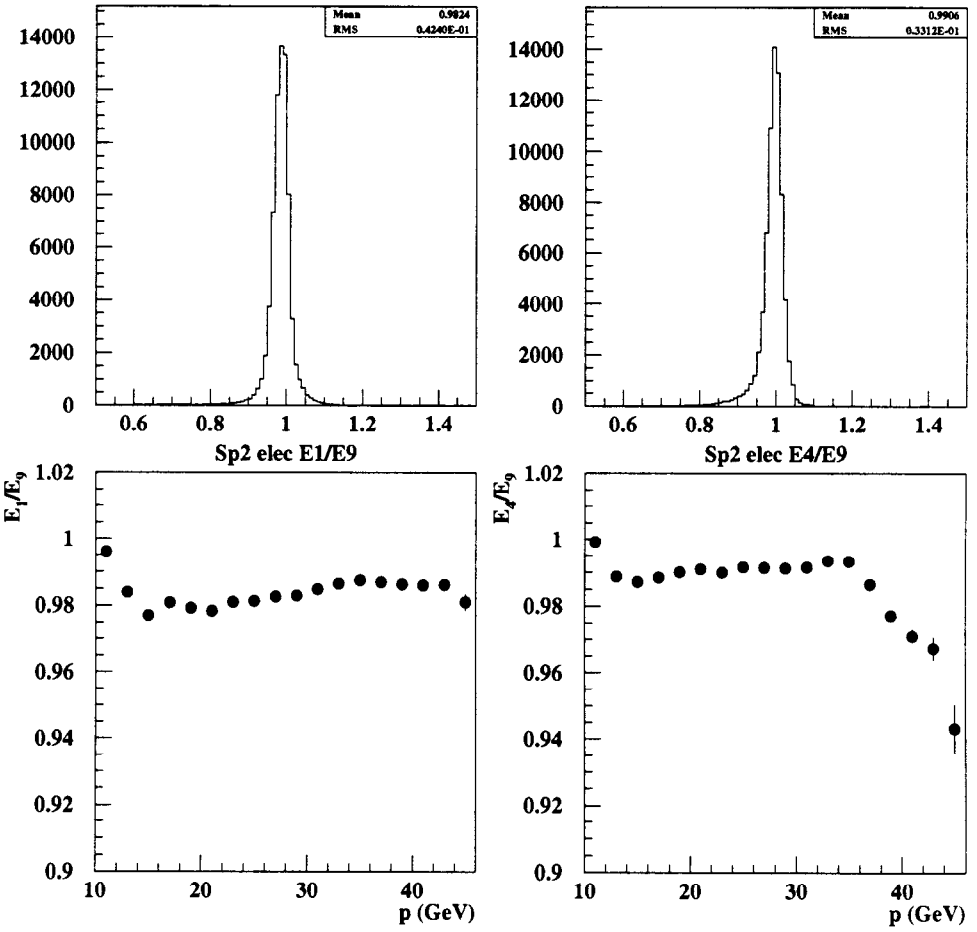

Fig. 3.13. Ratios of energies E_1/E_9 (top, left) and E_4/E_9 (top, right) and their momentum dependence (bottom).

the ratio E_4/E_9 deviates significantly from 1 starting at $p \approx 30$ GeV. The iterated energy E_1 does not exhibit such a behavior (Fig. 3.13).

The shower counter blocks were calibrated using a sample of electrons identified by a high threshold cut in the Cherenkovs. Low rate runs (empty reference cell runs at $\approx 1 \cdot 10^{10}$ electrons/pulse beam current) were used to minimize the rate-dependent effects. The calibration constants were adjusted interatively until the mean of the Gaussian fitted to the distribution of the ratios E_9/p reached unity for every block. This method could not be directly applied to the the blocks on the edges of the calorimeter and blocks with low phototube gain. For the edge blocks, we used the ratio E_4/p which is less sensitive to the leakage of the shower outside the detector. We also used a clean sample of muons and pions that do not produce a shower in the calorimeter. Such particles leave a single Cherenkov track in one shower block, and are seen as a monochromatic line with $E = 0.92 \pm 0.15$ GeV in our calorimeter.

Figure 3.14 shows the ratio E/p for electrons in both spectrometers. Left plots correspond to E_9 energy, and right plots are for E_1 energy. The energy resolution is comparable to that of the SLAC code. In Fig. 3.15 we show the ratio E_1/p in the 2.75° calorimeter for four special cases: clusters with no overlaps (top left), clusters with an overlap in any of the blocks (top right), clusters in overlaps in the central block (bottom left), and clusters with the central block on the edge of the calorimeter. No significant degradation of energy resolution and no significant bias is observed for either case. Fig. 3.16 shows the same plots for the low x (2.75° spectrometer, $9 < p < 12$ GeV). Again, energy determination is reasonably stable.

3.4.3 Shape cut

The difference between pion and electron shapes (Fig. 3.12) can be used to separate electrons from pions using only shower counter information. The SLAC analysis uses the algorithm based on a multi-layered neural network.[118,121] A set of input parameters (discriminating variables), e. g. energy deposited in each cluster

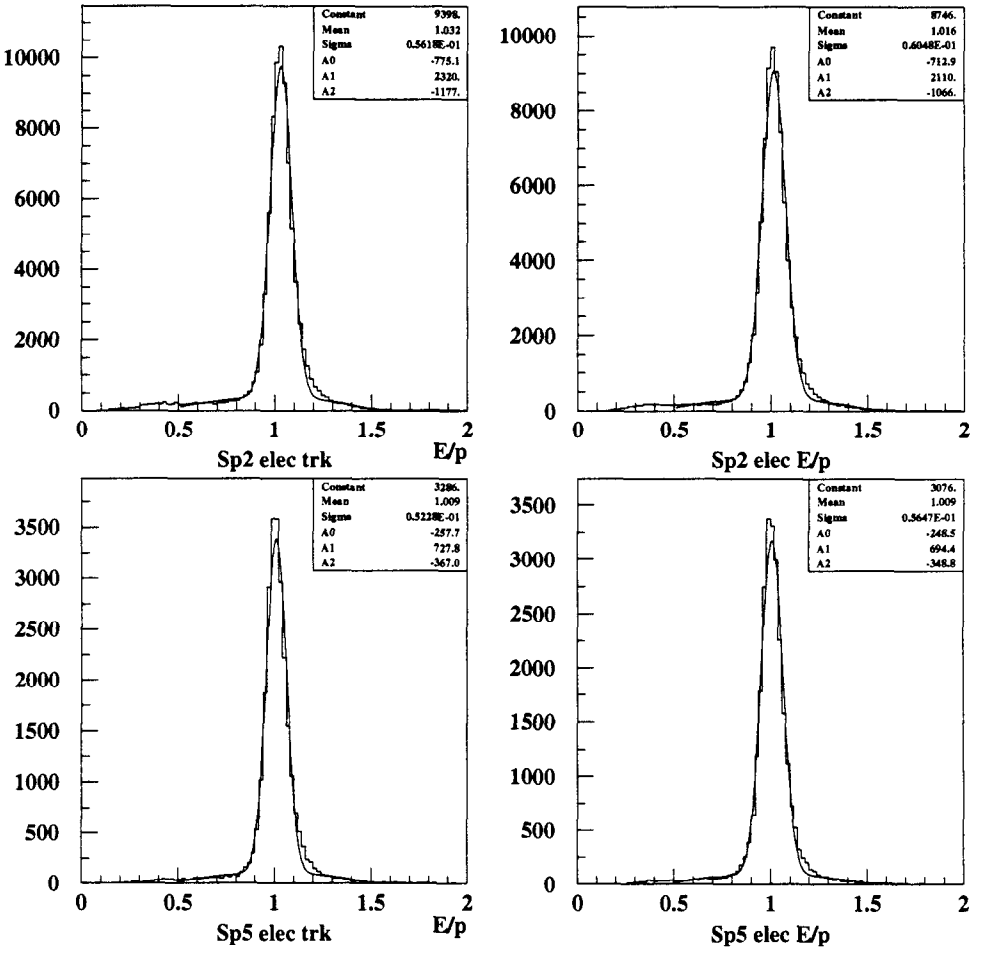

Fig. 3.14. Ratios E_9/p (left) and E_1/p (right) for electrons in 2.75° (top) and 5.5° (bottom) spectrometers. The fit is gaussian with quadratic background.

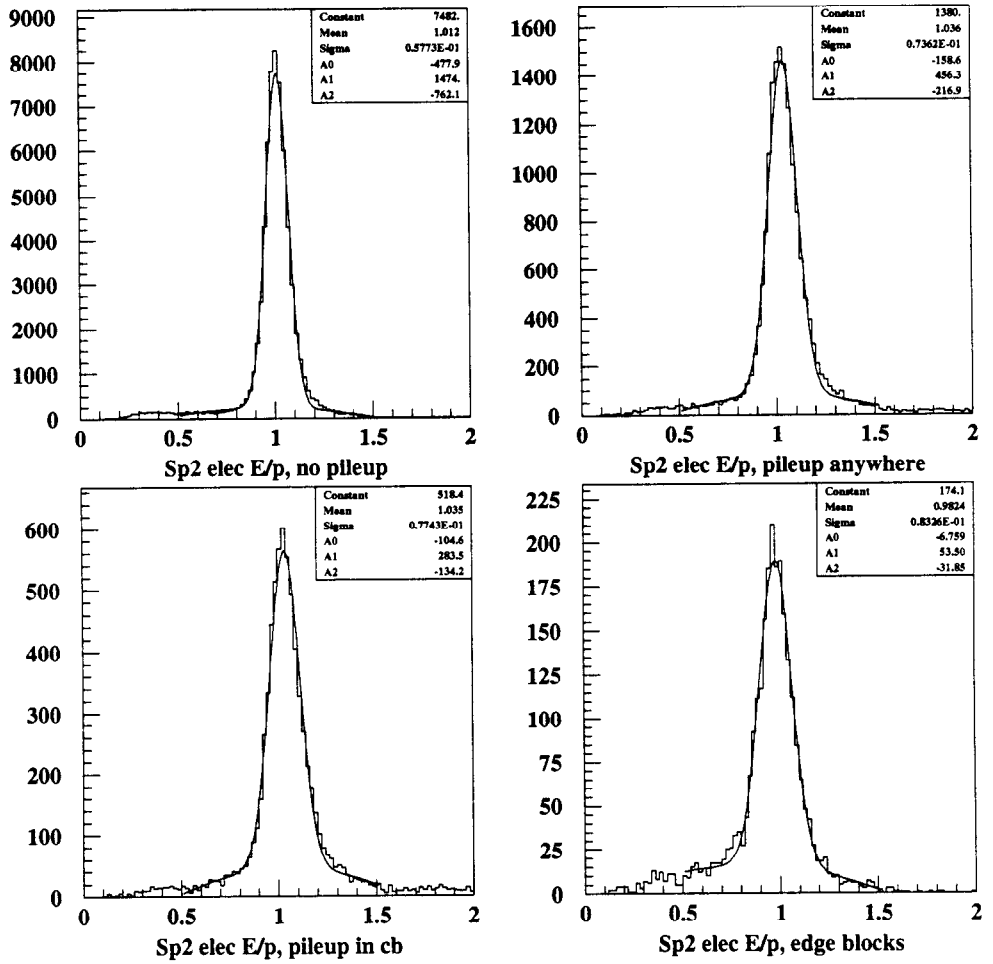

Fig. 3.15. Ratios E_1/p for electron clusters in 2.75° counter with (top left) no overlaps, (top right) overlaps in any of the cluster blocks, (bottom left) overlaps in central block, (bottom right) clusters with the central block on the edge of the calorimeter.

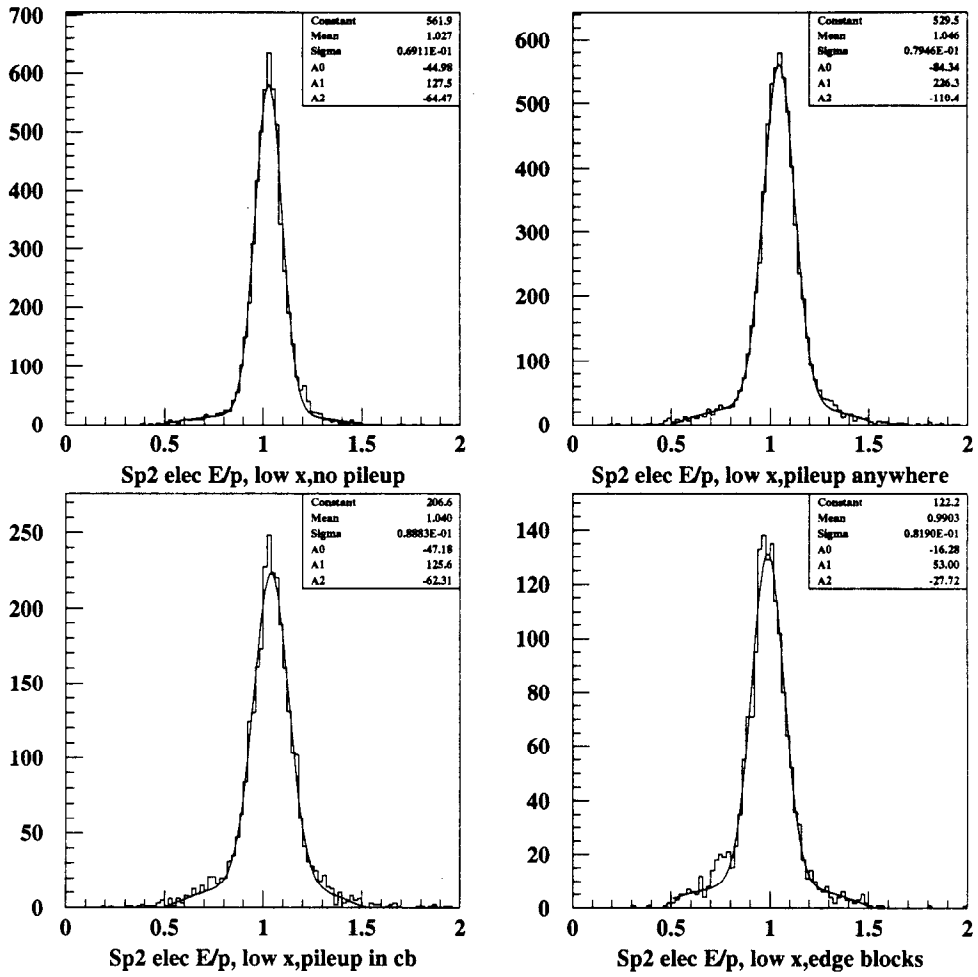

Fig. 3.16. Same as Fig. 3.15 for electrons with $9 < p < 12$ GeV.

block, cluster position, etc., combined in a non-linear fashion, identifies the event. Due to its non-linear nature, the properties of the network highly depend on the environment (rate, pion to electron ratio, etc.) and the event sample on which the network is "trained" (*i.e.* the way the relative weights of the input parameters are determined). Thus, the neural network efficiency is potentially rate dependent,[121,122] especially at low momentum where the rate of pion-electron overlaps is high. The overall efficiency is about 90% at low x,[121] and increases with momentum.

We discriminate between electron and pion showers by calculating the deviation from the electron shower shape χ

$$\chi = \frac{1}{E_4}\sqrt{\sum_i (E_i - E_4 \mathcal{S}(x_i - x_0, y_i - y_0) - E_{\text{back}})^2} \tag{3.16}$$

where the summation is over all cluster blocks, except for four most energetic ones used in the definition of E_4. The electrons are identified by the requirement $\chi \leq 0.045$. The distribution of the variable χ for electrons and pions is shown in Fig. 3.17. The efficiency was defined as a ratio of events that passed the cut to the total number of events. The electron and pion efficiencies are shown in Fig. 3.18. The electrons were selected by requiring a track with Cherenkov pulses in both tanks higher than 4.5 photoelectrons and a good match with the shower cluster. The pions were defined as class 2 (no Cherenkov signals and a good match with a shower cluster) tracks. Open circles in Fig. 3.18 show the efficiencies for the electron and pion samples that included the additional cut $E/p > 0.8$.

Several observations can be made. First, the pion rejection power of the χ cut is about 10:1. However, for the pions that have $E/p > 0.8$, it is at best 2:1, comparable to the SLAC neural network performance under the same conditions.[121] The reason is that pions usually deposit large amount of energy if they undergo a charge exchange $\pi^- p \rightarrow \pi^0 n$. The π^0 decays instantly into two photons and develops an electromagnetic shower; such a cluster is almost indistinguishable from an electron

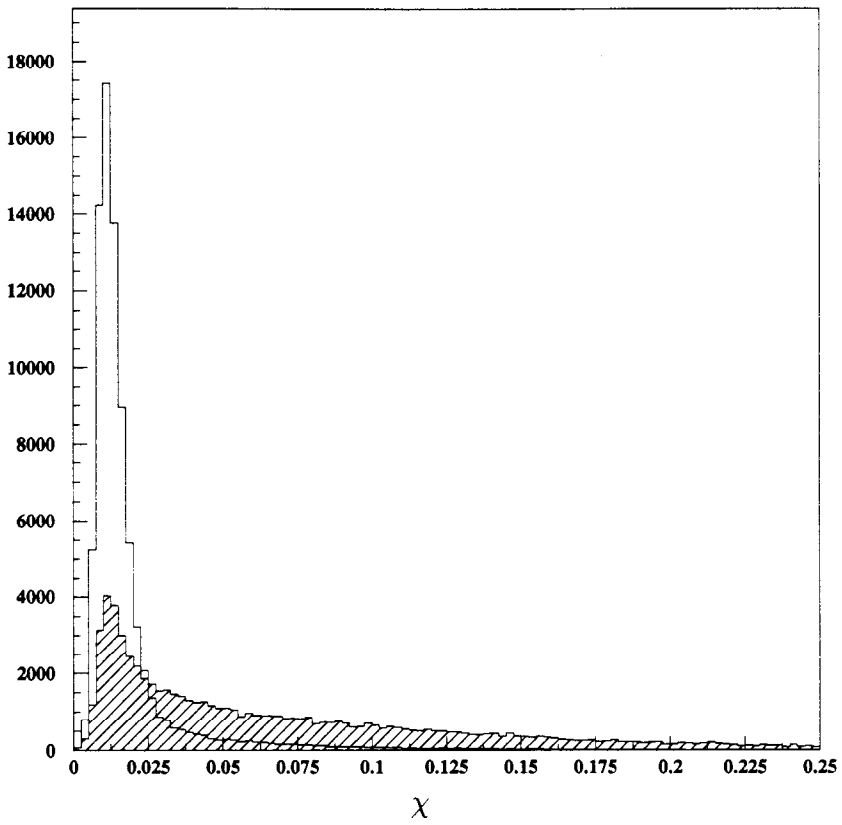

Fig. 3.17. Distribution of the shower shape variable χ for electrons (open) and pions (hatched).

cluster. Since the shape or neural net cut is optional and is usually applied *in addition* to the E/p cut, it is the latter rejection power that is relevant for the background analysis.

Electron efficiency ranges from 92% to 95% at low x (depending on the run), and slowly increases with momentum. It is comparable, if not slightly higher, than the neural network efficiency.[121] The variations with the run conditions are smaller than quoted for the SLAC code[121] that implies smaller rate dependence[7]. The reason for a sharp drop at about 30 GeV is use of the variable E_4 in Eq. (3.16). As was shown above (Fig. 3.13), it deviates significantly from the true cluster energy

[7]The rate dependence of the overall shower efficiency, including the shape cut, was studied by Piotr Zyla[123] and was found to be small (see Section 3.6).

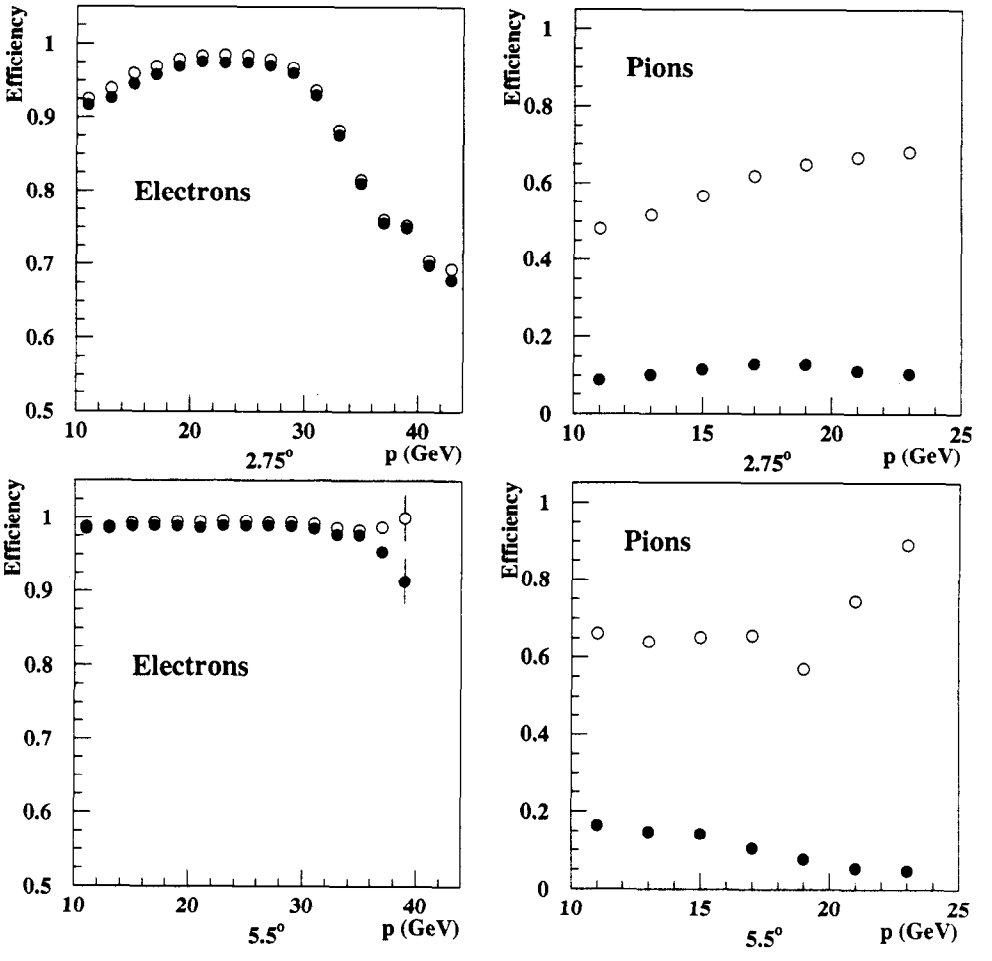

Fig. 3.18. Efficiencies of the shape cut for electrons (left) and pions (right) for 2.75° (top) and 5.5° (bottom) shower counters. A sample of electrons and pions is formed using the tracking and Cherenkov information as described in the text (closed circles). Open circles show efficiencies for the samples that included $E/p > 0.8$ cut.

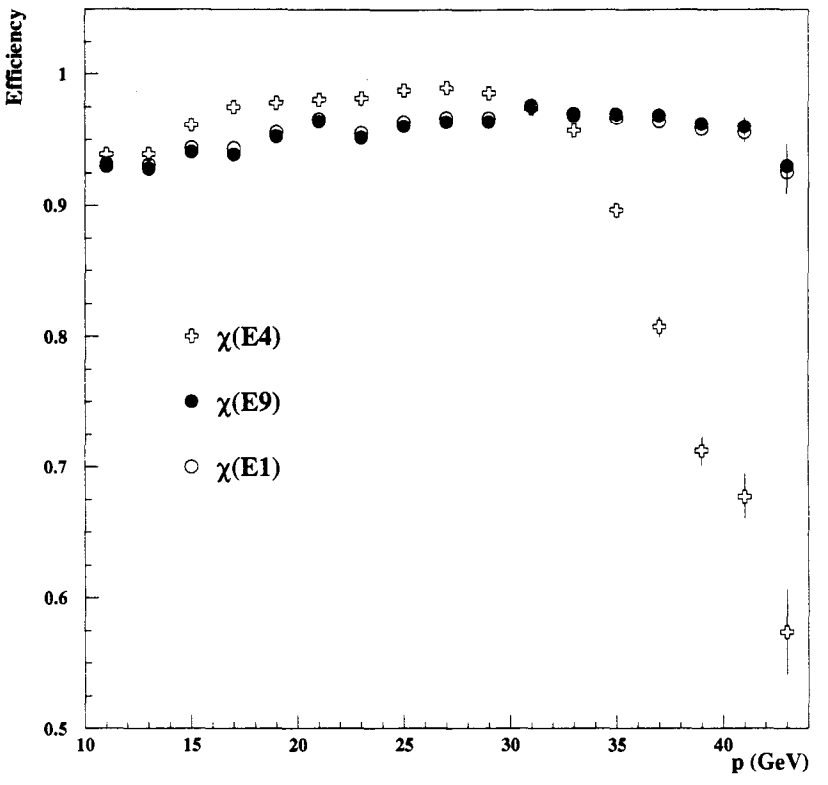

Fig. 3.19. Efficiency of the shape cut with different energy variables. Energy used in Eq. (3.16) is E_4 (crosses), E_1 (open circles), E_9 (closed circles). Note that the drop in efficiency disappears for E_1 and E_9.

starting at about 30 GeV, and the shape function $E_4\mathcal{S}(x_i-x_0, y_i-y_0)$ systematically underestimates true cell energy. The situation is improved, indeed, if other energy variables, E_1 or E_9 are used in Eq. (3.16) (Fig. 3.19). This effect was discovered too late to be applied to the DST production code. Instead, we turn off the shape cut for $p > 30$ GeV where pion contamination is negligible (see Section 3.7.3.2).

3.5 Tracking code

3.5.1 Introduction

The tracking code combines information from the hodoscopes, Cherenkov counters, and the shower counter to reconstruct charged particle tracks in the spectrometer. The standard electron definitions for the asymmetry analysis rely on the

tracking information. The momentum of an electron track is used to calculate the kinematics (x and Q^2) of the event. Thus, tracking is an important component of the physics analysis. In this note, we will describe the algorithm and its implementation, and discuss the efficiency and rate dependence.

3.5.2 Tracking algorithm

3.5.2.1 Track classes

In the following, we will often refer to the track *class* , *i.e.* a particular combination of detector systems used to fit a track. We recognize 4 track classes:

1. A shower cluster, at least one Cherenkov hit, and at least a minimum number (see below) of hodoscope hits.

2. A shower cluster and hodoscope hits; no Cherenkov hit is found within the time window.

3. At least one Cherenkov hit and hodoscope hits. No shower cluster is found within time and space limits.

4. Hodoscope hits only.

The track classes are exclusive, *i.e.* one track cannot be a member of two classes. Tracks of class 1 are electron candidates, and class 2 tracks are most probably pions. Tracks of class 3 are used primarily for the calibration of the shower counter (when cluster information is deliberately removed from tracking to eliminate biases), they are never used in the asymmetry analysis[8]. Class 4 tracks are used for diagnostic purposes.

[8]Class 3 tracks could be identified as real particles, for example, muons or pions with momentum above the Cherenkov threshold (12 GeV for muons and 19 GeV for pions in 2.75° spectrometer) that deposit a small amount of energy into the calorimeter and are therefore undetected. In the high rate environment of E154, however, most of such tracks are random coincidences.

3.5.2.2 Initialization

The tracking subroutines are called every spill for each spectrometer. As a first step, we copy information from the Cherenkov, hodoscope, and shower counter common blocks into the local data banks. For every detector hit, we calculate the target time

$$\tau_i = t_i - z_i/c \,, \tag{3.17}$$

where z_i is the z position of each detector and t_i is the actual time of the hit. By convention, the z position for the Cherenkov hits is taken in the center of the mirror, the z position of a hodoscope finger is in its geometrical center, and the z position of the shower cluster is associated with the center of gravity of the electron shower which is located approximately 5 radiation length deep.[124]

Each hit is characterized by its time τ, and the time resolution $\sigma(\tau)$. Hodoscope and shower hits also have the coordinate information. For the shower hit, we keep (x, y) positions of the cluster and the position uncertainties (σ_x, σ_y). For the hodoscope hits, we calculate the coordinate

$$u = x \cos\theta_u + y \sin\theta_u \,, \tag{3.18}$$

where $0 \leq \theta_u \leq \pi$ is the angle between the longest side of the finger and the $\hat{y}$ axis (counting counterclockwise)[9]. The direction $\hat{u}$ is perpendicular to the finger direction; thus, u is the coordinate *measured* by the finger. The finger resolution $\sigma(u) = w/\sqrt{12}$, where w is the finger width. The hodoscope planes are grouped in "packages" – the front hodoscope package (H1U, H2V, H3X, H4Y, H5Y, and H6X in the 2.75° spectrometer and H1U, H2X, H3Y, and H4V in the 5.5° spectrometer) and the back hodoscope package (H7X, H8Y, H9Y, and H10X in the 2.75° spectrometer and H5U, H6X, H7Y, H8V in the 5.5° spectrometer).

[9]The finger tilt in $(\hat{y}, \hat{z})$ plane is not important numerically and is ignored.

3.5.2.3 *Optics cuts*

One of the main strengths of the E154 tracking code is the use of optics cuts to reduce the combinatorial background in the hodoscopes, important in the high background rate environment. We employ the following strategy. The search for track candidates starts with the shower cluster. For charged particles originating from the target, the direction of the momentum is strongly correlated with the impact point at the shower counter. This can be clearly seen in Fig. 3.20. The correlation is strongest in $\hat{x}$ direction, where the effect of the magnetic field is small. In fact, the main reason for a non-zero width of the $\hat{x}$ distribution in the 5.5° spectrometer is the finite target length since there is almost no vertical component to the magnetic field. Even in the 2.75° spectrometer the correlation is strong. The correlation is not so strong in the $\hat{y}$ direction in both spectrometers; the peculiar shape of the $\hat{y}$ distributions is due to the reverse-bend optics of the spectrometers. Clearly, the optics cuts are strongest at the top of the spectrometer, *i.e.* at low momentum. The random background, that is thought to be caused by low-energy photons and neutrons, is roughly (within a factor of two) uniform across the face of the hodoscopes. Thus, the optics information enhances the signal/noise ratio in the search region of the hodoscopes.

The cut is implemented in the following way. The maps $\Theta_{\mathrm{min}}(x_{\mathrm{sh}})$, $\Theta_{\mathrm{max}}(x_{\mathrm{sh}})$, $\Phi_{\mathrm{min}}(y_{\mathrm{sh}})$, and $\Phi_{\mathrm{max}}(y_{\mathrm{sh}})$ are generated using a Monte Carlo program. Here $\left(\frac{dx}{dz}\right) \equiv \Theta$ and $\left(\frac{dy}{dz}\right) \equiv \Phi$ are track slopes, and min and max denote the minimum and maximum slopes for a particle scattered at the target and with a coordinate at the shower counter $(x_{\mathrm{sh}}, y_{\mathrm{sh}})$. We take into account the spatial resolution of the shower counter by increasing the slope range:

$$\begin{aligned} \Theta_{\mathrm{min}} &= \min\left(\Theta_{\mathrm{min}}(x_{\mathrm{sh}} \pm C_L\sigma(x_{\mathrm{sh}}))\right) \\ \Theta_{\mathrm{max}} &= \max\left(\Theta_{\mathrm{max}}(x_{\mathrm{sh}} \pm C_L\sigma(x_{\mathrm{sh}}))\right) \end{aligned} \tag{3.19}$$

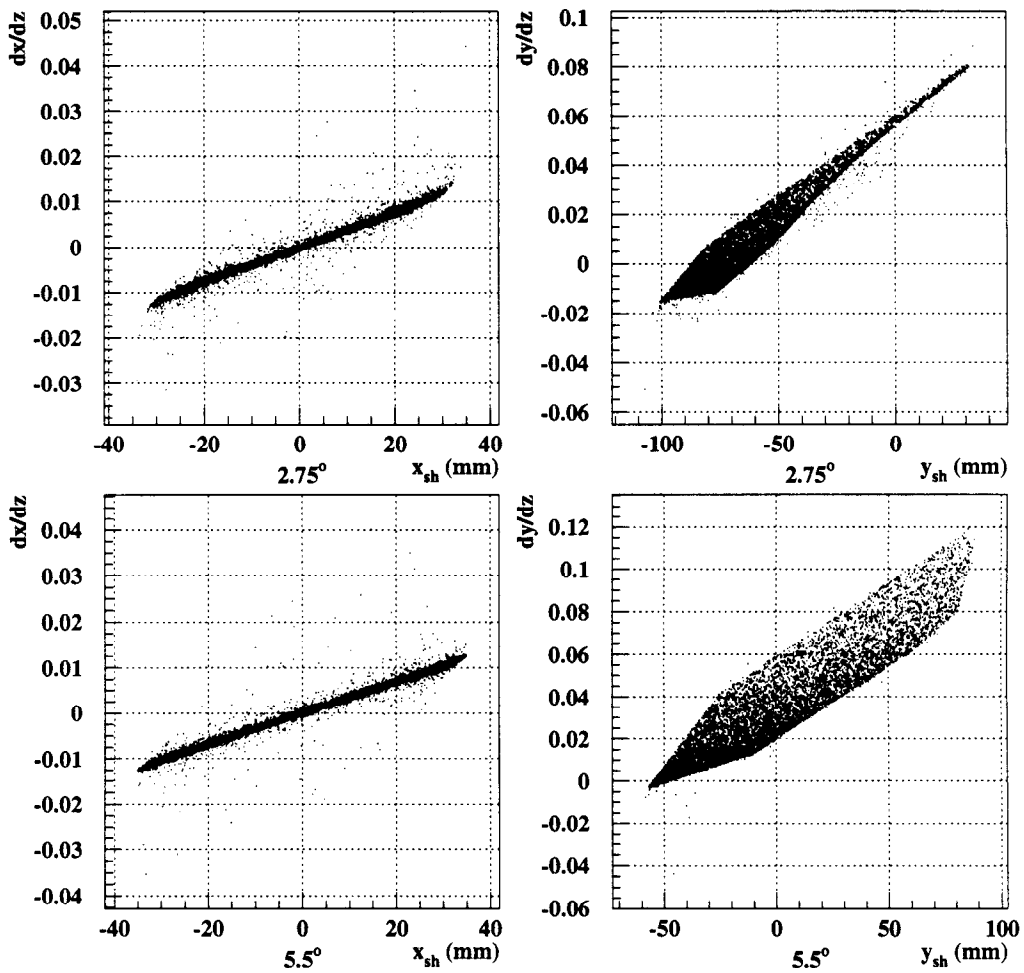

Fig. 3.20. Distribution of slopes of charged particle tracks (in $\hat{x}$, left, and $\hat{y}$, right) versus track position at the shower counter for 2.75° (top) and 5.5° (bottom) spectrometers.

and analogously in $\hat{y}$ direction. The "confidence level" factor C_L was chosen to be 5 to optimize efficiency[10]. Now for every hodoscope plane we determine the range of allowed coordinates:

$$\begin{aligned} u_{\min} &= \min(u_1, u_2, u_3, u_4) - C_X \cdot w \\ u_{\max} &= \max(u_1, u_2, u_3, u_4) + C_X \cdot w \ , \end{aligned} \tag{3.20}$$

where $C_X = 3$ is a factor that allows for the finite hodoscope resolution and w is the hodoscope width (the combination of these two factors makes the search area bigger by one finger in each direction). Finally, the combinations u_1, u_2, u_3, and u_4 are

$$\begin{aligned} u_1 &= x_{\min}\cos\theta_u + y_{\min}\sin\theta_u \\ u_2 &= x_{\min}\cos\theta_u + y_{\max}\sin\theta_u \\ u_3 &= x_{\max}\cos\theta_u + y_{\min}\sin\theta_u \\ u_4 &= x_{\max}\cos\theta_u + y_{\max}\sin\theta_u \ , \end{aligned} \tag{3.21}$$

where θ_u is defined in Eq. (3.18). Corners of the region allowed by optics are

$$\begin{aligned} x_{\min} &= [x_{\rm sh} - C_L\sigma(x_{\rm sh})] + \Delta z\Theta_{\min} \\ x_{\max} &= [x_{\rm sh} + C_L\sigma(x_{\rm sh})] + \Delta z\Theta_{\max} \\ y_{\min} &= [y_{\rm sh} - C_L\sigma(y_{\rm sh})] + \Delta z\Phi_{\min} \\ y_{\max} &= [y_{\rm sh} + C_L\sigma(y_{\rm sh})] + \Delta z\Phi_{\max} \ , \end{aligned} \tag{3.22}$$

where $\Delta z = (z_{\rm hod} - z_{\rm sh})$.

[10]This factor also reflects a non-gaussian shape of the calorimeter resolution due to multiple scattering and bremsstrahlung in the spectrometer.

3.5.2.4 Track candidates

We will discuss the algorithm for the first two track classes. Algorithm for classes 3 and 4, that do not include clusters, is a simple extension of the main algorithm and will be discussed later.

We loop first over the shower clusters that are identified as electrons by the shower particle ID algorithm (neural net for SLAC analysis and shape cut for Caltech), and then over all remaining clusters. For every cluster, we look for time coincidence with a Cherenkov signals. We first select Cherenkov hits that are within a time window

$$\Delta\tau = \tau_{\rm sh} - \tau_{\rm ch} = C_T \cdot \sqrt{\sigma^2(\tau_{\rm sh}) + \sigma^2(\tau_{\rm ch})} \tag{3.23}$$

from the shower cluster. Here τ is the "target" time (see Eq. (3.17)), and $\sigma(\tau_{\rm sh})$ and $\sigma(\tau_{\rm ch})$ are shower time and Cherenkov resolutions. Factor C_T is typically set to 3. Among all selected hits, we pick two (or one, if hits from only one tank are found) that minimize χ^2

$$\chi^2 = \sum_i \frac{(\tau_i - \langle\tau\rangle)^2}{\sigma^2(\tau_i)}\,, \tag{3.24}$$

where the summation includes the shower cluster and Cherenkov hits from each tank. The average time $\langle\tau\rangle$ is given as usual by

$$\langle\tau\rangle = \frac{\sum_i \tau_i/\sigma^2(\tau_i)}{\sum_i 1/\sigma^2(\tau_i)}\,. \tag{3.25}$$

This average time and its uncertainty

$$\sigma^2(\langle\tau\rangle) = \frac{1}{\sum_i 1/\sigma^2(\tau_i)} \tag{3.26}$$

are used to define the time window for the hodoscope hits. If no Cherenkov hits are found to match the cluster, the track is a class 2 candidate; time $\langle\tau\rangle$ and its uncertainty are then taken from the shower cluster.

3.5.2.5 Hodoscope mini-clusters

After the Cherenkov and shower cluster match is found, we select the hodoscope hits that pass the optics cuts and are sufficiently close in time to the average time $\langle\tau\rangle$ to be with the window $\langle\tau\rangle \pm \Delta\tau$, where

$$\Delta\tau = C_T \cdot \sqrt{\sigma^2(\langle\tau\rangle) + \sigma^2(\tau_{\rm hod})} \; . \tag{3.27}$$

The next step is to arrange the hits within a hodoscope package (front and rear) into local clusters. The idea is to eliminate combinations of fingers that cannot geometrically belong to one track. To reduce the pattern recognition problem to two dimensions, we first project all fingers onto a common plane (taken at the z position of the last plane of the package). We use a stereographic projection along the line connecting the center of a given finger and the shower cluster:

$$\begin{aligned} x_c &\rightarrow x_c^{'} = x_c + (x_{\rm sh} - x_c)\frac{z^{'} - z}{z_{\rm sh} - z} \\ y_c &\rightarrow y_c^{'} = y_c + (y_{\rm sh} - y_c)\frac{z^{'} - z}{z_{\rm sh} - z} \\ w &\rightarrow w^{'} = w + (w_{\rm sh} - w)\frac{z^{'} - z}{z_{\rm sh} - z} \; . \end{aligned} \tag{3.28}$$

Here (x_c, y_c) is the position of the finger center, z is the finger z position, and $z^{'}$ is the position of the plane of projection. Note that the finger width w is also modified; the shower width $w_{\rm sh}$ is given by

$$w_{\rm sh} = 3\left(\sigma(x_{\rm sh})|\cos\theta_u| + \sigma(y_{\rm sh})|\sin\theta_u|\right) \; . \tag{3.29}$$

Now the problem is reduced to selecting sets of overlapping rectangles (fingers). This is done iteratively. We first find all crossings among all hit fingers in the first two planes of the package. Crossed fingers are replaced by a rectangle that represents the area common to both fingers. This is shown in Fig. 3.21. For simplicity, we make the resulting box parallel to the $\hat{x} - \hat{y}$ axes. Every such finger overlap makes a new

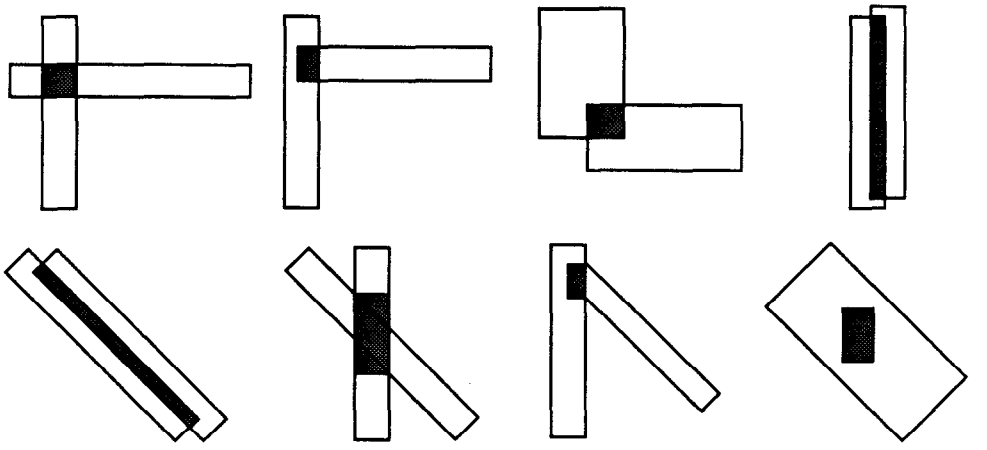

Fig. 3.21. Possible two-finger mini-clusters.

hodoscope mini-cluster. We then loop over fingers in the next plane of the package and look for fingers that cross either an existing cluster, or a finger in the first two planes. In the former case, the finger is added to the existing mini-cluster, in the latter, a new mini-cluster is created. The procedure is repeated until all possible mini-clusters are found. Examples of hodoscope mini-clusters are shown in Fig. 3.22.

3.5.2.6 Fitting

The track candidates are formed from the shower clusters, Cherenkov hits, and all combinations of hodoscope mini-clusters. All tracks are straight in the detector hut, so for every track we calculate 5 parameters: line intercepts and slopes (x_0, Θ, y_0, Φ), and track time at the target τ_0. This is done by minimizing

$$\chi^2 = \sum_i \left(\frac{(x_0 + z_i\Theta)\cos\theta_u + (y_0 + z_i\Phi)\sin\theta_u - u_i}{\sigma(u_i)} \right)^2 + \sum_j \left(\frac{\tau_0 - \tau_i}{\sigma(\tau_i)} \right)^2 . \quad (3.30)$$

The first sum in Eq. (3.30) includes the hodoscope hits and the shower cluster (for the latter we have two entries: $u \equiv x$ and $u \equiv y$). The second sum also includes Cherenkov hits. The resulting system of linear equations can be factorized into the

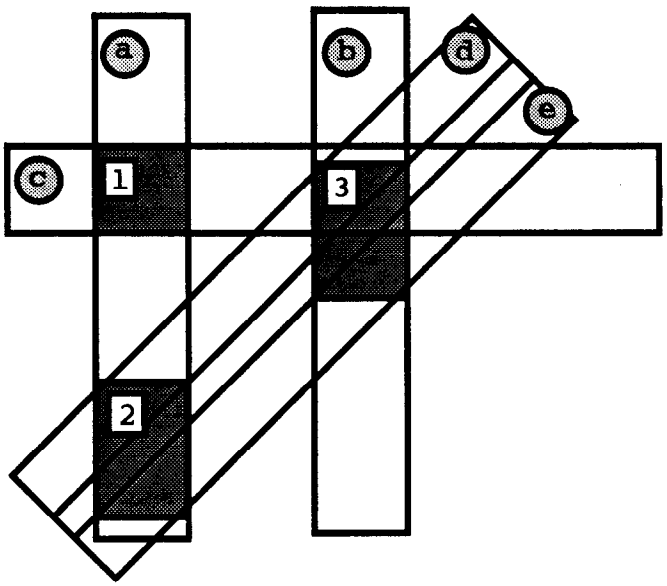

Fig. 3.22. Three mini-clusters are formed from five hit fingers. Cluster (1) consists of fingers (a) and (c), (2) of (a), (d), and (e), and (3) of (b), (c), (d), and (e).

space and time parts. The time of the track τ_0 is then readily found as an average of all hits, weighted by the uncertainty $\sigma(\tau_i)$. In order to increase performance, we in fact first do the fitting in the time domain only, remove all hits with times τ_i outside the $\chi^2_{\max}$ cut (see next section), and then repeat the fit in both space and time.

The detector time τ_i needs to be corrected for the time of the light propagation from the point where the track crosses the detector (hodoscope finger or Cherenkov mirror) to the phototube. For the hodoscopes, it is the time of light propagation inside the finger. By convention, the time offsets for the hodoscope fingers are calculated for a track that passes through the geometrical center of the finger, so such tracks need no propagation time correction. Therefore, the correction is proportional to the distance from the finger center to the track:

$$\Delta\tau_{\text{hod}} = \frac{1}{v}\left[-(x_0 + z_c\Theta - x_c)\sin\theta_u + (y_0 + z_c\Phi - y_c)\cos\theta_u\right] , \qquad (3.31)$$

where (x_c, y_c, x_c) is the geometrical center of the finger. The correction is positive (the track passed later than τ_i) if the track position is closer to the phototube than

the finger center. The constant v is the effective light propagation speed along the finger. It is a phenomenological constant that reflects the geometry of the fingers and peculiarities of the light collection, and is unique to every plane. It ranges from 135 mm/ns to 213 mm/ns[11].

For the Cherenkov detectors, we correct for the light propagation from the mirror to the phototube. The time offsets for the Cherenkov counters correspond to the geometrical center of the mirror. Thus, the correction is related to the *difference* between the distance from the track position at the mirror to the phototube and the distance from the mirror center to the phototube:

$$\Delta\tau_{\text{hod}} = \frac{1}{c}\left[\sqrt{(x_0+z_m\Theta-x_p)^2+(y_0+z_m\Phi-y_p)^2+(z_m-z_p)^2}- \sqrt{(x_m-x_p)^2+(y_m-y_p)^2+(z_m-z_p)^2}\right], \tag{3.32}$$

where (x_m, y_m, z_m) is the center of the mirror, (x_p, y_p, z_p) are the phototube positions, and c is the speed of light. We neglect mirror curvature and yaw.

3.5.2.7 *Selecting the best track candidate*

After the track parameters are found, we calculate the time and spatial residuals for every hodoscope and Cherenkov hit, and find the hit with the worst

$$\chi_i^2 = \left(\frac{(x_0+z_i\Theta)\cos\theta_u+(y_0+z_i\Phi)\sin\theta_u-u_i}{\sigma(u_i)}\right)^2+\left(\frac{\tau_0-\tau_i}{\sigma(\tau_i)}\right)^2. \tag{3.33}$$

For the Cherenkovs, there is indeed no spatial residual. We set the limit $\chi^2_{\text{max}} = 8$ for the fit in the time domain and $\chi^2_{\text{max}} = 16$ for the combined space-time fit. If $\chi^2_{\text{worst}} > \chi^2_{\text{max}}$, the worst hit is removed from the track candidate unless

- The number of hits in the hodoscope package drops below the threshold. The minimum number of hits was set to 4 for the front hodoscope package in 2.75°

[11] Note that the physical light propagation speed for Bicron BC404 is 190 mm/ns that corresponds to the refractive index of 1.58.

spectrometer and to 3 for the back package in 2.75° and for both packages in 5.5° spectrometer. This number is half the expected average number of hits per package if the hodoscopes are 100% efficient (except the back hodoscope package of 2.75° spectrometer where the expected average number of hits is 5).

- One of the sums

$$\sum_{\text{planes}} |\cos\theta_u| \,, \quad \sum_{\text{planes}} |\sin\theta_u|$$

drops below the threshold of 0.5 for one of the hodoscope packages. This requirement assures that both $\hat{x}$ and $\hat{y}$ projections are determined.

If one of the conditions above is met, the entire track candidate is dropped. Otherwise, the worst hit is removed and the fit is repeated. The fitting converges if either all hits are within χ^2_{max} limit, or the candidate is dropped. Out of all successful track candidates (combinations of hodoscope mini-clusters), we pick one with the best total χ^2 per degree of freedom.

If the track is fitted successfully, the hits are marked to prevent them from being used on another track[12].

3.5.2.8 Class 3 and 4 tracks

The algorithm for class 3 and 4 tracks (that do not include a shower cluster) is an extension of the general algorithm discussed above. First, the spill is divided into 6 nsec time intervals. Let τ_0 denote the center of an interval. We find the time slice with the most Cherenkov and hodoscope hits within ± 9 nsec around τ_0 (preference is always given to the intervals with most Cherenkov hits). Then, a "fake" shower cluster is created with time τ_0, time uncertainty $9/C_T$ nsec (C_T is the time "confidence level factor" of Eq. (3.27)), and infinite position resolution. From

[12]For Caltech DST production, we disabled marking of Cherenkov hits and reduced rate dependence by about 0.5%.

this point, the algorithm proceeds exactly as described above for classes 1 and 2 with the following trivial modifications:

- The minimum and maximum track slopes are used to define the stereographic projection in Eq. (3.29).
- The "fake" shower cluster is not used in fitting.

The search for class 3 and 4 tracks stops when track candidates in all time slices are exhausted.

3.5.3 Performance

Typically, an electron track in the 2.75° spectrometer is constructed of 16-17 hits (including all detectors, Fig. 3.23). The average number of hits per hodoscope package is found to be close to the expectation (8 for the front package and 5 for the rear package) that implies that the hodoscope inefficiency is not big. We estimate the tracking efficiency by comparing the number of shower clusters with the number of associated tracks. The inefficiency, defined as the ratio $(N_{\text{clusters}} - N_{\text{tracks}})/N_{\text{clusters}}$, is shown in Fig. 3.24 for all clusters (top left), and for electron clusters. The low energy clusters are mostly pions, and the tracking efficiency for them is low. This is mostly due to the fact that the resolution (both spatial and time) of the shower counter is worse for pions than it is for electrons, and hence the initial cuts (optics and time) are not as efficient as for electrons. The electron efficiency is better than 90%, even after the E/p cuts. To identify the electron clusters in Fig. 3.24, we require a time coincidence among the cluster and two Cherenkov hits with the peak voltage greater than 50. This sample is still somewhat contaminated by random coincidences of pion clusters with Cherenkov hits, so the values of inefficiencies in Fig. 3.24 are upper limits of true electron inefficiencies.

An independent determination of the tracking efficiencies was based on a Monte Carlo technique. Electron tracks, generated using the optics model of the spectrom-

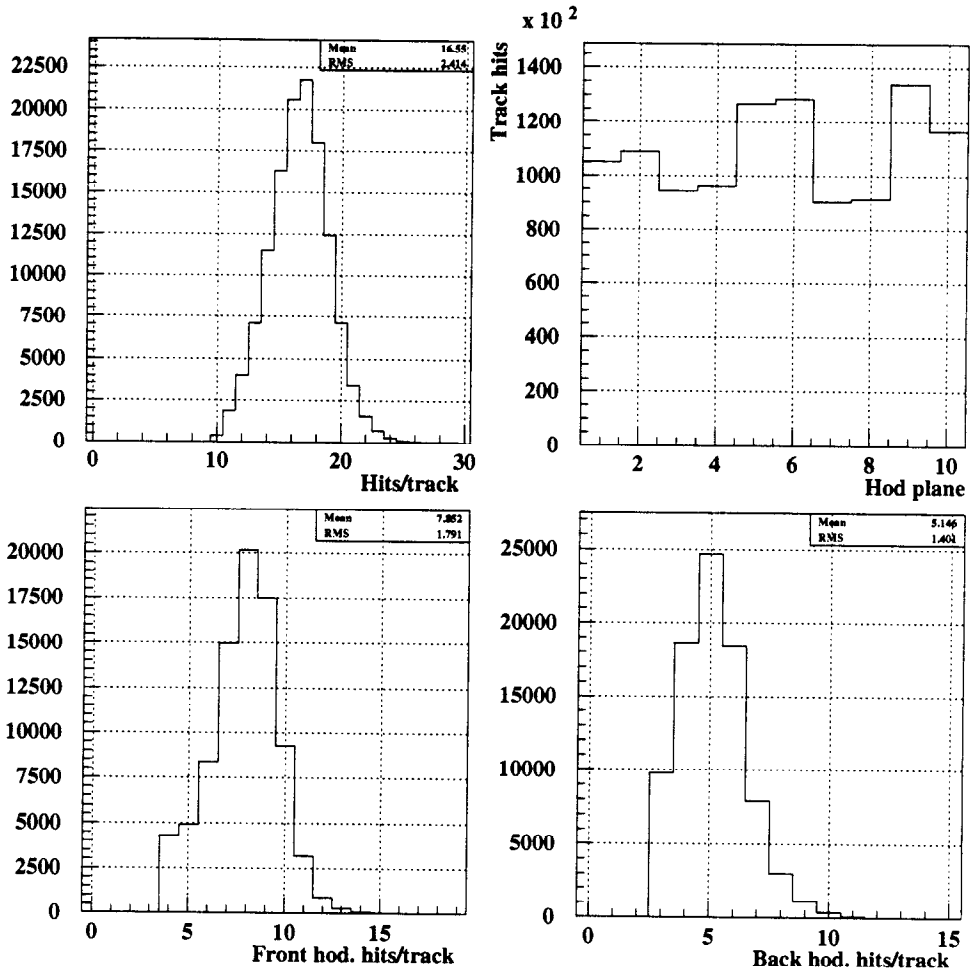

Fig. 3.23. Distribution of hits per track (top left), hits per hodoscope plane (top right), and distributions of track hits in the front (bottom left) and back (bottom right) hodoscope packages. All plots are for electrons in the 2.75° spectrometer.

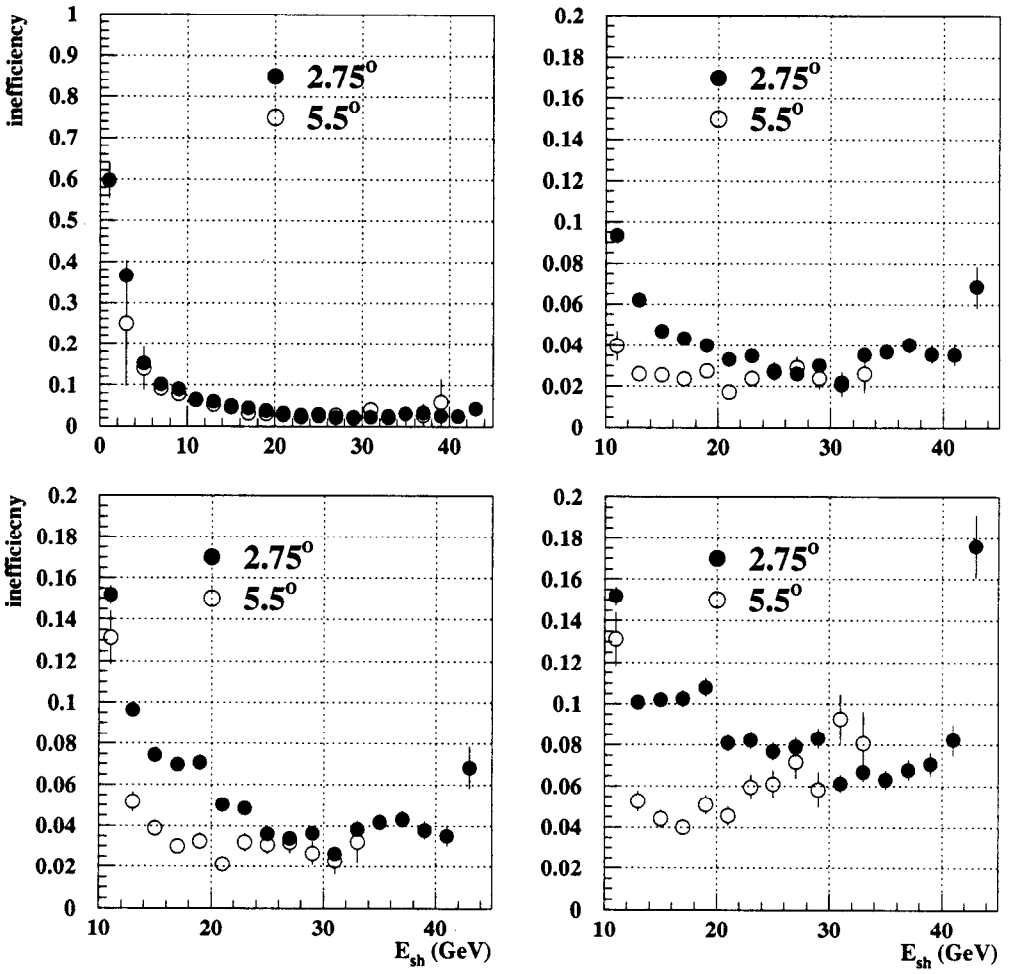

Fig. 3.24. Tracking inefficiency determined by the data (see text) for all clusters (top left) and for electron clusters (top right). Additional cuts are applied to electron tracks: $0.8 < E/p$ (bottom left) and $0.8 < E/p < 1.25$ (bottom right). Data are for ruin 3366 (beam current of $5 \cdot 10^{10}$ electrons/spill).

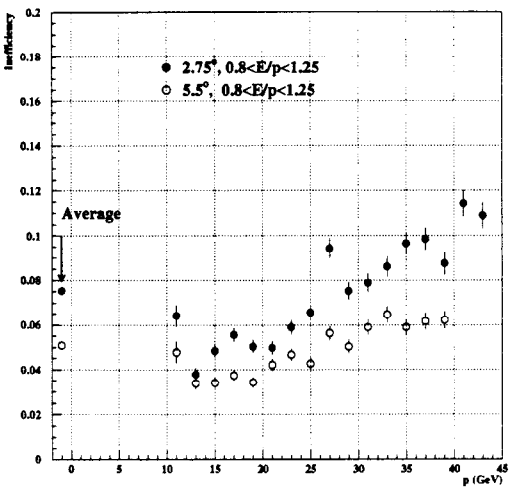

Fig. 3.25. Tracking inefficiencies for two spectrometers determined by the Monte Carlo method.

eter, were "seeded" among the real data and then reconstructed by the standard analysis code. The resolution and dead-time effects were taken into account. The efficiency was determined as the ratio of the number of reconstructed tracks with $0.8 \leq E/p \leq 1.25$ to the number of seeded tracks (see Fig. 3.25). It is consistent with the efficiencies determined by the data. The effect of the optics cuts described in Section 3.5.2.3 is demonstrated in Fig. 3.26. The tracking efficiency significantly decreases (by up to 5% in 2.75° spectrometer) when the optics cuts are turned off. Roughly the same decrease in efficiency was found when the local hodoscope clustering was turned off. Both effects is due to random coincidences in hodoscopes and are strongly rate dependent.

The largest contributions to inefficiency for 2.75° spectrometer are (on average):

- Momentum and energy resolution (in E/p cut): $\approx 2.5\%$;
- Hodoscope dead time: $\approx 2\%$
- Algorithm (cuts): $\approx 2\%$
- Hodoscope random coincidences: $\approx 1\%$

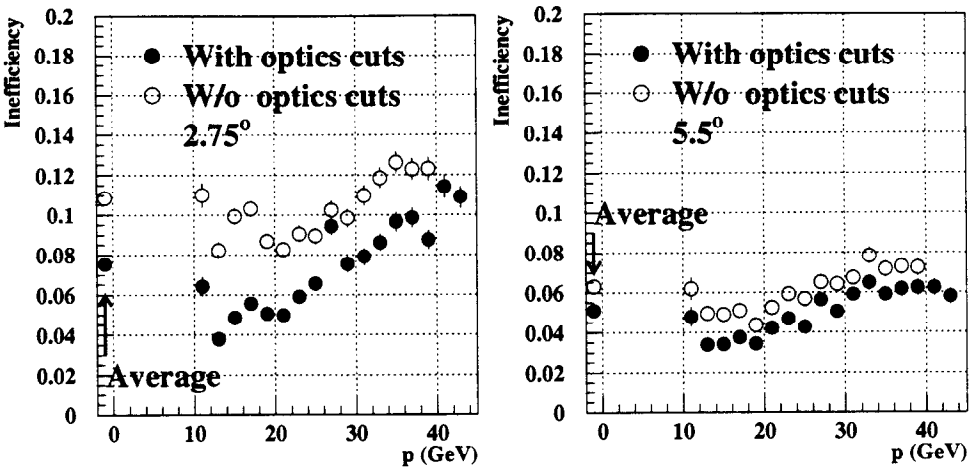

Fig. 3.26. Monte Carlo tracking inefficiencies for codes with and without optics cuts.

Contributions from the rate dependent sources (hodoscope dead time and random coincidences) are not large. The largest momentum dependence of inefficiency is due to E/p cuts; inefficiency increases with momentum as the resolution is degraded.

The rate dependence of tracking was studied by Piotr Zyla.[123] The contributions to the rate-dependent inefficiency from the hodoscope noise was found to be within 2% for every target (consistent with the estimates above). It was also found that the momentum determination is robust against the rate changes, much more than the energy determined by the shower counter (see Fig. 3.27).

3.5.4 Resolution

The tracking resolutions were determined by Monte Carlo (see above). Tracking timing resolution is $\approx 0.25 - 0.3$ nsec in both spectrometers (Fig. 3.28). Fig. 3.29 shows the spatial resolution in both spectrometers at the z position of the shower counter for electrons[13]. The spatial resolution for class 3 tracks (that do not use shower clusters) is shown in Fig. 3.30. It is significantly worse than that of class 1 and 2 tracks, and is in fact comparable to the position resolution of the shower counter

[13]All plots in this section are for Caltech analysis.

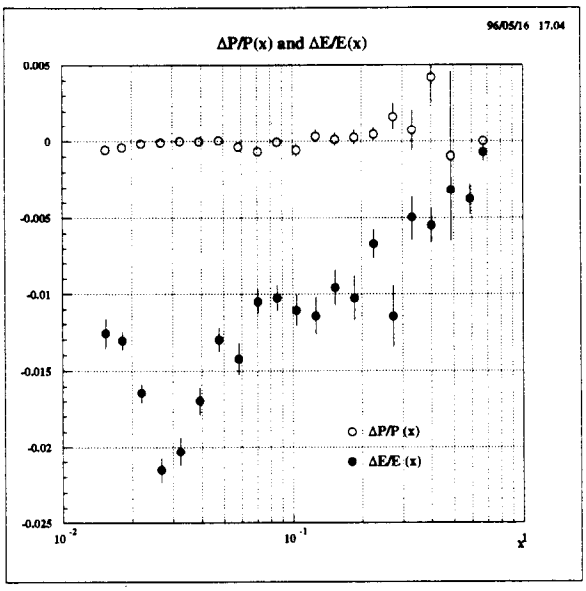

Fig. 3.27. Rate dependence of momentum and energy reconstruction. Plotted are the relative changes in momentum (open circles) and energy (closed circles) versus Bjorken x in 2.75° spectrometer when the detector rate is doubled. Courtesy of Piotr Zyla.[123]

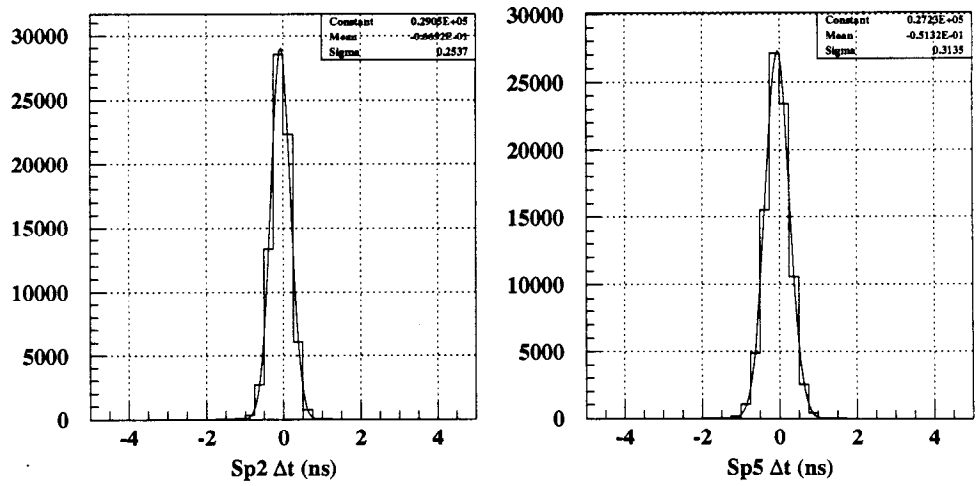

Fig. 3.28. Tracking time resolution in 2.75° (left) and 5.5° (right) spectrometers.

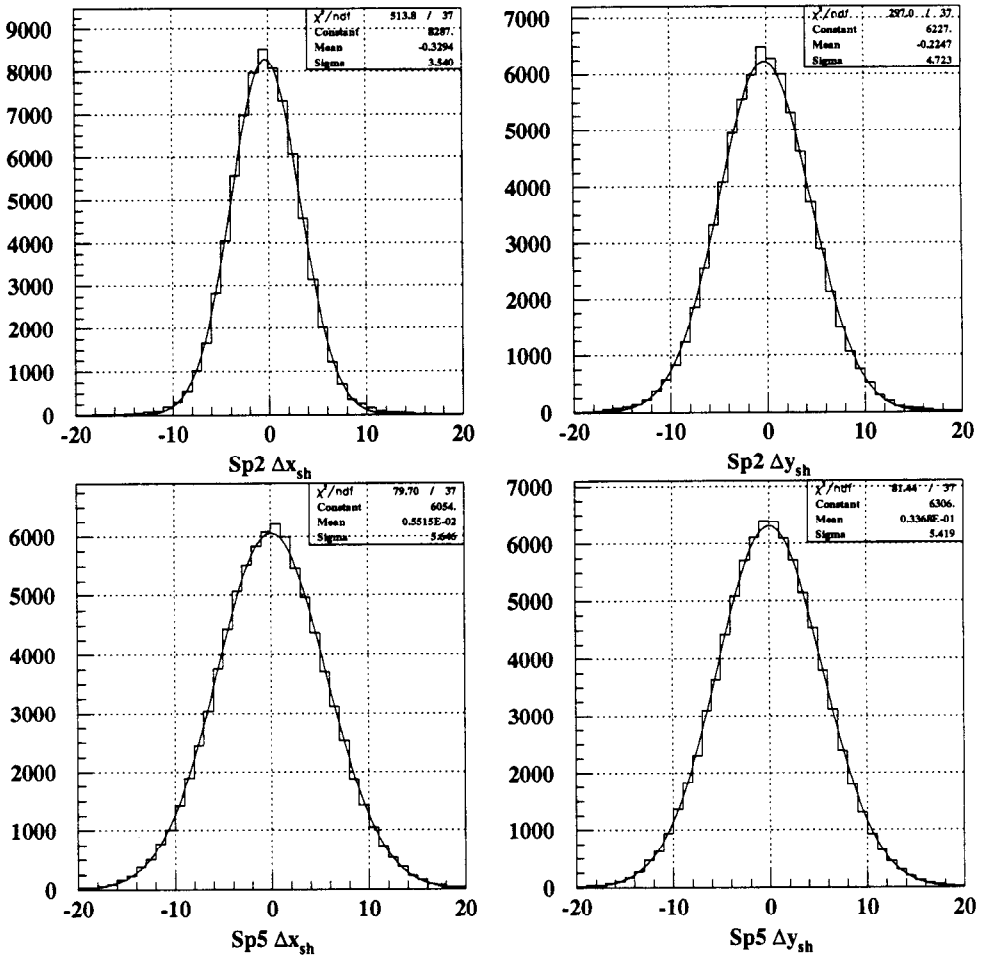

Fig. 3.29. Tracking resolution in x (left) and y at the z position of the shower counter for class 1 electrons. 2.75° (top) and 5.5° (bottom) spectrometers. All numbers are in mm.

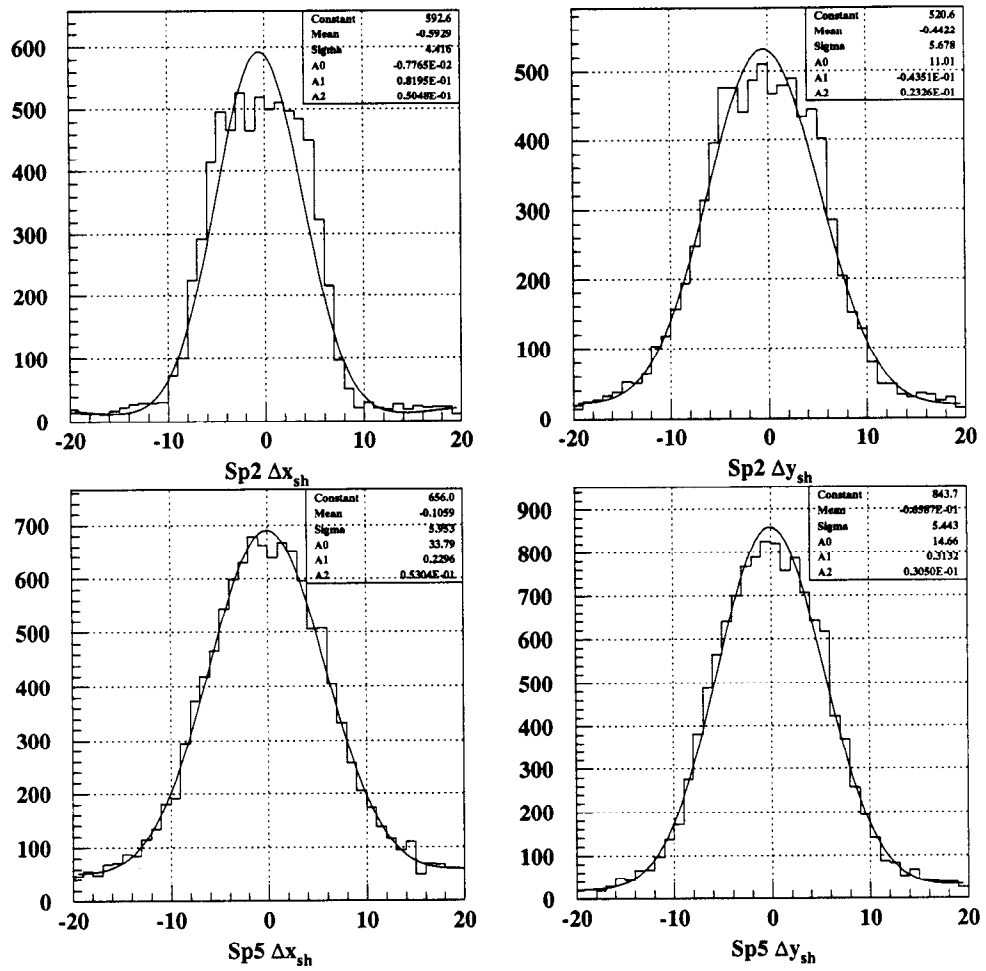

Fig. 3.30. Tracking resolution in x (left) and y (right) at the z position of the shower counter for class 3 tracks. 2.75° (top) and 5.5° (bottom) spectrometers. Overlaid is a Gaussian fit with quadratic background. All numbers are in mm.

alone (see Section 3.4). The shape of the distribution is clearly not Gaussian. Its core reflects the finite size of the hodoscope fingers, and the tails are due to random background in the hodoscopes.

The resolutions of the reconstructed momenta and scattering angles are shown in Fig. 3.31 (for original, *i.e.* before cell the Picard setting of Q1). The average momentum resolution is 2.4% in the 2.75° spectrometer and 2.7% in the 5.5° spectrometer (weighted by acceptance). The average angular resolution is $\approx$ 0.4 mrad in both spectrometers. The momentum dependence of the momentum resolution is shown in Fig. 3.32. For the original quadrupole setting (pre-Picard runs), the resolution degrades rapidly at low momentum in the 2.75° spectrometer. This is due to strong quadrupole focusing that results in almost ambiguous optics in the upper part of the spectrometer. The angular resolution in the bend plane ($\sigma(\phi)$) also shows very strong momentum dependence. On the contrary, the angular resolution in the non-bend plane ($\sigma(\theta)$) is almost constant with momentum.

The parameterizations for the momentum and angular resolution are given by

$$\begin{aligned}
\frac{\sigma(p)}{p} &= \sqrt{\frac{0.013}{(\tilde{p}-7.58)^2} + (0.93\cdot 10^{-3}\tilde{p})^2}\,, \quad \text{Caltech, 2.75°, pre-Picard} \\
\frac{\sigma(p)}{p} &= \sqrt{0.011^2 + (0.81\cdot 10^{-3}\tilde{p})^2}\,, \quad \text{Caltech, 2.75°, Picard} \qquad (3.34) \\
\frac{\sigma(p)}{p} &= \sqrt{0.015^2 + (1.01\cdot 10^{-3}\tilde{p})^2}\,, \quad \text{Caltech, 5.5°}
\end{aligned}$$

$$\begin{aligned}
\frac{\sigma(p)}{p} &= \sqrt{\frac{0.013}{(\tilde{p}-7.54)^2} + (0.98\cdot 10^{-3}\tilde{p})^2}\,, \quad \text{SLAC, 2.75°, pre-Picard} \\
\frac{\sigma(p)}{p} &= \sqrt{0.011^2 + (0.89\cdot 10^{-3}\tilde{p})^2}\,, \quad \text{SLAC, 2.75°, Picard} \qquad (3.35) \\
\frac{\sigma(p)}{p} &= \sqrt{0.015^2 + (1.14\cdot 10^{-3}\tilde{p})^2}\,, \quad \text{SLAC, 5.5°}
\end{aligned}$$

where $\tilde{p} = \frac{20}{p_c}p$, and p_c is the central momentum of the spectrometer (all momenta are in GeV).

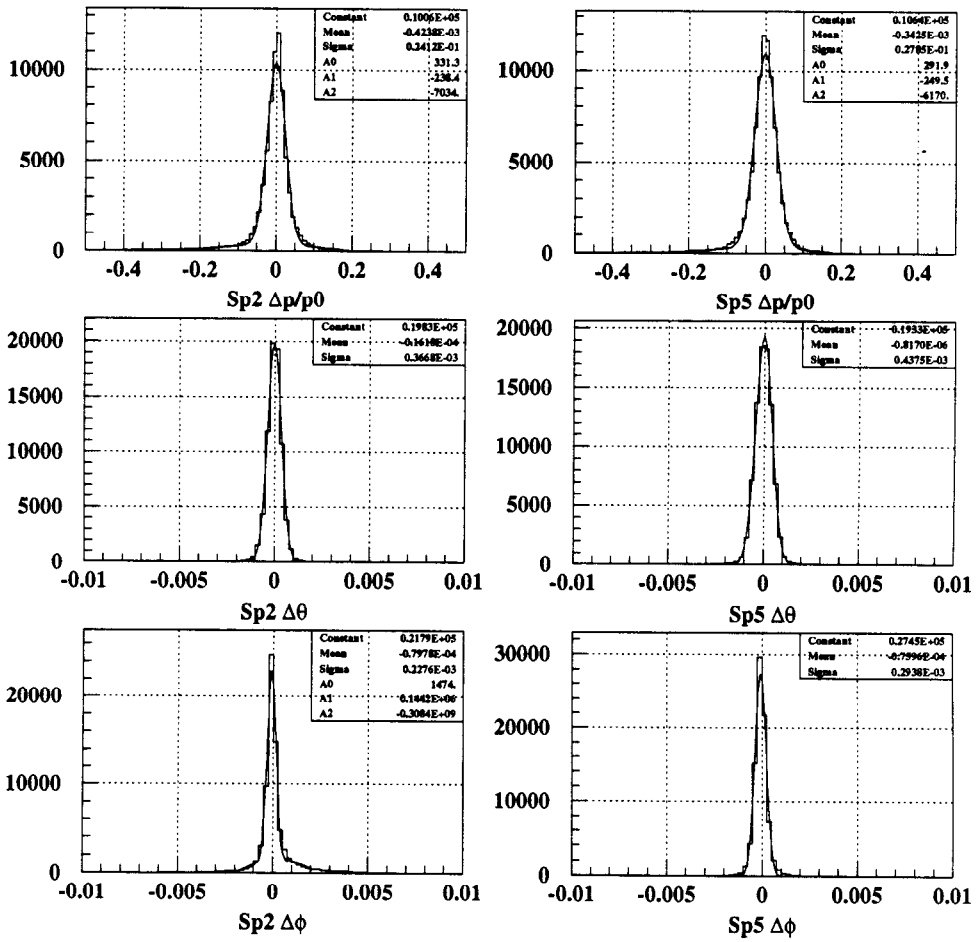

Fig. 3.31. Average momentum (top) and angular resolution in the bend (middle) and non-bend (bottom) planes. 2.75° (left) and 5.5° spectrometers (right)

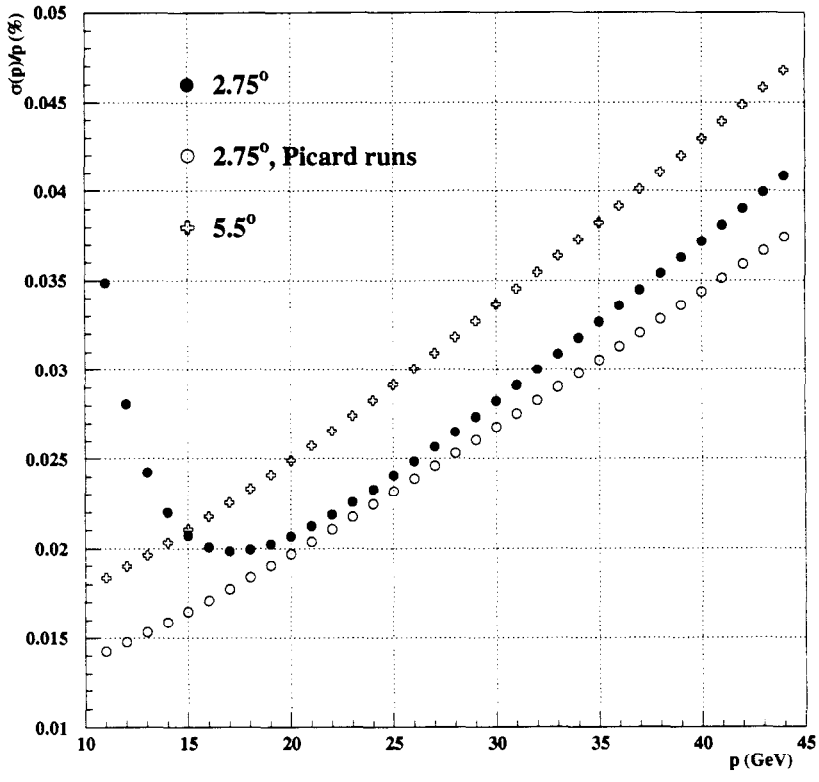

Fig. 3.32. Momentum dependence of the tracking momentum resolution. Standard optics configuration of 2.75° spectrometer is shown by solid circles, Picard optics is by open circles, and 5.5° spectrometer is shown by crosses.

The angular resolution in the bend plane is given by

$$\begin{aligned} \sigma(\phi) &= \frac{0.037}{(\tilde{p}-7.58)^2} + 0.194 \cdot 10^{-3}\,, \quad 2.75°, \text{ pre-Picard} \\ \sigma(\phi) &= \frac{0.002}{(\tilde{p}-7.58)^{0.71}}\,, \quad 2.75°, \text{ Picard}\,. \end{aligned} \tag{3.36}$$

The angular resolution in 5.5° spectrometer is independent of momentum. The difference between SLAC and Caltech values is negligible.

3.6 Efficiency and rate dependence

In E154, we measure asymmetry between cross sections in two different helicity states (see Section 1.2.1). The polarization direction of the target was reversed six times during the experiment. On another hand, the beam helicity was flipped every

pulse according to a pseudo-random pattern. Due to such rapid helicity changes, spectrometer acceptance and slow changes in efficiency average out between two polarization states and can be ignored. The average efficiency factorizes in Equations (1.10) and (1.11), and is cancelled. Thus, unlike experiments which measure absolute cross sections, the overall efficiency is not particularly important for E154 as long as it does not significantly impact statistics of the experiment.

The efficiency of each detector system, relative to other detectors in the spectrometer, was estimated by using the tracking code. For instance, when the efficiency of the Cherenkovs for electrons was studied, class 2 tracks with shower energy $E > 9$ GeV and $E/p > 0.8$ were selected. Efficiency was defined as the ratio of number of time coincidences between such tracks and Cherenkov signals to the total number of selected tracks. For a typical Cherenkov cut used in the analysis that required hits in both tanks in coincidence with one of them higher than 2.5 photoelectrons (see Section 3.7.3.2), the efficiency was about 90%. The intrinsic efficiency of the total absorption shower counter should in principle be very close to 100% (excluding dead blocks and similar hardware problems) at small rates (see below for the discussion of the rate dependence). The efficiency of the shower electron ID cut, such as χ cut (see Section 3.4) or neural network cut used in SLAC analysis[121] is typically $\approx 90 - 95\%$. Tracking efficiency, determined as described in Section 3.5, was also on the order $90 - 95\%$. Overall, the electron reconstruction efficiency is estimated to be $70 - 80\%$. Unfortunately, there is insufficient redundancy in the detector system to determine this number more precisely.

The rate dependence of the efficiency is potentially a much more important effect. Suppose, the reconstruction efficiency depends (linearly) on the electron rate:

$$\epsilon = \epsilon_0 (1 - \beta N) \ , \tag{3.37}$$

where ϵ is electron efficiency, β is a small linearity coefficient, and N is rate (in arbitrary units). The measured rate for each helicity is then

$$N^{L(R)} = N_0^{L(R)} \epsilon_0 \left(1 - \beta N_0^{L(R)}\right) , \tag{3.38}$$

where indices $L(R)$ denote the helicity state. It is easy to show that in this case the measured asymmetry will be biased:

$$A^{\text{meas}} \equiv \frac{N^L - N^R}{N^L + N^R} \approx A_0 - \beta \langle N \rangle A_0 . \tag{3.39}$$

Here $A_0 = \frac{N_0^L - N_0^R}{N_0^L + N_0^R}$ is the true asymmetry, the average electron rate is $\langle N \rangle = 1/2(N_0^L + N_0^R)$, and all higher order terms (in β and A_0) have been dropped. Thus, the measured asymmetry will be biased by an amount proportional to the rate dependence of the efficiency.

The rate dependence of the reconstruction efficiency was studied[123] using a Monte Carlo technique dubbed "*pulse fiction*"[14]. The idea is to analyze two consecutive spills in one spectrometer, and then merge them on the level of raw data taking into account dead time, etc. Thus, the merged pulse will appear as taken at "double rate". The ratio of the number of electrons in merged pulses to the sum of the number of electrons in the original pulses determined the product $\alpha \equiv \beta \langle N \rangle$. Since electron efficiency depends primarily on the environmental rate (*i.e.* the total rate in the detectors and not only the electron rate), the individual coefficients α_{cher}, α_{hodo}, and α_{shw} were determined for Cherenkovs, hodoscope, and the shower counter by merging raw data from individual detectors. The rate dependence correction to the measured asymmetry is given similarly to Eq. (3.39) by

$$\Delta A^{\text{rate}} \equiv A_0 - A^{\text{meas}} = \alpha_{\text{cher}} A_{\text{cher}} + \alpha_{\text{hodo}} A_{\text{hodo}} + \alpha_{\text{shw}} A_{\text{shw}} , \tag{3.40}$$

where A_{cher}, A_{hodo}, and A_{shw} are asymmetries in rates for individual detectors. The coefficients $\alpha_i \equiv \beta_i \langle N_i \rangle$ for every detector and the coefficient α_{tot} (determined by merging all detectors at the same time) are shown in Fig. 3.33 for all polarized

[14]The name was inspired by a popular, as of time of analysis, motion picture.

^{3}He cells.[123] There is an obvious correlation of the rate dependence to the overall rate in the spectrometers. The runs taken at the high beam current of $\approx 9 \cdot 10^{10}$ electrons/spill (target cells Dave, Riker, Bob, SMC, and Generals) show a stronger rate dependence than the runs at the intermediate current of $\approx 5 \cdot 10^{10}$ electrons/spill (target cells Hermes, Prelims, and Chance), or the low current of $3 \cdot 10^{10}$ electrons/spill (target cell Picard). The rate dependence was also sensitive to the beam quality that was improving over the course of the experiment, and to the target window thickness. There is an apparent jump in the rate dependence in the 5.5° spectrometer for target Chance. This target had the thickest windows, and unlike the 2.75° spectrometer, the acceptance of the 5.5° spectrometer was fixed. Note also that $\alpha_{\rm tot}$ is usually somewhat higher than the sum of rate dependences for individual detectors. This is due to subtle correlations that exist in tracking. If we assume that the rate asymmetries in the individual detectors are uncorrelated (which is a good approximation since the detectors are sensitive to different types of the background), these correlations should be ignored in Eq. (3.40).

The rate dependence was typically $6-8\%$ in the 2.75° spectrometer and $3-5\%$ in the 5.5° spectrometer, and showed mild dependence on electron momentum.[123]

3.7 DST analysis

The Data Summary Tapes contained pre-processed information about the Cherenkov hits, shower clusters, and tracks in the spectrometers, as well as information about the beam charge, position, helicity etc. A typical size of a DST file for one run was about 130 Mbytes – more than factor of six reduction in size compared to the raw data tapes. The main advantage of using DST tapes was the processing speed. Contrary to the raw data analysis, the DST analysis code was not CPU-intensive, and the speed was limited only by the I/O throughput. Thus, the entire data set of E154 could be analyzed in less than three days. The analysis speed

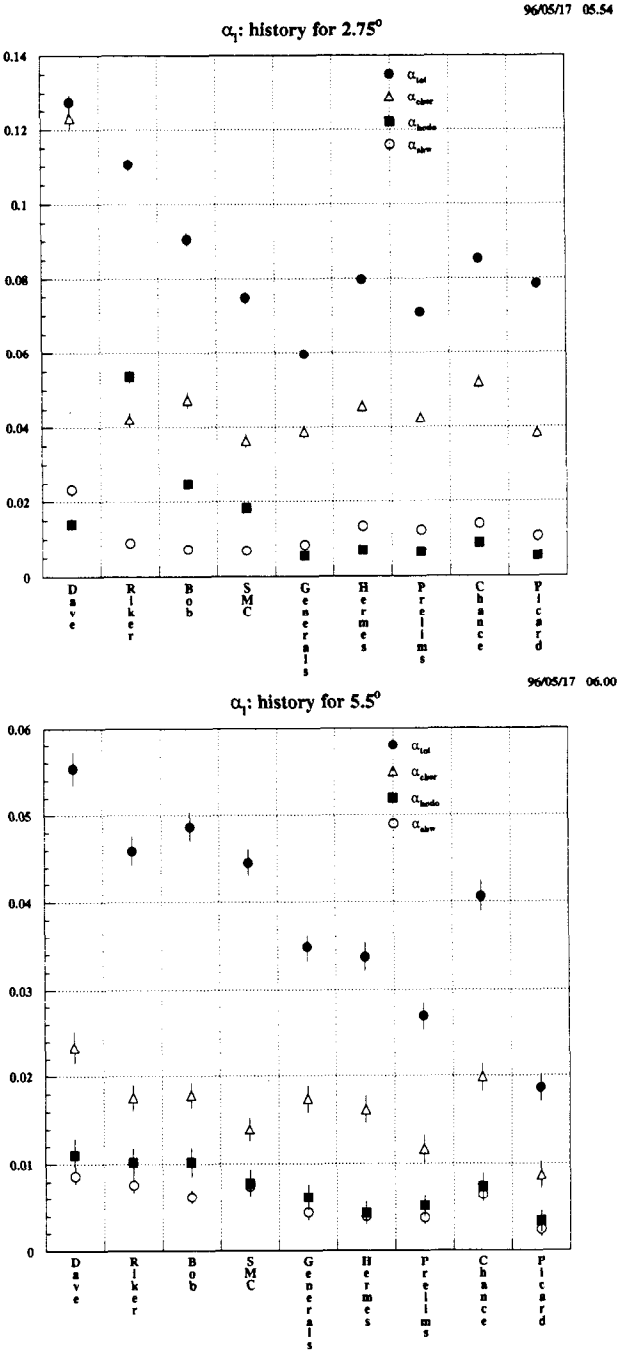

Fig. 3.33. Rate dependence coefficients α (see text) for the 2.75° (top) and 5.5° (bottom) spectrometers.

offered great flexibility in studying detector performance, effects of electron cuts, pion contamination, and other systematic effects.

For each run, the DST analysis code counted events satisfying certain electron (or pion) definitions, and placed them in appropriate x and Q^2 bins for each beam helicity. The summary files produces for each run were then used by a separate program to calculate physics asymmetries.

3.7.1 Kinematics

The kinematics of each event is determined by tracking. The scattering angle of an electron is given by

$$\vartheta = \sqrt{(\theta_0 + \theta)^2 + \phi^2} \tag{3.41}$$

where $\theta_0 = -2.75°(+5.5°)$, and θ and ϕ are scattering angles in non-bend and bend planes respectively. Track momentum p determines the scattered electron energy E'. The kinematic variables are calculated as follows:

$$\begin{aligned} Q^2 &= 4EE' \sin^2 \vartheta/2 \\ x &= \frac{Q^2}{2M(E-E')} \\ W^2 &= M^2 + Q^2 \frac{1-x}{x} . \end{aligned} \tag{3.42}$$

The beam energy is E and M is the proton mass.

3.7.2 Run selection

The polarized data taking started with run 1329 on October 9, 1995 (target Dave) and ended with run 3785 on November 20, 1995. The total of 1467 polarized ^{3}He runs were written to tape. Only 956 of them were used for the asymmetry analysis. Below, we describe runs that did not satisfy the selection criteria. Some of the cuts apply to the reference cell runs as well (cuts not related to polarization or beam asymmetries).

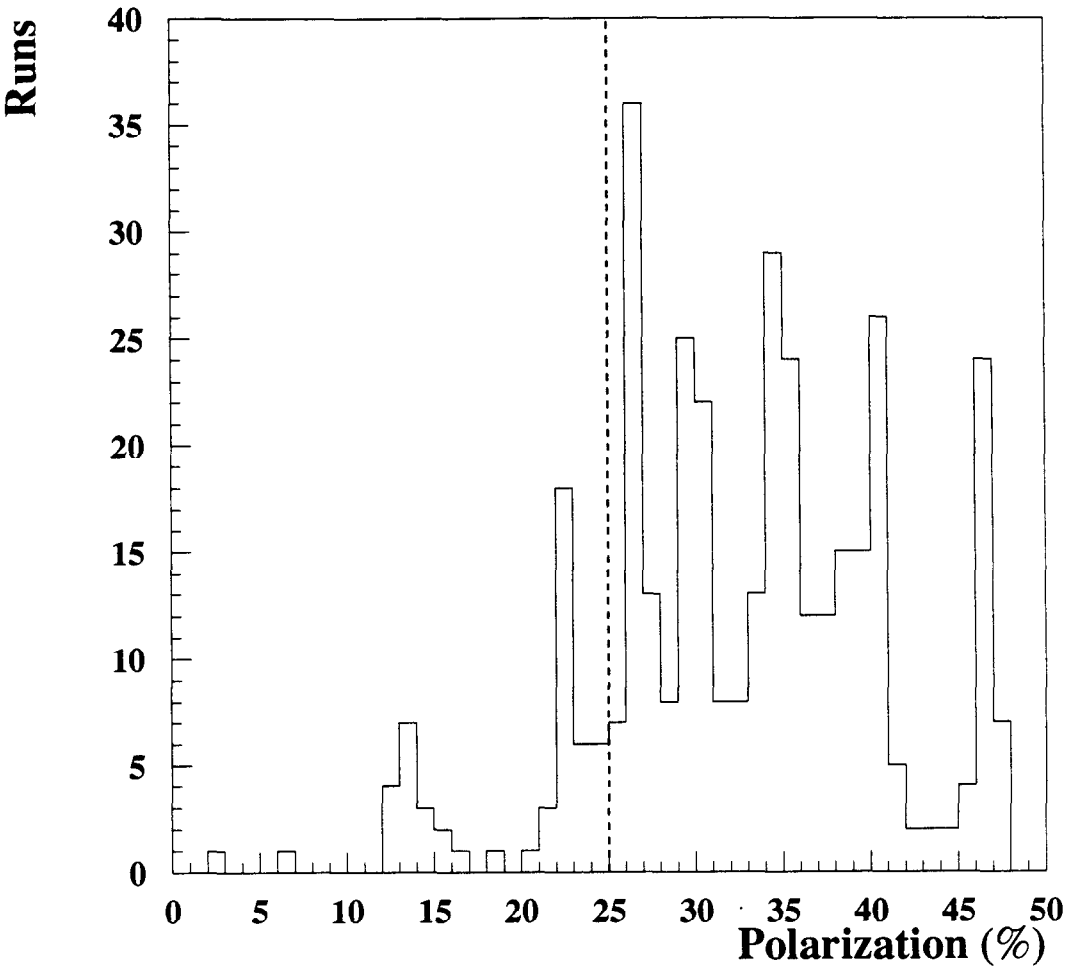

Fig. 3.34. Distribution of target polarization measurements. Only runs with polarization above 25% (dashed line) are included in the asymmetry analysis.

3.7.2.1 Target polarization

Only runs with the target polarization higher than 25% were used in the asymmetry analysis. Most of the runs that failed the cut were taken either during the spin-up of the target or in in special target tests, and polarization was not very stable. The distribution of the target polarization measurements is shown in Fig. 3.34. The target polarization cut eliminated 190 runs. If included, these runs, however, would have a negligible impact on overall statistics of E154.

3.7.2.2 Beam and hardware problems

Certain runs, identified as "bad" by a shift crew and marked in the log book, were actually written to tape. Such runs were removed from the data sample. The beam problems listed in log books included test runs (when the beam or spectrometer configuration was not normal), runs with frequent beam trips and/or poor beam quality, runs affected by hardware failures or hardware changes, and runs affected DAQ or control software problems. We also removed runs that were shorter than 30,000 spills (a typical run size was 200,000 spills). 270 runs have been eliminated.

3.7.2.3 Charge and beam position asymmetry

The raw asymmetries measured in our experiments are small, typically, on the order of $10^{-4} - 10^{-3}$. In order to minimize systematic effects, it is important to keep beam-related asymmetries to the minimum. The rate dependence of electron efficiency was typically on the order of 10% (see Section 3.6), so the beam charge asymmetry has to be below 10^{-3} in order to keep asymmetry bias below 10^{-4} for every run. The distribution and history of beam charge asymmetry is shown in Fig. 3.35. We have cut runs with charge asymmetry $|A_{\text{charge}}| = |(Q_L - Q_R)/(Q_L + Q_R)| > 5 \cdot 10^{-4}$. A total of 34 runs have been eliminated.

Another potential source of systematic biases in measured raw asymmetry is asymmetry in beam position. Due to the variation of the target cell window thickness, spectrometer rate depends on the relative positions of the beam and the target cell,[114] as was determined by moving an empty reference cell vertically through the beam. This dependence is illustrated in Fig. 3.36. The distribution of beam position asymmetries is shown in Fig. 3.37.[125]

For asymmetry analysis, we select runs with position asymmetries $|\langle x_L \rangle - \langle x_R \rangle| \leq 0.004$ mm, and $|\langle y_L \rangle - \langle y_R \rangle| \leq 0.005$ mm. Here $\langle x_{L(R)} \rangle$ is the average beam position

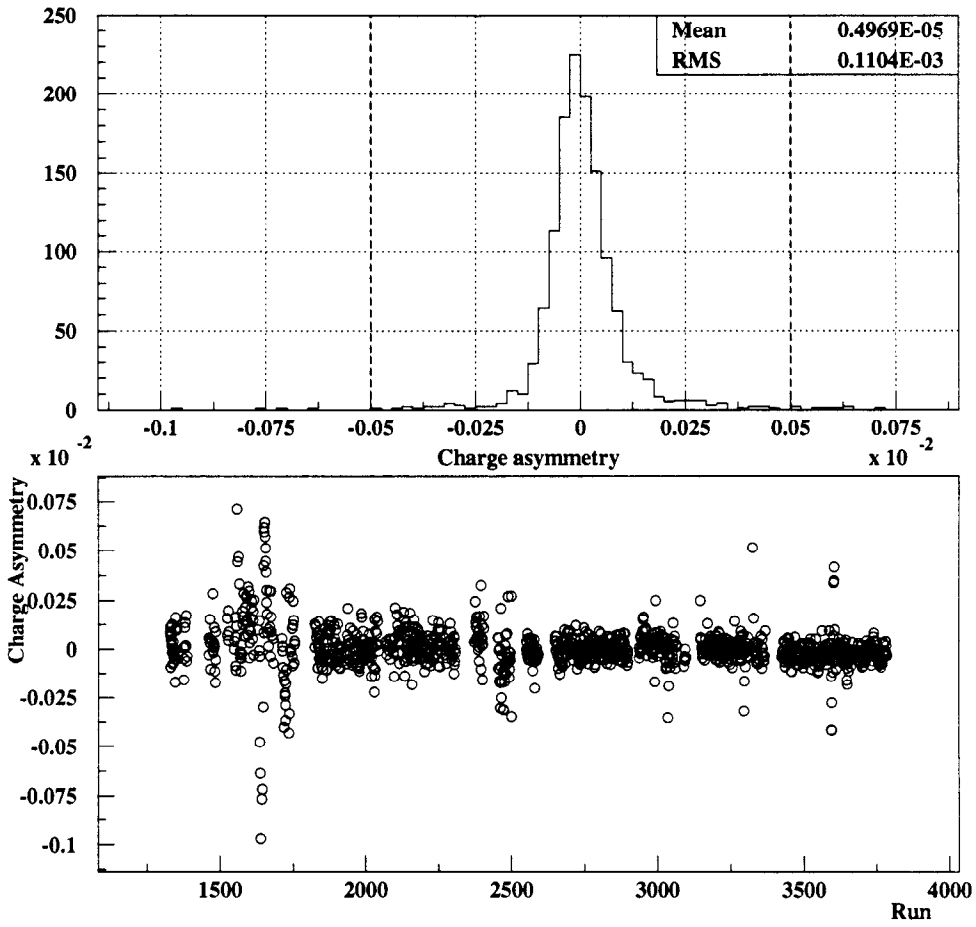

Fig. 3.35. Distribution (top) and history (bottom) of beam charge asymmetry versus E154 run number. The applied cut is shown as a dashed line.

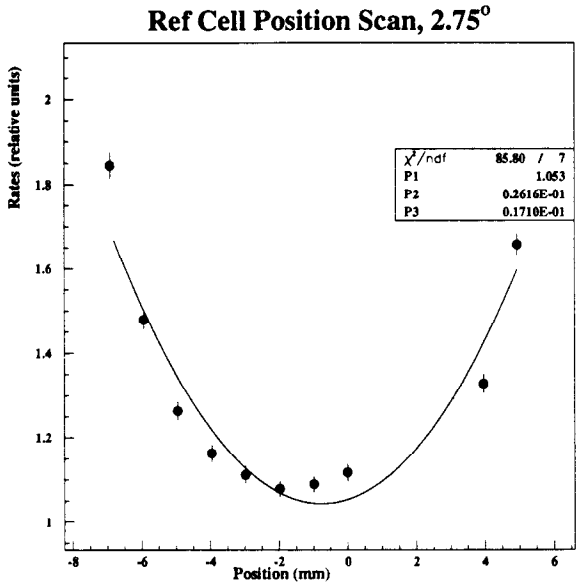

Fig. 3.36. Dependence of the electron rate in the 2.75° spectrometer on the relative beam position. Overlaid is a quadratic fit. Courtesy of Piotr Zyla.

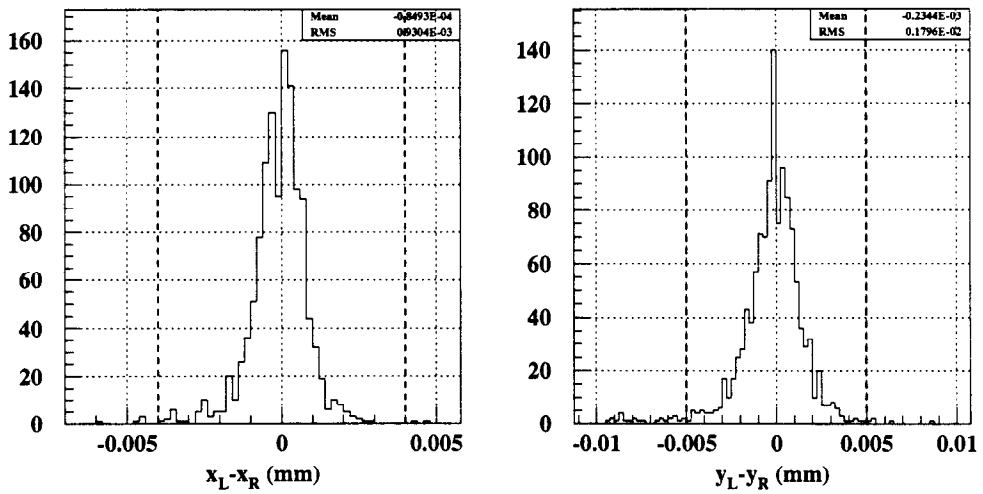

Fig. 3.37. Difference between average over run beam positions for left and right helicities. Cut values are shown by dashed lines.

for "left" ("right") electrons in x. The cut eliminates 33 polarized runs. It ensures that the position-dependent bias to the raw asymmetry does not exceed $0.5 \cdot 10^{-4}$.

3.7.2.4 Polarization bit

The polarization state of the beam was sent to the Data Acquisition System via four physically distinct pathways: the PMON line, Mach line, Pockels Cell High Voltage Line and the Veto Bits. Each measurement delivered a two-bit combination, where the combination '01' referred to positive helicity photons and '10' meant that the photons incident on the photocathode were of negative helicity. Combination '00' in the PMON meant that the beam is unpolarized, and '11' marked an error condition. During E142, reading of the Veto module was found to fail at high rates[126] that caused a bias in the asymmetry analysis. The problem was solved prior to E154.

The electron helicity was governed by a pseudo-random bit generator at the electron source. The seed of the generator can be determined by measuring the polarization state of 33 consecutive spills.[92] After the seed is determined, the polarization state of any subsequent spill can be predicted if the sequence number of the spill is known. Such a sequence number was provided by the PMON module. The predictor code thus provided a fifth determination of the spill helicity state.

All methods typically agreed to $\approx 10^{-5}$ level[92] (the failure rate can only be tested to $\approx 5 \cdot 10^{-6}$ level for a given run since the typical run size is 200,000 spills). However, 18 runs were found to have a failure rate of more than $10 \cdot 10^{-4}$,[92] *i.e.* comparable to the raw asymmetry. These runs have been excluded from the asymmetry analysis. In addition, for 35 runs in the range 2454 through 2494, the Veto signal was in error.[92] Those runs are included in the asymmetry analysis and the polarization state is determined by other four measurements.

3.7.3 Event selection

3.7.3.1 Beam cut

The purpose of the beam cut was to get rid of spills with beam properties very different from the average, for these may potentially bias the measured electron asymmetry. Such a cut should be reasonably mild, on another hand, as tight cuts have lower efficiency and may adversely affect the electron asymmetry if a particular beam parameter has large left-right asymmetry. We applied a cut of 4σ to the following beam quantities:

1. Beam charge.
2. Good spill ADC.
3. Bad spill ADC.
4. Beam width at the wire array in x.
5. Beam width at the wire array in y.
6. Beam position at the wire array in x.
7. Beam position at the wire array in y.
8. Beam position at the TWBPM in x.
9. Beam position at the TWBPM in y.

The distributions of bad spill ADCs and beam position in y before and after the cut are shown in Fig. 3.38. The number of spills rejected by each cut is given in Fig. 3.39.

Cuts (1), (3), and (7) are most important. We believe this is justified. Big fluctuations in the incident charge could introduce fluctuation in electron rate due

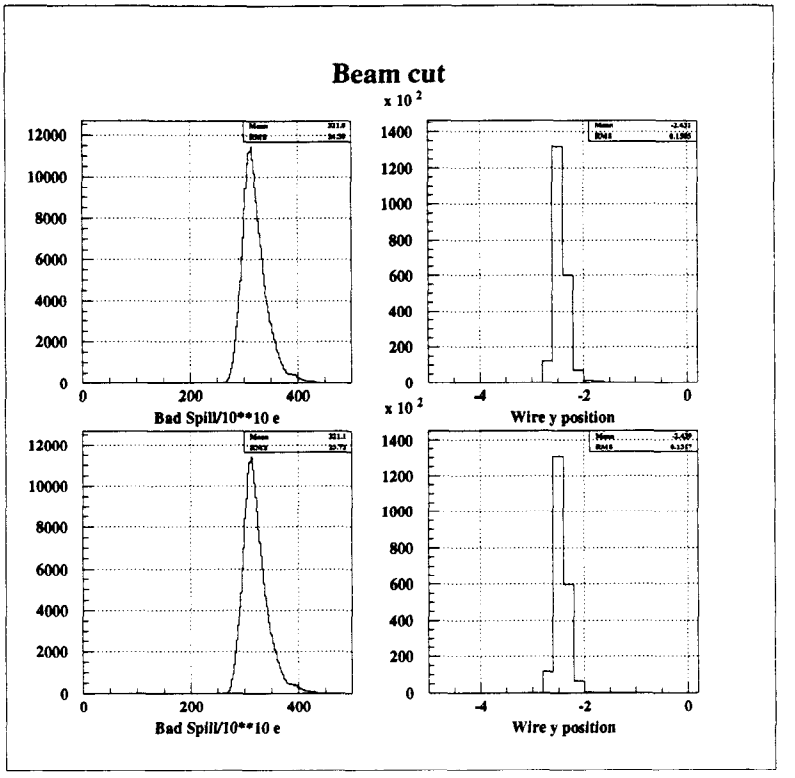

Fig. 3.38. Distribution of two quantities used in the beam cut before (top) and after (bottom) the cut. Bad spill ADC is shown on the left and the beam position at the wire array in y is on the right. The tails of both distributions are smaller after the cut.

to rate dependence. The dependence of electron rate on the beam position has been observed (see Fig. 3.36) and is not insignificant. The bad spill ADC, positioned in the alcove, has historically been an indicator of overall beam quality.

In addition to the 4σ cut, we selected only spills with $0.5 \leq Q \leq 12$ (in units of 10^{10} electrons: cut # 0 in Fig. 3.39). This mainly gets rid of the "witness" pulses used for accelerator tuning. We also require the match of all four hardware polarization signals (PMON, Mach Line, Scaler, and Veto: cut # -1 in Fig. 3.39)[15].

We calculated the mean and RMS of every value used in the cut every 1056 spills (32 cycles of the random number generator for the polarization bits). These values

[15]For runs between 2440 and 2495, the Veto module is believed to have been malfunctioning[92], so we are using a three-fold coincidence.

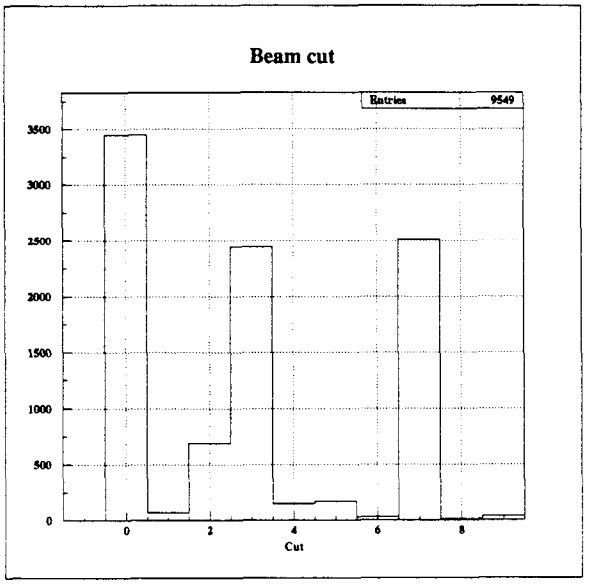

Fig. 3.39. Number of spills rejected by each beam cut. See text for explanation of cut numbers.

are then applied to the next 1056 spills. Thus, the cut is "sliding", it follows slow changes in the beam quantities. On another hand, short beam trips and random "flyers" that last less than $\approx$ 9 sec are rejected.

3.7.3.2 Electron selection

For systematic studies, we implemented 52 electron definitions and 14 pion definitions. The main definition for the asymmetry analysis was chosen to maximize efficiency (statistics), minimize pion contamination, and minimize rate dependence. The electron definition, found as a best compromise among the criteria above and denoted as "definition 33", is defined by the following set of cuts:

1. Class 1 track with both Cherenkov in coincidence;

2. Acceptance cut passed;

3. 8 GeV $< p <$ 48.3 GeV;

4. $Q^2 \geq 1$ GeV^2, $W^2 \geq 8$ GeV^2;

5. One of the Cherenkov signals greater than 2.5 photoelectrons ("AND-OR" cut)

6. $E > 7.5$ GeV;

7. $E/p \geq 0.8$;

8. Shower shape $\chi \leq 0.045$ for $p < 30$ GeV (see Eq. (3.16));

9. No DAQ failures for the spill in the given spectrometer.

The acceptance cut (2) is defined by

$$-\theta_{\max} \leq \theta \leq \theta_{\max}, \quad \phi_{\min} \leq \phi \leq \phi_{\max}, \tag{3.43}$$

where θ and ϕ are the horizontal and vertical scattering angles at the target limited by $\theta_{\max} = 0.006(0.013)$, $\phi_{\min} = -0.031(-0.028)$, and $\phi_{\max} = 0.005(0.01)$ for $2.75°(5.5°)$ spectrometer (all angles are relative to the central spectrometer angle and are in rad). The relation between the Cherenkov peak voltage and number of photoelectrons in cut (5) is given in Section 3.3.

The main differences with the SLAC analysis are in cuts (5), (7) and (8). The differences between the shower shape χ cut and neural network cut used at SLAC (cut (8)) are discussed in Section 3.4. The "AND-OR" cut (5) was found to have a smaller rate dependence by about 1%[114] compared to the "AND" cut used at SLAC (which required both Cherenkov hits to be higher than 25 FADC units). It also had a slightly higher efficiency (by about 2.5%) than the "AND" cut with a comparable pion rejection power. In addition to the $E/p \geq 0.8$ cut (7), SLAC analysis required a cut on high side of the peak $E/p \leq 1.2$. This cut was found to have a significant rate dependence[114] (about 2%, or more than a factor of two higher than low E/p cut) without compensating gain in the pion rejection.

3.8 Asymmetry analysis

Summary files produced for each run in the DST analysis were used to extract the raw experimental asymmetries $A_{\parallel}^{\rm raw}$ and $A_{\perp}^{\rm raw}$:

$$A_{\parallel}^{\rm raw}(x) = \frac{(N(x)/Q)^{\downarrow\Uparrow} - (N(x)/Q)^{\uparrow\Uparrow}}{(N(x)/Q)^{\downarrow\Uparrow} + (N(x)/Q)^{\uparrow\Uparrow}} , \tag{3.44}$$

where $N(x)/Q$ is the number of events in each helicity state passing the analysis cuts normalized to the incident charge. The expression for $A_{\perp}^{\rm raw}$ is analogous to Eq. (3.44). The Bjorken x and four momentum transfer squared Q^2 of an event were determined from the momentum and scattering angle of reconstructed electrons. The statistical error, in the limit of small $A_{\parallel}^{\rm raw}$ (the raw electron asymmetries are on the order of 10^{-3}) is given by

$$\sigma(A_{\parallel}^{\rm raw}) = \frac{\sqrt{(N(x)/Q^2)^{\downarrow\Uparrow} + (N(x)/Q^2)^{\uparrow\Uparrow}}}{(N(x)/Q)^{\downarrow\Uparrow} + (N(x)/Q)^{\uparrow\Uparrow}} . \tag{3.45}$$

The raw experimental asymmetries in Eq. (3.44) must be corrected before they can be used in Eq. (1.23) and Eq. (1.24) to calculate the spin-dependent structure functions. First, we account for the fact that the target and beam were not completely polarized, and that the detected electrons can be scattered from the unpolarized materials in the target such as glass cell end windows. The correction is applied by multiplying the raw asymmetries by a factor $1/(fP_bP_t)$ (*cf.* Eq. (1.10) and Eq. (1.11)). Second, some events that passed our cuts are not the true DIS events whose asymmetry we are interested in. Furthermore, the data sample is contaminated to a small degree by pions misidentified as electrons. In addition, a certain portion of electrons came from the charge symmetric processes (such as $\pi^0 \to e^+e^-\gamma$, $\gamma \to e^+e^-$ etc.). Such events should be subtracted from the data sample. The raw asymmetries are also corrected for rate dependence of asymmetries as discussed in Section 3.6 and radiative effects. Finally, a small correction is applied to account for a parity-violating asymmetry coming from the interference of the γ

and Z^0 exchange amplitudes. Combining all corrections, the physics asymmetry that can be used to calculate the polarized structure functions takes the form:

$$A^{\text{phys}} = \frac{A_{e^-}^{\text{raw}} + \Delta A^{\text{rate}} - P_b A^{\text{EW}}}{f P_b P_t} + \Delta A^{\text{RC}} , \tag{3.46}$$

where $A_{e^-}^{\text{raw}}$ is the raw asymmetry (with backgrounds subtracted), ΔA^{rate} is the rate dependence correction of Eq. (3.40), A^{EW} is the electro-weak parity-violating asymmetry, ΔA^{RC} is the additive radiative correction, f, P_b, and P_t are the ^{3}He dilution factor, beam, and target polarizations, respectively.

We will discuss the corrections mentioned above in the following Sections.

3.9 Background subtraction

The sample of events that passed our electron cuts is not purely electrons coming from the DIS events. First, charged hadrons (pions, and to a much lesser degree kaons) and muons could be misidentified as electrons. Moreover, a certain portion of electrons we detected came from the charge symmetric processes (such as charge symmetric decays and pair production). These events dilute the DIS sample, and could even distort the asymmetry if the production processes have significant spin dependence. Let π/e and A_π denote the fraction of misidentified hadrons (relative to the number of all electrons) and pion asymmetry, respectively. Similarly, let e^+/e^- and A_{e^+} denote the fraction of electrons from the charge symmetric processes and their asymmetry. The asymmetry of purely DIS events is then given by (x dependence omitted)

$$A_{e^-}^{\text{raw}} = \frac{1}{1 - e^+/e^-} \left[\frac{A^{\text{raw}} - (\pi/e) A_\pi}{1 - \pi/e} - (e^+/e^-) A_{e^+} \right] . \tag{3.47}$$

We will discuss each background separately.

3.9.1 Pion background

3.9.1.1 Pion contamination

The number of negatively charged hadrons (referred to as π^- hereafter) in the electron data sample was estimated by comparing the E/p spectrum of well-identified pions and the E/p distribution of the events passing our cuts. As an example, we will take the electron "definition 2", that requires 2 Cherenkov signals in coincidence higher than 1.5 photoelectrons, $E/p \geq 0.8$, and does not use the shower shape cut. Pions can be identified requiring a veto in both Cherenkovs with a negligible electron contamination. The E/p spectrum of events satisfying definition 2 at low E/p is dominated by pions. Matching two spectra at low E/p (where both spectra have a peak due to pions that do not shower), we can estimate the size of a pion tail leaking under the electron E/p peak (see Fig. 3.40). The pion contamination π/e is given by the ratio of the number of pions to the number of electrons with $E/p \geq 0.8$. The same procedure was applied to the electron definitions that do use the shower shape χ cut, but the statistical uncertainty was bigger in those cases.

The pion contamination for the worst case, target Dave (data were taken at "high" current of $9 \cdot 10^{10}$ electrons per spill) , is plotted in Fig. 3.41 for definition 33. Even for this target, it does not exceed 10%. The average pion contamination at low x in the 2.75° spectrometer was 2.8% and smaller at higher values of x. Two independent methods were employed to check the estimates of the pion contaminaiton[127] and were found to yield similar results. The error on π/e is dominated by systematics (estimated as a discrepancy between different methods used to determine the contamination) and is taken to be 50% of the value of π/ϵ.

3.9.1.2 Pion asymmetry

Pion asymmetry was measured using the DST tapes produced in the dedicated production (in which we included class 2 tracks and lifted the energy cut-off in

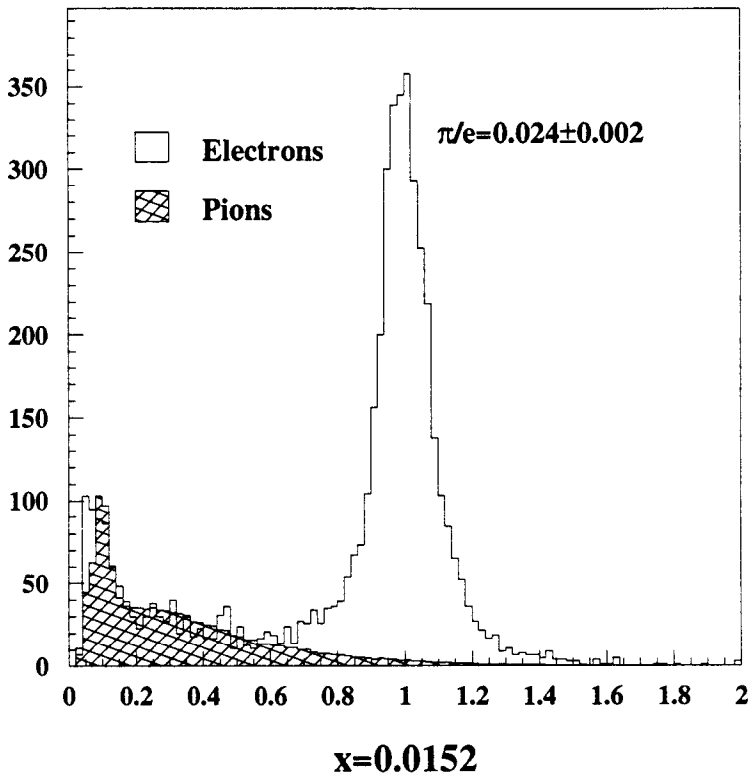

Fig. 3.40. Pion contamination in the 2.75° spectrometer at $x = 0.0152$. Error is statistical. See text for discussion.

clustering (see Section 3.4.2). The pion asymmetry $A_{\parallel}^{\pi}$ (divided by the dilution factor and beam and target polarizations) for both negatively and positively charged pions is shown in Fig. 3.42. This is perhaps the largest data sample on asymmetry in the inclusive hadron photo-production. The asymmetry is approximately three times smaller than the electron asymmetry and is *not* consistent with zero. It is interesting to note that the π^+ asymmetry is almost a factor of two bigger (in absolute value) than the π^- asymmetry.

3.9.2 Charge symmetric background

The event rate of electrons originating in the charge symmetric processes was measured by reversing the polarity of the spectrometer magnets. The positron

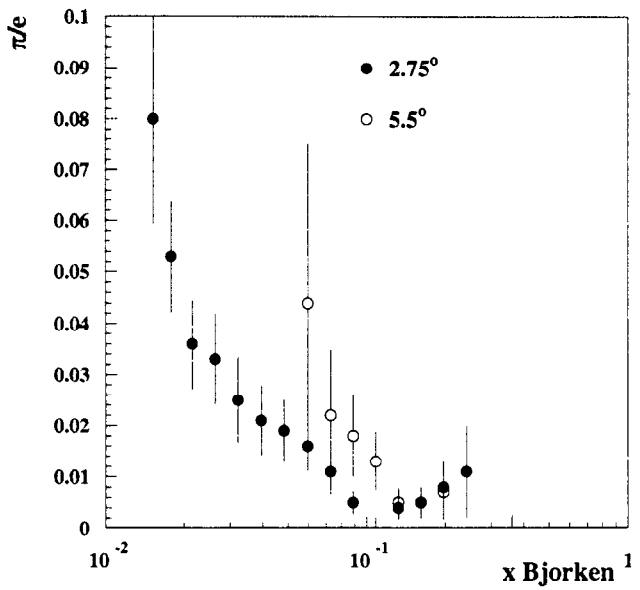

Fig. 3.41. Pion contamination in the 2.75° (solid circles) and 5.5° (open circles) spectrometers versus Bjorken x for electron definition 33, target Dave. Error is statistical.

component of the background was measured and assumed equal to the electron component of the charge symmetric background.

A total of 81 positron runs (with the longitudinally polarized target) with target cell Picard was used to determine the ratio e^+/e^- and the asymmetry A_{e^+}. The extracted "positron contamination" e^+/e^- is shown in Fig. 3.43 and the positron asymmetry (divided by the dilution factor and beam and target polarizations) is shown in Fig. 3.44.

The positron rate was also measured with the empty and full reference cells. It is believed that the main source of the charge symmetric background is photoproduction (or electro-production with $Q^2 \approx 0$) via processes $\gamma p \rightarrow \pi^0 p$, $\pi^0 \rightarrow e^+e^-\gamma$ and $\gamma \rightarrow e^+e^-$ etc. The rate of real (or almost real) photons depends on the radiation length (thickness) of the target and the rate of the photon conversion is approximately linear with it, hence the positron rate increases as a second (or even higher) power of the target thickness. Since the electron rate is to the zeroth order

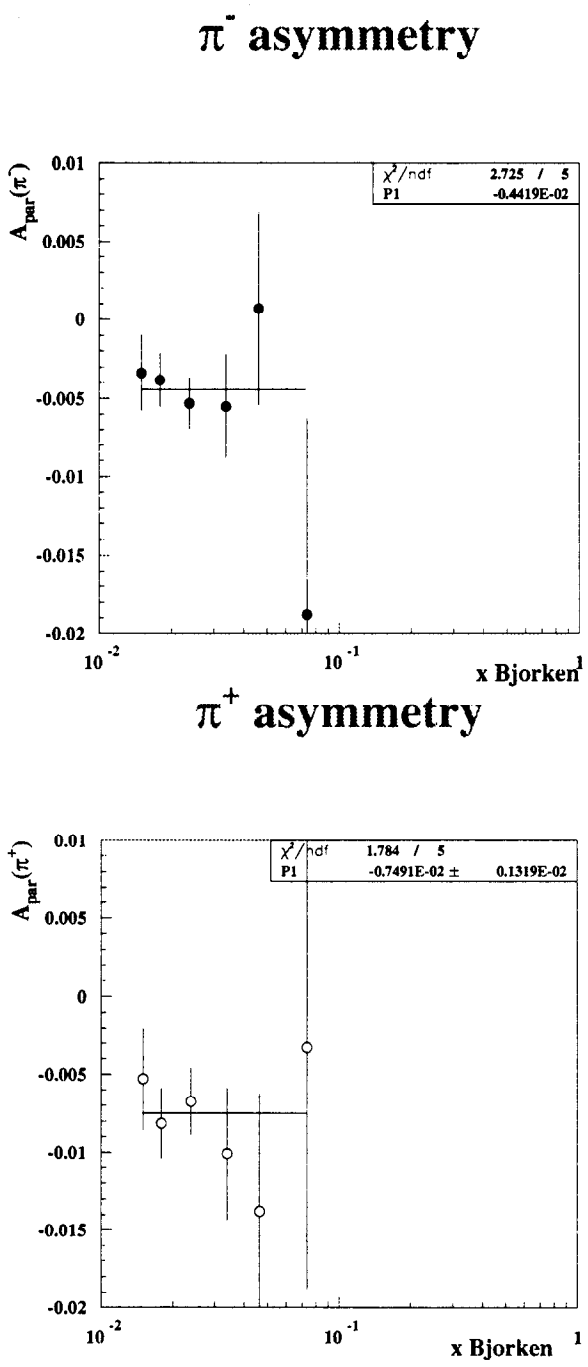

Fig. 3.42. Asymmetries for production of negative (top) and positive (bottom) pions as a function of x.

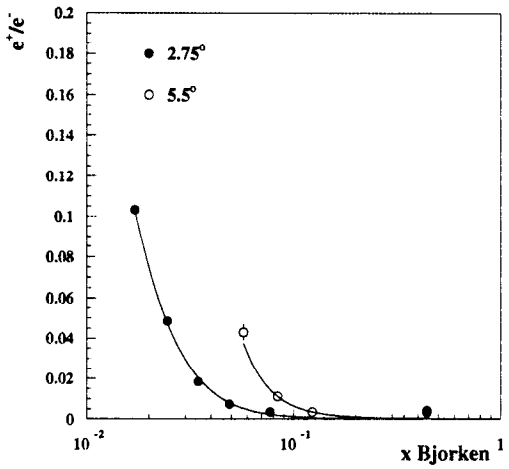

Fig. 3.43. Ratio e^+/e^- in 2.75° (solid circles) and 5.5° (open circles) spectrometers as a function of x. Error bars are statistical only.

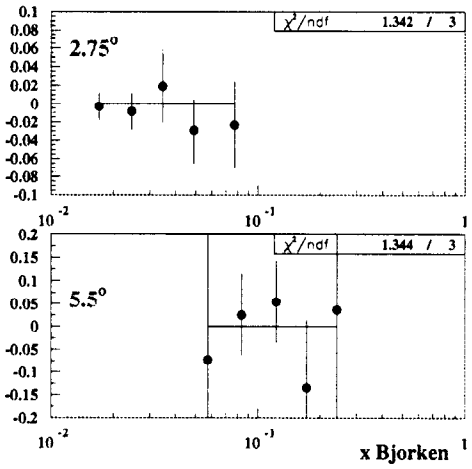

Fig. 3.44. Positron asymmetry measured in 2.75° (top) and 5.5° (bottom) spectrometers as a function of x. The χ^2 for the asymmetry being consistent with zero is given for reference.

proportional to the target thickness, the ratio e^+/e^- is expected to be different for different target pressures and geometries. The variation of about 20% was observed with different empty reference cells, and about 10% with full reference cells. Since the positron runs were not taken with every polarized cell, we assign a 20% systematic error to the ratio e^+/e^-.

The positron asymmetry is found to be consistent with zero, albeit with large uncertainty. It is also consistent within errors with both π^- and π^+ asymmetries. For the electron asymmetry correction, we assume the positron asymmetry $A_{e^+} = 0$ and use the statistical errors on the measurement to estimate the systematic uncertainty on g_1^n due to the charge symmetric backgrounds. This uncertainty dominates the systematic error on g_1^n in the lowest x ($x = 0.017$) where the e^+/e^- ratio is the biggest (see Section 4.2). This error could be significantly decreased if a theoretical guidance regarding the physics of the charge-symmetric backgrounds was available. For instance, if the dominant mechanism for the creation of the e^+e^- pairs is the photo-production (either direct or via the π^0 decay), the same process that dominates the pion production, it seems feasible (on the basis of isospin symmetry) that the positron asymmetry is bound by π^- and π^+ asymmetries. If we used such a bound, the systematic uncertainty in the lowest x would have decreased by $\approx 40\%$. On another hand, if we averaged the positron data over all x (relying on an assumption that the kinematic dependence of the asymmetry is not very strong), the systematic error at $x = 0.017$ would have decreased by $\approx 30\%$. Lacking the theoretical guidance, we have taken a conservative approach and subtracted the charge-symmetric background bin-by-bin.

3.10 Dilution Factor

In order to extract the physics asymmetries $A_{||}^{\text{phys}}$ and $A_{\perp}^{\text{phys}}$ for ^{3}He, we should correct for events that have originated from scattering off the unpolarized material in the target. The ratio

$$f = \frac{\text{number of electrons scattered off } ^3\text{He}}{\text{total of number of events}} \tag{3.48}$$

is called a dilution factor. This factor is roughly 1/2 where the rest of the events come from the glass end windows and a small amount of nitrogen in the target. The dilution factor can be calculated using measured unpolarized cross sections, and knowing the composition of the target.[128] The dilution factor can also be measured with the reference cells by varying ^{3}He pressure. Both methods are discussed below.

3.10.1 Theoretical dilution factor

The theoretical expression for the dilution factor is given by

$$f(x,Q^2) = \frac{R_{\rm He}(x,Q^2)}{R_{\rm He}(x,Q^2) + R_{\rm N}(x,Q^2) + R_{\rm gl}(x,Q^2)} \tag{3.49}$$

where $R_{\rm He,N,gl}$ are the rates of scattering off ^{3}He, N_2, and glass. These are given by

$$R_i(x,Q^2) = (Z_i\, F_2^p(x,Q^2) + (A_i - Z_i)\, F_2^n(x,Q^2))\, f_{\rm RC}\, f_{\rm EMC}(A_i,x)\, n_i\, L_i\ , \tag{3.50}$$

where A_i and Z_i are the atomic weight and number of each target component, F_2 is the unpolarized structure function,[129] $f_{\rm RC}$ is the unpolarized multiplicative radiative correction, and $f_{\rm EMC}$ is the EMC factor[74] that takes into account effects of nuclear binding and motion. The atomic density and the length of the material i are n_i and L_i.

For the calculation, we use F_2 parameterization from Ref. [129], and parameterizations of the EMC effect from Ref. [130,131]. The parameters of the target model are given in Ref. [132] (see also Section 2.5). On average, 53% of all events are coming from scattering off ^{3}He, 43% off glass, and the remaining 4% off N_2. The biggest systematic error is due to the uncertainty in radiative corrections, that corresponds to uncertainty and variations of the target model, and ranges from 5% at low x to 0.7 at mid-x. Uncertainties in window thickness and F_2 each contribute $\approx 1\%$ to the error on dilution factor.

3.10.2 Experimental dilution factor

An important feature of our experiment is the ability to measure the dilution factor experimentally using the reference cells. Reference cells are targets with geometry similar to that of the polarized ^{3}He targets, but that could have a variable ^{3}He pressure. To the extent that the geometries of the reference and polarized target cells are exactly the same, the dilution factor can be measured as

$$f(x,Q^2) = \frac{R_{\text{full}}(x,Q^2) - R_{\text{empty}}(x,Q^2)}{R_{\text{polarized}}}, \tag{3.51}$$

where $R_{\text{full,empty,polarized}}$ are scattering rates from the full and empty reference cells and polarized ^{3}He target, respectively. In reality, we extract the dilution factor by measuring the slope of event rate versus ^{3}He pressure and comparing it to the scattering rate from the polarized cell:

$$f = \frac{\partial R_{\text{ref}}}{\partial P_{\text{ref}}} \frac{P_{\text{polarized}}}{R_{\text{polarized}}} \frac{L_{\text{polarized}}}{L_{\text{ref}}}, \tag{3.52}$$

where P_{ref} and $P_{\text{polarized}}$ are the reference and polarized cell pressure, and L_{ref} and $L_{\text{polarized}}$ are the lengths of the reference and polarized cells. The scattering rates are corrected for rate dependence, and for charge symmetric and hadronic backgrounds.

3.10.3 Dilution factor results

The comparison of the theoretical and experimental dilution factor from target cell Picard is shown in Fig. 3.45. The agreement is generally very good. The experimental results are limited by statistics, especially at high x in the 5.5° spectrometer. For the asymmetry analysis, we use the theoretical values. For each target cell, we add in quadrature the average disagreement between two methods (on average, less than 1%) to the error on the theoretically calculated dilution factor. The average error on dilution factor, weighted by statistical error on $A_{||}$ is 5.1%.[128]

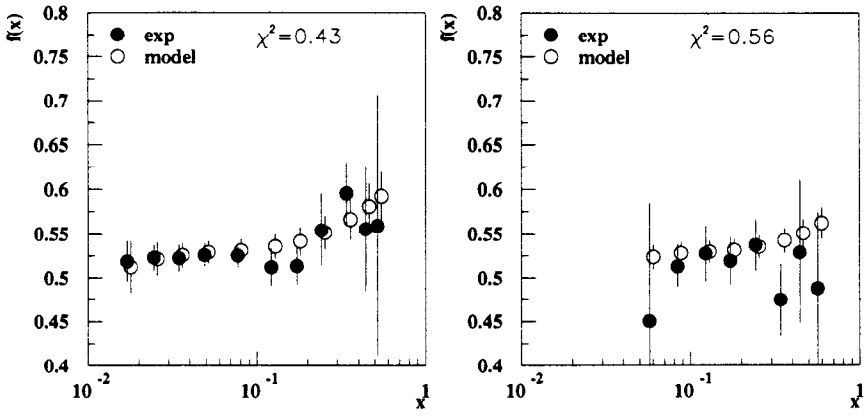

Fig. 3.45. Comparison of the theoretically calculated (open circles) and experimentally determined (closed circles) dilution factor for the 2.75° (left) and 5.5° (right) spectrometers.

3.11 Radiative corrections

The structure functions $g_1^n(x, Q^2)$ and $g_2^n(x, Q^2)$ are defined in the Born limit, *i.e.*, for a single virtual photon exchange in the deep inelastic regime. However, experimentally observed lepton-nucleon scattering includes contributions from higher order processes as well as from elastic, quasielastic, and inelastic tails. In addition, electrons may lose energy before or after scattering due to bremsstrahlung or ionization in external material (target cell entrance and exit windows and side walls). These processes modify the measured asymmetry in Eq. (1.10), so corrections have to be applied in order to extract Born asymmetries.

The radiative corrections are traditionally divided into "*internal*" and "*external*". The internal effects are those occurring at the ^{3}He nucleus where the inelastic scattering occurs. The electrons are off-shell between the emission of the photon and the nuclear scattering. The external effects are those which modify the electron energy before or after the DIS event, hence, the electrons are on-shell.

3.11.1 Internal radiative correction

In addition to the single-photon exchange, the experimentally observed lepton-nucleon scattering cross sections include contributions from higher order processes. At any $(x_{\rm DIS}, Q^2_{\rm DIS})$, there is radiative leakage from other kinematic points ($x \geq x_{\rm DIS}$, $Q^2 \leq Q^2_{\rm DIS}$ for radiation before, and $Q^2 \geq Q^2_{\rm DIS}$ for radiation after scattering), referred to as elastic, quasielastic, and inelastic tails. Since the asymmetries of the tails are not *a priori* identical to the deep-inelastic Born asymmetries, the measured asymmetry must be corrected. The formalism for calculating the radiative corrections (RC) to spin-dependent DIS has been developed by Kukhto, Shumeiko, and Akushevich[133] and implemented in their Fortran code POLRAD 1.5.[134] An independent code was developed by Linda Stuart[135] based on the formalism of Ref. [133] and produced identical results.

At any kinematic point (x, Q^2), the measured asymmetries are given by

$$A^{\rm meas} = \frac{\Delta\sigma^{\rm Born} V + \Delta\sigma^{\rm tails}}{\sigma^{\rm Born} V + \sigma^{\rm tails}} \,, \tag{3.53}$$

where

$$\sigma^{\rm tails} = \sigma^{\rm el} + \sigma^{\rm qel} + \sigma^{\rm res} + \int_{\tilde{x}\geq x} d\tilde{x} \int d\tilde{Q}^2 \, \sigma^{\rm DIS}(\tilde{x}, \tilde{Q}^2) \tag{3.54}$$

are the contributions from the elastic, quasielastic, resonance, and DIS radiative tails, respectively. The correction due to higher-order processes V is given by

$$V = \delta_R^{IR} + \delta_{\rm vert} + \delta^l_{\rm vac} + \delta^h_{\rm vac} \,. \tag{3.55}$$

Here σ_R^{IR} is the correction due to soft photon emission (where the infra-red divergence is cancelled by a similar contribution to DIS tail[136]), $\sigma_{\rm vert}$ is the lepton vertex correction, $\sigma^l_{\rm vac}$ is the lepton vacuum polarization, and $\sigma^h_{\rm vac}$ is the hadronic vacuum polarization. The soft photon and virtual corrections to the cross section are insensitive to the helicity state; these contributions factorize in Eq. (3.53). Thus, the radiative corrections come entirely from the difference between the Born asymmetry

Table 3.5. Contributions to the measured polarized and unpolarized cross sections at $x = 0.017$ from radiative tails, virtual and external corrections (relative to the Born cross section).

	Elastic	Quasielastic	DIS	Resonance	Virtual	External
Unpolarized	0.12	0.20	0.30	0.06	0.11	−0.02
Polarized	0.11	−0.01	0.02	0.04	0.11	−0.02

and asymmetries of the radiative tails. We will now discuss the contributions from each of the tails.

With the emission of a hard photon by the incident electron before scattering, the energy and Q^2 of the event are lowered. Since the form factors of the nucleons in ^{3}He are roughly proportional to $1/Q^4$ at high Q^2, the probability of scattering quasielastically is enhanced. The asymmetry of the quasielastic scattering, expressible in terms of products of form factors $G_E G_M$ and G_M^2,[137] is different from the DIS asymmetry. Radiative effects thus mix in this asymmetry with the DIS asymmetry in which we are interested. The magnitude of this contribution increases as we move to lower x and Q^2. Details of the nuclear structure of ^{3}He are important in the evaluation of this contribution. Predictions for the S, S', and D percentages of the ^{3}He wave function (see Section 1.6) are used to determine the relative contributions from the quasielastic asymmetries of the protons and neutrons in ^{3}He. The correction due to the elastic scattering off the ^{3}He nucleus is small for the E154 kinematics. The relative contributions of elastic and quasielastic tails to the unpolarized and polarized cross sections are summarized in Table 3.5.

The inelastic tail contribution arises similarly to the processes discussed above. Electrons detected in the spectrometers that undergo hard photon emission before the scattering have their energy E' overestimated. Similarly, bremsstrahlung after the scattering results in underestimation of the scattered electron energy E'. In both cases, the event is assigned a lower value of Bjorken x (and higher value of

Q^2). Therefore, DIS asymmetries from higher x, as well as asymmetries from the resonance region $W^2 < 4$ GeV^2 are mixed into the asymmetry measured at lower x.

3.11.2 External radiative correction

Before and after the DIS event, electrons may lose energy by bremsstrahlung and, to much smaller extent, by ionization in interactions with other target nuclei. Similar to internal effects, these interactions mix the asymmetry at a given kinematic point $x_{\rm DIS}, Q^2_{\rm DIS}$) with asymmetries from a broad region $x \geq x_{\rm DIS}$. Thus, the measured (uncorrected) asymmetries are given in terms of convolutions of polarized and unpolarized cross sections and electron straggling probabilities over this kinematic range. The external radiative corrections are calculated using the formalism of Mo and Tsai.[138]

The external radiative effects depend on the thickness of the material traversed by the electrons before and after the DIS interaction. The dominant source of external radiative corrections are the side walls of the target through which the electrons pass at very shallow angles. The target NMR pickup coils were modified prior to E154, and one of the major contributions to the external radiative corrections, important for E142,[122] was eliminated. Overall, the effect of external radiative corrections to the measured asymmetries is very small.

3.11.3 Calculating the correction

Equation (3.53) can be re-written in terms of the convolution of the Born DIS cross section and the internal (external) bremsstrahlung probabilities (with the helicity indices suppressed):

$$\sigma^{\rm meas}(E_0, E') = \sigma^{\rm Born}(E_0, E') + \int d\epsilon_0 \psi_{\rm in}(\epsilon_0/E_0, E')\sigma^{\rm Born}(\epsilon_0, E') + \int d\epsilon \psi_{\rm out}(E_0, E'/\epsilon)\sigma^{\rm Born}(E_0, \epsilon)\,, \tag{3.56}$$

where E_0 and E' are the initial and final electron energies, and $\psi_{\rm in}$ and $\psi_{\rm out}$ are the straggling probabilities before and after the scattering, respectively. Evaluation of

the integrals in Eq. (3.56) requires knowledge of the unpolarized and polarized cross sections over the large phase space, including the DIS region, which is precisely what we are trying to extract. Thus, we cannot solve it analytically; instead, an iterative technique is employed. We define the radiative correction to the measured asymmetry by

$$\Delta A^{\mathrm{RC}} \equiv A^{\mathrm{Born}} - A^{\mathrm{meas}} . \tag{3.57}$$

A smooth parameterization to the measured $g_1^{\mathrm{He}}(x)/F_1^{\mathrm{He}}$ is used to calculate the initial estimate of A^{Born}, then at every i-th iteration we take $A_i^{\mathrm{Born}} = A_{i-1}^{\mathrm{Born}} + \Delta A_{i-1}^{\mathrm{RC}}$. The process typically converges after 3-4 iterations.

3.11.4 Radiative correction and experimental Errors

It is obvious from the discussions above, that the experimental uncertainties on ΔA^{RC} are correlated to those on A^{meas}. Not only is this true at every experimental point, but the convolutions in Eq. (3.56) also introduce point-to-point correlations. This makes the propagation of errors through the radiative corrections a rather complicated issue. We identify three types of experimental errors on A^{Born}:

- Statistical error $\sigma_{\mathrm{stat}}(A^{\mathrm{Born}})$: propagated statistical error on A^{meas};
- Systematic error $\sigma_{\mathrm{syst}}(A^{\mathrm{Born}})$: propagated systematic error on A^{meas} due to sources other than RC; and
- Errors on A^{tail} and unpolarized cross sections – true RC systematic error $\sigma_{\mathrm{RC}}(A^{\mathrm{Born}})$ – to be added in quadrature to other systematic errors.

The statistical errors on A^{meas} are uncorrelated from point to point, and we assume systematic errors to be 100% correlated from point to point. Then, for a given experimental point i, the propagated errors are given by

$$\sigma^2_{\mathrm{stat}}(A_i^{\mathrm{Born}}) = \sigma^2_{\mathrm{stat}}(A_i^{\mathrm{meas}}) \left(1 + \frac{\partial \Delta A_i^{\mathrm{RC}}}{\partial A_i^{\mathrm{meas}}}\right)^2 + \sum_{j \neq i} \sigma^2_{\mathrm{stat}}(A_j^{\mathrm{meas}}) \left(\frac{\partial \Delta A_i^{\mathrm{RC}}}{\partial A_j^{\mathrm{meas}}}\right)^2 \tag{3.58}$$

$$\sigma_{\rm syst}(A_i^{\rm Born}) = \sigma_{\rm syst}(A_i^{\rm meas})\left(1+\frac{\partial\Delta A_i^{\rm RC}}{\partial A_i^{\rm meas}}\right)+\sum_{j\neq i}\sigma_{\rm stat}(A_j^{\rm meas})\left(\frac{\partial\Delta A_i^{\rm RC}}{\partial A_j^{\rm meas}}\right). \quad (3.59)$$

In practice, the partial derivatives are evaluated numerically by varying the value of $A_i^{\rm meas}$ for every point independently within its statistical and systematic uncertainties. In order to include point-to-point correlations into the error on the integrals of g_1^n and g_2^n, the full correlation matrix is constructed. The off-diagonal elements of the correlation matrix are typically small.

In the absence of the off-diagonal elements, the uncertainty on the Born asymmetry is bigger than the error on the measured asymmetry by a factor

$$\frac{1}{f} = 1+\frac{\partial\Delta A_i^{\rm RC}}{\partial A_i^{\rm meas}}\,. \quad (3.60)$$

The factor f can be viewed as a "dilution factor" that accounts for the fact that the radiative tails are really backgrounds to our measurement. This dilution factor is given by the ratio of the unpolarized cross sections

$$f = \frac{\sigma^{\rm meas}-\sigma^{\rm tails}}{\sigma^{\rm meas}}\,, \quad (3.61)$$

where the "tails" include contributions from the elastic, quasi-elastic, resonance, and parts of the DIS tails. Due to the infra-red divergence,[136] the definition of the DIS tail is ambiguous.[139] We only include those points in x that are more than two bins away from the x of the measurement, beyond the range of a typical variation of g_1.[139] The "dilution factor" method of calculating the error on the Born asymmetry agrees with the method of Equations (3.58) and (3.59), and for practical purposes was adopted for the published results.

The systematic uncertainty on the radiative corrections is estimated by varying the input models of unpolarized and polarized cross sections (form factors for elastic and quasielastic scattering, nuclear corrections in ^{3}He unpolarized structure functions, models of the resonance region, contributions from g_2, and possible Q^2

Table 3.6. Systematic errors of the radiative corrections for the 2.75° and 5.5° spectrometers (× 100).

x bin	F_2	g_1 reson.	Q^2 dep.	g_2	$G_{e,m}^{p,n}$	Pauli	Elast
2.75° spectrometer							
0.017	0.018	0.025	0.031	0.019	0.017	0.006	0.004
0.025	0.049	0.022	0.011	0.015	0.007	0.004	0.003
0.035	0.030	0.020	0.003	0.010	0.003	0.002	0.002
0.049	0.010	0.018	0.000	0.007	0.001	0.001	0.001
0.078	0.006	0.015	0.000	0.004	0.000	0.000	0.000
0.123	0.013	0.014	0.000	0.002	0.000	0.000	0.000
0.173	0.001	0.015	0.000	0.003	0.000	0.000	0.000
0.241	0.000	0.018	0.000	0.003	0.000	0.000	0.000
0.340	0.001	0.026	0.000	0.005	0.000	0.000	0.000
0.423	0.000	0.045	0.000	0.007	0.000	0.000	0.000
5.5° spectrometer							
0.057	0.039	0.045	0.000	0.034	0.012	0.003	0.006
0.084	0.023	0.041	0.000	0.024	0.007	0.002	0.004
0.123	0.005	0.031	0.000	0.019	0.005	0.001	0.002
0.173	0.021	0.023	0.000	0.016	0.002	0.000	0.002
0.242	0.001	0.017	0.000	0.014	0.001	0.000	0.001
0.342	0.000	0.009	0.000	0.018	0.000	0.000	0.000
0.442	0.000	0.007	0.000	0.029	0.000	0.000	0.000
0.564	0.000	0.008	0.000	0.062	0.000	0.000	0.000

dependence[77] of the ratio g_1/F_1 below $Q^2 = 1$ GeV^2) and the target model (for external corrections). The contributions from the various sources for two spectrometers are given in Table 3.6.[139] The radiative corrections for $A_{||}$[140] and their errors[139] are given in Table 3.7.

Note that traditionally the "radiative dilution factor" was calculated assuming that only the elastic and quasi-elastic tails are backgrounds to the DIS measurement.[135] The uncertainty in the DIS asymmetries was included into the overall systematic error by varying the *shape* of the function used to parameterize the measured asymmetries.[140] This approach is inconsistent, subjective, and generally leads to incorrect results. First, the resonance and DIS tails have to be treated as

Table 3.7. Radiative corrections ($\times$ 100), the effect on the propagated errors, and the systematic errors of the radiative corrections.

x bin	ΔA^{RC}	$\sigma\left(A^{Born}\right)/\sigma\left(A^{meas}\right)$	Syst.
2.75° spectrometer			
0.017	-0.341	1.686	0.051
0.025	-0.285	1.500	0.057
0.035	-0.233	1.334	0.038
0.049	-0.192	1.216	0.022
0.078	-0.151	1.154	0.017
0.123	-0.122	1.113	0.019
0.173	-0.099	1.068	0.015
0.241	-0.081	1.049	0.018
0.340	-0.061	1.048	0.026
0.423	-0.051	1.102	0.046
5.5° spectrometer			
0.0573	-0.290	1.319	0.070
0.0837	-0.251	1.202	0.053
0.1231	-0.227	1.123	0.037
0.1725	-0.210	1.066	0.035
0.2420	-0.185	1.039	0.022
0.3424	-0.152	1.022	0.020
0.4423	-0.124	1.009	0.030
0.5643	-0.102	1.028	0.063

backgrounds and such events have to be subtracted from the data sample. Second, the variations of the functional form used to fit the measured data, deemed to test any possible "model dependence" of the radiative corrections, only change the relative weights of the data points. Many functional forms with acceptable χ^2 differ from one another by an amount comparable to the statistical errors of the data. This amount depends on the choice of the functional forms, and is very subjective. Varying the form of the fit is equivalent to varying the input values of the measured asymmetries by some fraction of their statistical errors. Thus, the variation of the Born asymmetries due to different fits used in the radiative corrections is already included into the statistical error $\sigma_{\mathrm{stat}}(A^{\mathrm{Born}})$. Including this variation into the systematic error $\sigma_{\mathrm{RC}}(A^{\mathrm{Born}})$ introduces unphysical correlations of the statistical and systematic errors, and in case of E154 increases the uncertainty $\sigma_{\mathrm{RC}}(A^{\mathrm{Born}})$ by about factor of two. The model dependence may appear, however, when the data are *extrapolated* outside the kinematic range of the measurement. Thus, the uncertainty due to extrapolation of the data into the low Q^2 region is included in the systematic error.

3.12 Rate dependence and electroweak corrections

The rate dependence to $A_{||}$ is calculated as described in Section 3.6. The detector asymmetries (electron asymmetry diluted by the pion and noise hits) were typically $(3-5)\cdot 10^{-4}$ in the Cherenkov detectors, $(1-4)\cdot 10^{-4}$ in the hodoscopes, and $(1-4)\cdot 10^{-3}$ in the shower counter. The rate dependence coefficients α_i determined by pulse fiction actually place the upper limit on the true rate dependence. The "true" rate dependence is proportional to the derivative of the efficiency with respect to rate. Pulse fiction measures the finite difference of efficiencies at normal and double rate. Since the second derivative of efficiency versus rate is normally negative (*i.e.* has the same sign as the first derivative), the coefficients α_i found by pulse fiction

are somewhat overestimated. So we treat the pulse fiction results as upper limits and apply only half of ΔA^{rate} as a correction to the raw asymmetries, and use the full value of ΔA^{rate} as a systematic error. This error ranges from 4% of $A_{||}$ at low x to 8% at high x.

The electroweak parity-violating asymmetry arises from the interference of the γ and Z^0 exchange amplitudes. It is given by[20]

$$A^{\text{EW}} \equiv \frac{\sigma_R - \sigma_L}{\sigma_R + \sigma_L} = Q^2 \left(a_1 + a_2 \frac{1-(1-y)^2}{1+(1-y)^2} \right) , \tag{3.62}$$

where σ_L and σ_R are cross sections for left and right electrons, and y is the fractional energy transfer from the electron to hadrons. For an isoscalar target, neglecting strange sea, one has

$$\begin{aligned} a_1 &\approx \frac{3G_F}{5\sqrt{2}\pi\alpha} \left(-\frac{3}{4} + \frac{5}{3}\sin^2\theta_W \right) \quad \text{and} \\ a_2 &\approx \frac{9G_F}{5\sqrt{2}\pi\alpha} \left(\sin^2\theta_W - \frac{1}{4} \right) . \end{aligned} \tag{3.63}$$

The factors in the equation are the Fermi constant G_F, the fine structure constant α, and the Weinberg angle θ_W. The electroweak asymmetry is not sensitive to the polarization of the target, and it is suppressed by the reversals of the target spin. The correction is the biggest at high Q^2 (and high x) and reaches 10% of $A_{||}$ (it is however much smaller than the statistical error on $A_{||}$). We use 20% of the correction as the associated systematic uncertainty.

3.13 Final asymmetry results

The corrected physics asymmetries A^{phys}, calculated for every run according to Eq. (3.46), were weighted by the statistical error and averaged. The results for two spectrometers are given in Table 3.8.

Table 3.8. Final results on ^{3}He asymmetries $A_{||}$ and $A_{\perp}$.

x bin	$\langle x \rangle$	$\langle Q^2 \rangle$ (GeV^2)	$A_{||} \pm$ stat. $\pm$ syst.	$A_{\perp} \pm$ stat. $\pm$ syst.
		2.75° spectrometer		
0.014 – 0.02	0.017	1.21	$-0.0140 \pm 0.0041 \pm 0.0036$	$0.0052 \pm 0.0125 \pm 0.0017$
0.02 – 0.03	0.025	1.59	$-0.0174 \pm 0.0030 \pm 0.0025$	$-0.0021 \pm 0.0094 \pm 0.0013$
0.03 – 0.04	0.035	2.05	$-0.0164 \pm 0.0031 \pm 0.0018$	$-0.0187 \pm 0.0100 \pm 0.0019$
0.04 – 0.06	0.049	2.57	$-0.0136 \pm 0.0025 \pm 0.0011$	$0.0142 \pm 0.0080 \pm 0.0015$
0.06 – 0.10	0.078	3.32	$-0.0107 \pm 0.0023 \pm 0.0009$	$0.0083 \pm 0.0075 \pm 0.0013$
0.10 – 0.15	0.122	4.09	$-0.0080 \pm 0.0027 \pm 0.0007$	$0.0101 \pm 0.0095 \pm 0.0022$
0.15 – 0.20	0.173	4.63	$-0.0102 \pm 0.0034 \pm 0.0008$	$0.0013 \pm 0.0123 \pm 0.0022$
0.20 – 0.30	0.241	5.09	$-0.0085 \pm 0.0034 \pm 0.0007$	$-0.0097 \pm 0.0121 \pm 0.0020$
0.30 – 0.40	0.340	5.51	$-0.0030 \pm 0.0058 \pm 0.0005$	$0.0357 \pm 0.0200 \pm 0.0038$
0.40 – 0.50	0.423	5.82	$0.0035 \pm 0.0137 \pm 0.0007$	$0.0043 \pm 0.0443 \pm 0.0008$
		5.5° spectrometer		
0.04 – 0.06	0.057	4.03	$0.0126 \pm 0.0256 \pm 0.0027$	$0.1669 \pm 0.1219 \pm 0.0151$
0.06 – 0.10	0.084	5.47	$-0.0222 \pm 0.0035 \pm 0.0022$	$0.0294 \pm 0.0163 \pm 0.0026$
0.10 – 0.15	0.123	7.23	$-0.0219 \pm 0.0026 \pm 0.0017$	$0.0052 \pm 0.0124 \pm 0.0025$
0.15 – 0.20	0.172	8.94	$-0.0153 \pm 0.0033 \pm 0.0012$	$0.0043 \pm 0.0154 \pm 0.0033$
0.20 – 0.30	0.242	10.71	$-0.0161 \pm 0.0033 \pm 0.0013$	$0.0137 \pm 0.0153 \pm 0.0034$
0.30 – 0.40	0.342	12.55	$-0.0089 \pm 0.0051 \pm 0.0018$	$-0.0106 \pm 0.0237 \pm 0.0022$
0.40 – 0.50	0.442	13.83	$-0.0132 \pm 0.0079 \pm 0.0013$	$-0.0092 \pm 0.0365 \pm 0.0015$
0.50 – 0.70	0.564	15.00	$-0.0010 \pm 0.0113 \pm 0.0008$	$-0.0036 \pm 0.0519 \pm 0.0035$

CHAPTER 4

NEUTRON SPIN STRUCTURE FUNCTIONS

4.1 From asymmetries to the structure functions

4.1.1 Structure functions and photon-nucleon asymmetries

The fully-corrected asymmetries in Table 3.8 are ready to be used to calculate the quantities of interest: the spin dependent structure functions and the virtual photon-nucleon asymmetries. At this time it is also logical to compare the results of two independent analyses. While the raw asymmetries could have been somewhat different in the SLAC and Caltech analyses (due to different contamination and corrections), the final asymmetries $A_{||}$ and $A_{\perp}$ must be identical within allowed statistical fluctuations, if both analyses are correct. For completeness, we will here list the main differences between two analyses:

- *Raw analysis*

  The DST production had started earlier at SLAC, and certain ideas were not implemented. The most important one was the FADC synchronization using the TDC information (see Section 3.3). The shower code described in Section 3.4 was used only in the Caltech analysis; the SLAC code is described in Ref. [116]. The tracking used by both analyses is described in Section 3.5 with very minor improvements not implemented in the SLAC version. The Caltech analysis stored only class 1 tracks on the DST tapes while at SLAC tracks of classes 1, 2, and 3 were kept (only class 1 tracks were used as electron candidates).

- *Run selection*

  Both analyses used the same set of runs, as described in Section 3.7.2.

- *DST analysis*

  Both codes were very similar at the level of the DST analysis. The main difference was in the beam cut, which was very generous for the SLAC analysis[141] and somewhat more restrictive at Caltech (see Section 3.7.3.1).

- *Electron selection*

  The two analyses differed in the definition of electrons (*cf.* Section 3.7.3.2). For completeness, we list below the definition adopted by the SLAC group:[141]

  1. Class 1 track with both Cherenkovs in coincidence;
  2. Acceptance cut passed;
  3. 8 GeV$< p <$ 48.3 GeV;
  4. 1 GeV$^2 \leq Q^2 \leq$ 25 GeV^2, $W^2 \geq$ 8 GeV^2;
  5. Peak voltage in both Cherenkov tanks $\geq$ 25 (in FADC units);
  6. $0.8 \leq E/p \leq 1.2$;
  7. Neural Network ≥ -0.98.[121]

- *Background subtraction and corrections to the raw asymmetries*

  The estimates of the pion contamination were quite different in the two analyses (*cf.* Section 3.9.1.1). The SLAC group estimated a less than 1% pion contamination using an indirect technique of scaling the π^+/e^+ ratio by the ratio of the π^-/π^+ production cross sections and the measured e^+/e^- rates[142] (a more sophisticated method, similar to the one described in Section 3.9.1.1, has been applied to the SLAC analysis data[143] and gives bigger estimates of the pion contamination, consistent with our analysis). The pion contamination was only measured for runs with the target cell Picard (the only time interval when the polarized "positron" runs were taken), and the SLAC group assumed that the contamination was constant with time. Fortunately, the pion contamination

was at most $5 - 10\%$ for the highest rate runs (see Section 3.9.1.1), so the error associated with such an assumption is not big. The background from the charge-symmetric processes was independent of the analysis cuts, and estimates of the background rates by both groups agree. The rate dependence correction was only applied to the Caltech data and was neglected by the SLAC group.

The comparison between the two sets of asymmetries is shown in Fig. 4.1. The agreement is as good as it could be, since the majority of the selected events is common. The differences between the two results are consistent with statistical fluctuations if $\approx 10 - 15\%$ of the events in the two samples are different. For the publications, we have chosen to average two results (straight average), and we have taken the larger statistical error. The averaged asymmetries are given in Table 4.1.

The averaged asymmetries $A_{||}$ and $A_{\perp}$ were used to calculate the spin dependent structure functions g_1^n and g_2^n and the photon-nucleon asymmetries A_1^n and A_2^n. Since the experimental asymmetries are given for ^{3}He, we first calculate $A_{||}$ and $A_{\perp}$ for the neutron (*cf.* Eq. (1.89)):

$$A_{||}^n = \frac{1}{p_n F_2^n} \left(A_{||}^{^3\mathrm{He}} (2F_2^p + F_2^n) f_{\mathrm{EMC}} - 2A_{||}^p p_p F_2^p \right) , \tag{4.1}$$

where $p_{n(p)}$ is the neutron (proton) polarization in ^{3}He (see Section 1.6), f_{EMC} is the EMC effect factor,[74] and $F_2^{n(p)}$ is the unpolarized structure function of the neutron (proton) (we assume that the ratio of the longitudinal to transverse cross sections $R(x, Q^2)$ is the same for proton and neutron[79]). We use the fit to the world data on g_1^p[10,12] to calculate the proton asymmetry $A_{||}^p$. The contribution of g_2^p is calculated using the Wandzura-Wilczek[36] twist-2 expression (see Eq. (1.47)) and the fit to g_1^p mentioned above. The expression for $A_{\perp}^n$ is similar to Eq. (4.1).

We use Equations (1.23) and (1.24) to calculate the spin dependent structure functions g_1^n and g_2^n of the neutron. The neutron virtual asymmetries A_1^n and A_2^n are given by Equations (1.25) and (1.26). The structure functions and the photon-

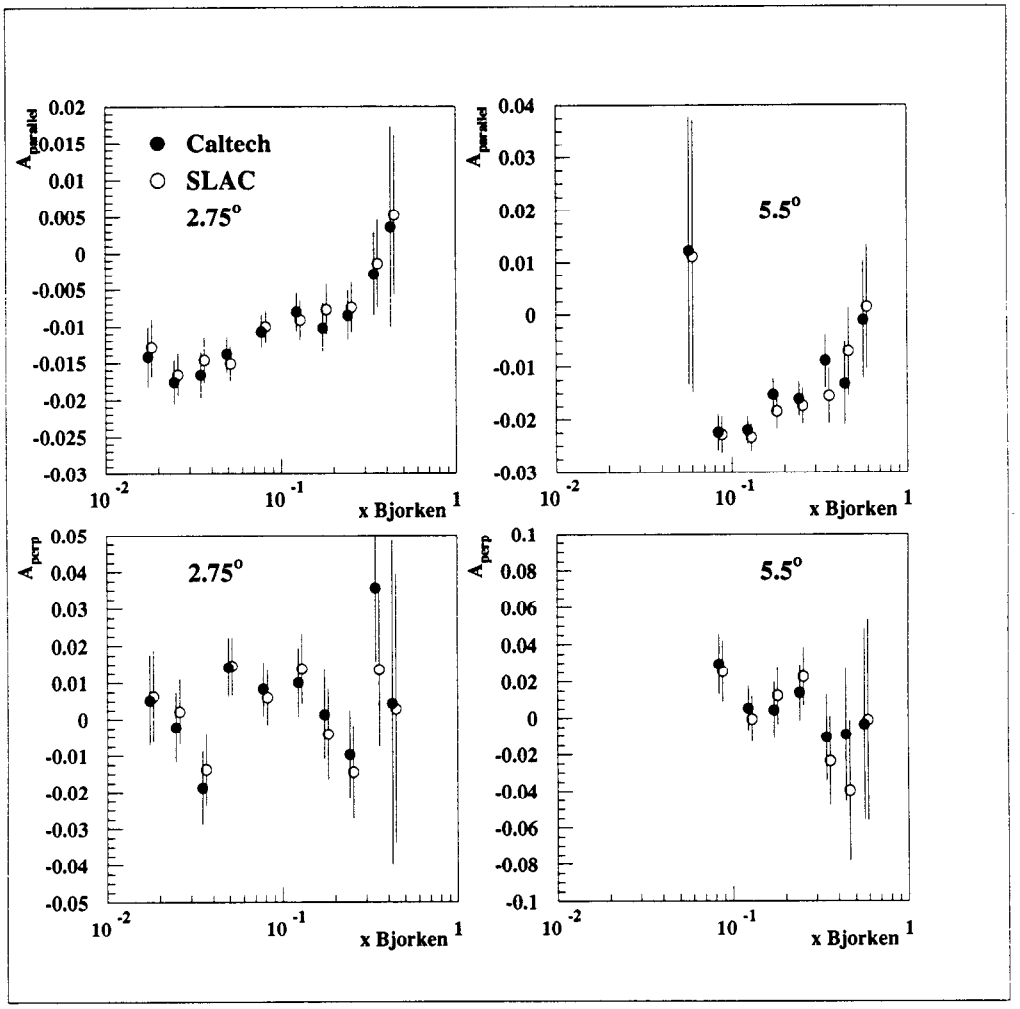

Fig. 4.1. The comparison between asymmetries $A_{\parallel}$ (top) and $A_{\perp}$ (bottom) given by the SLAC (open circles) and Caltech (closed circles) analyses.

Table 4.1. Averaged results of the two analyses on ^{3}He asymmetries $A_{\parallel}$ and $A_{\perp}$.

x bin	$\langle x \rangle$	$\langle Q^2 \rangle$ (GeV^2)	$A_{\parallel} \pm$ stat. $\pm$ syst.	$A_{\perp} \pm$ stat. $\pm$ syst.
		2.75° spectrometer		
0.014 – 0.02	0.017	1.21	$-0.0133 \pm 0.0041 \pm 0.0036$	$0.0058 \pm 0.0126 \pm 0.0018$
0.02 – 0.03	0.025	1.59	$-0.0169 \pm 0.0030 \pm 0.0025$	$0.0000 \pm 0.0094 \pm 0.0013$
0.03 – 0.04	0.035	2.05	$-0.0154 \pm 0.0031 \pm 0.0018$	$-0.0163 \pm 0.0100 \pm 0.0018$
0.04 – 0.06	0.049	2.57	$-0.0143 \pm 0.0025 \pm 0.0012$	$0.0144 \pm 0.0080 \pm 0.0015$
0.06 – 0.10	0.078	3.32	$-0.0103 \pm 0.0023 \pm 0.0009$	$0.0072 \pm 0.0075 \pm 0.0013$
0.10 – 0.15	0.122	4.09	$-0.0085 \pm 0.0027 \pm 0.0007$	$0.0120 \pm 0.0095 \pm 0.0022$
0.15 – 0.20	0.173	4.63	$-0.0089 \pm 0.0034 \pm 0.0008$	$-0.0014 \pm 0.0125 \pm 0.0022$
0.20 – 0.30	0.241	5.09	$-0.0080 \pm 0.0034 \pm 0.0007$	$-0.0121 \pm 0.0127 \pm 0.0021$
0.30 – 0.40	0.340	5.51	$-0.0022 \pm 0.0060 \pm 0.0005$	$0.0247 \pm 0.0210 \pm 0.0035$
0.40 – 0.50	0.423	5.82	$0.0044 \pm 0.0137 \pm 0.0007$	$0.0036 \pm 0.0443 \pm 0.0007$
		5.5° spectrometer		
0.04 – 0.06	0.057	4.03	$0.0120 \pm 0.0260 \pm 0.0027$	$0.1582 \pm 0.1219 \pm 0.0146$
0.06 – 0.10	0.084	5.47	$-0.0224 \pm 0.0035 \pm 0.0022$	$0.0274 \pm 0.0165 \pm 0.0025$
0.10 – 0.15	0.123	7.23	$-0.0226 \pm 0.0027 \pm 0.0018$	$0.0023 \pm 0.0126 \pm 0.0025$
0.15 – 0.20	0.172	8.94	$-0.0168 \pm 0.0034 \pm 0.0013$	$0.0082 \pm 0.0157 \pm 0.0033$
0.20 – 0.30	0.242	10.71	$-0.0168 \pm 0.0034 \pm 0.0013$	$0.0182 \pm 0.0158 \pm 0.0035$
0.30 – 0.40	0.342	12.55	$-0.0123 \pm 0.0053 \pm 0.0019$	$-0.0171 \pm 0.0246 \pm 0.0024$
0.40 – 0.50	0.442	13.83	$-0.0102 \pm 0.0084 \pm 0.0012$	$-0.0245 \pm 0.0383 \pm 0.0020$
0.50 – 0.70	0.564	15.00	$0.0003 \pm 0.0119 \pm 0.0008$	$-0.0024 \pm 0.0548 \pm 0.0034$

Table 4.2. The spin dependent structure function g_1^n and the photon-nucleon asymmetry A_1^n.

$\langle x \rangle$	$\langle Q^2 \rangle$ (GeV^2)	$g_1^n \pm$ stat. $\pm$ syst.	$A_1^n \pm$ stat. $\pm$ syst.
		2.75° spectrometer	
0.017	1.21	$-0.351 \pm 0.115 \pm 0.104$	$-0.058 \pm 0.019 \pm 0.017$
0.024	1.59	$-0.374 \pm 0.071 \pm 0.062$	$-0.080 \pm 0.015 \pm 0.014$
0.035	2.05	$-0.290 \pm 0.061 \pm 0.037$	$-0.078 \pm 0.018 \pm 0.011$
0.049	2.57	$-0.212 \pm 0.041 \pm 0.021$	$-0.089 \pm 0.016 \pm 0.010$
0.078	3.32	$-0.119 \pm 0.031 \pm 0.013$	$-0.078 \pm 0.019 \pm 0.009$
0.123	4.09	$-0.075 \pm 0.030 \pm 0.009$	$-0.089 \pm 0.031 \pm 0.011$
0.173	4.63	$-0.070 \pm 0.033 \pm 0.009$	$-0.100 \pm 0.053 \pm 0.014$
0.241	5.09	$-0.053 \pm 0.028 \pm 0.007$	$-0.078 \pm 0.077 \pm 0.018$
0.340	5.51	$0.001 \pm 0.036 \pm 0.004$	$-0.166 \pm 0.206 \pm 0.051$
0.423	5.82	$0.027 \pm 0.059 \pm 0.007$	$0.166 \pm 0.606 \pm 0.038$
		5.5° spectrometer	
0.057	4.03	$0.224 \pm 0.285 \pm 0.035$	$0.045 \pm 0.120 \pm 0.012$
0.084	5.47	$-0.152 \pm 0.029 \pm 0.019$	$-0.104 \pm 0.018 \pm 0.013$
0.123	7.23	$-0.117 \pm 0.017 \pm 0.012$	$-0.110 \pm 0.015 \pm 0.012$
0.172	8.94	$-0.059 \pm 0.016 \pm 0.007$	$-0.090 \pm 0.023 \pm 0.011$
0.242	10.71	$-0.040 \pm 0.012 \pm 0.005$	$-0.118 \pm 0.030 \pm 0.016$
0.342	12.55	$-0.019 \pm 0.012 \pm 0.005$	$-0.057 \pm 0.068 \pm 0.022$
0.442	13.83	$-0.009 \pm 0.012 \pm 0.002$	$-0.013 \pm 0.146 \pm 0.018$
0.564	15.00	$0.003 \pm 0.008 \pm 0.001$	$0.100 \pm 0.294 \pm 0.032$

nucleon asymmetries are given for the two spectrometers in Table 4.2 and Table 4.3. The structure function xg_1^n is plotted in Fig. 4.2, and xg_2^n is shown in Fig. 4.3.

4.1.2 Traditional Q^2 evolution

Since the QCD sum rules are defined at a fixed four-momentum transfer, one needs to evolve the data from the Q^2 of the measurement (which is given along the line $Q^2 = Q^2(x)$, see Fig. 2.10) to a constant value, usually taken to be the average Q^2. The average Q^2 for E154 (weighted by statistics of $A_{||}$) is ≈ 5 GeV^2. Traditionally, experiments have been using the fact that the data, albeit of the limited precision to be conclusive, are consistent with the assumption that for $Q^2 >$ 1 GeV^2 the ratio of the polarized to the unpolarized structure functions g_1/F_1, or

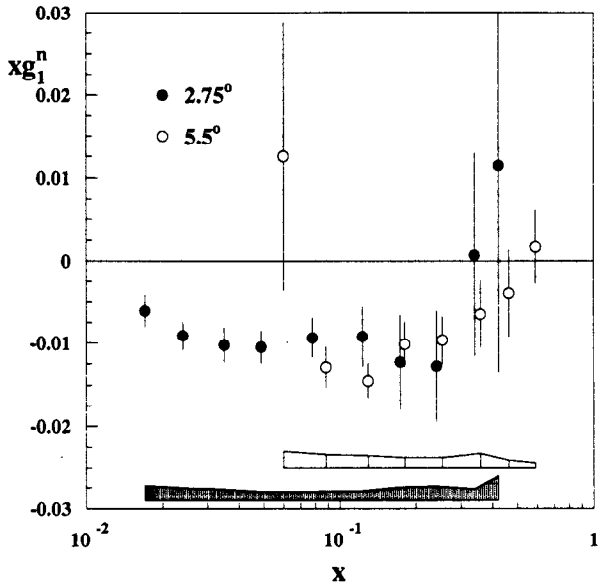

Fig. 4.2. The structure function xg_1^n measured in the 2.75° (closed circles) and 5.5° (open circles) spectrometers. The 5.5° data points are slightly offset in x for clarity. The shaded area represents one standard deviation systematic errors.

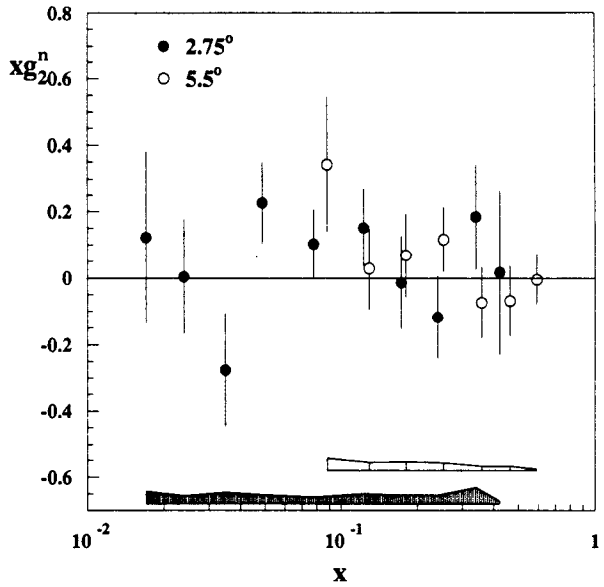

Fig. 4.3. The structure function xg_2^n measured in the 2.75° and 5.5° spectrometers. The shaded area represents one standard deviation systematic errors.

Table 4.3. The spin dependent structure function g_2^n and the photon-nucleon asymmetry A_2^n.

$\langle x \rangle$	$\langle Q^2 \rangle$ (GeV^2)	$g_2^n \pm$ stat. $\pm$ syst.	$A_2^n \pm$ stat. $\pm$ syst.
		2.75° spectrometer	
0.017	1.21	$7.167 \pm 15.312 \pm 2.169$	$0.033 \pm 0.074 \pm 0.010$
0.024	1.59	$0.154 \pm 7.232 \pm 0.980$	$-0.002 \pm 0.056 \pm 0.007$
0.035	2.05	$-7.870 \pm 4.890 \pm 0.958$	$-0.106 \pm 0.064 \pm 0.013$
0.049	2.57	$4.605 \pm 2.504 \pm 0.543$	$0.099 \pm 0.056 \pm 0.012$
0.078	3.32	$1.318 \pm 1.331 \pm 0.245$	$0.058 \pm 0.065 \pm 0.012$
0.123	4.09	$1.223 \pm 0.953 \pm 0.237$	$0.127 \pm 0.106 \pm 0.026$
0.173	4.63	$-0.080 \pm 0.810 \pm 0.145$	$-0.033 \pm 0.179 \pm 0.033$
0.241	5.09	$-0.486 \pm 0.515 \pm 0.105$	$-0.251 \pm 0.241 \pm 0.049$
0.340	5.51	$0.541 \pm 0.466 \pm 0.145$	$0.635 \pm 0.550 \pm 0.126$
0.423	5.82	$0.040 \pm 0.580 \pm 0.018$	$0.162 \pm 1.414 \pm 0.040$
		5.5° spectrometer	
0.057	4.03	$41.007 \pm 31.640 \pm 4.458$	$0.945 \pm 0.727 \pm 0.103$
0.084	5.47	$4.077 \pm 2.403 \pm 0.434$	$0.161 \pm 0.099 \pm 0.018$
0.123	7.23	$0.231 \pm 1.003 \pm 0.196$	$0.009 \pm 0.080 \pm 0.016$
0.172	8.94	$0.398 \pm 0.723 \pm 0.153$	$0.052 \pm 0.112 \pm 0.024$
0.242	10.71	$0.477 \pm 0.407 \pm 0.098$	$0.145 \pm 0.136 \pm 0.031$
0.342	12.55	$-0.216 \pm 0.311 \pm 0.039$	$-0.205 \pm 0.273 \pm 0.032$
0.442	13.83	$-0.155 \pm 0.239 \pm 0.030$	$-0.360 \pm 0.532 \pm 0.047$
0.564	15.00	$-0.008 \pm 0.132 \pm 0.009$	$-0.036 \pm 0.953 \pm 0.058$

the virtual photon-nucleon asymmetry A_1 are independent of Q^2 *for any given value of* x.[77] Although the assumption contradicts a perturbative QCD analysis (as will be discussed in Chapter 5), it could be a reasonable approximation if the range of Q^2 is not very big and/or if the error due to the approximation is significantly smaller than the uncertainty on the data. We will follow the traditional approach and evolve the data to $Q^2 = 5$ GeV^2 assuming the scaling (Q^2-independence) of g_1^n/F_1^n. We will carry out the Next-to-Leading order perturbative QCD analysis of the polarized DIS data in the next chapter and return to the question of Q^2 evolution.

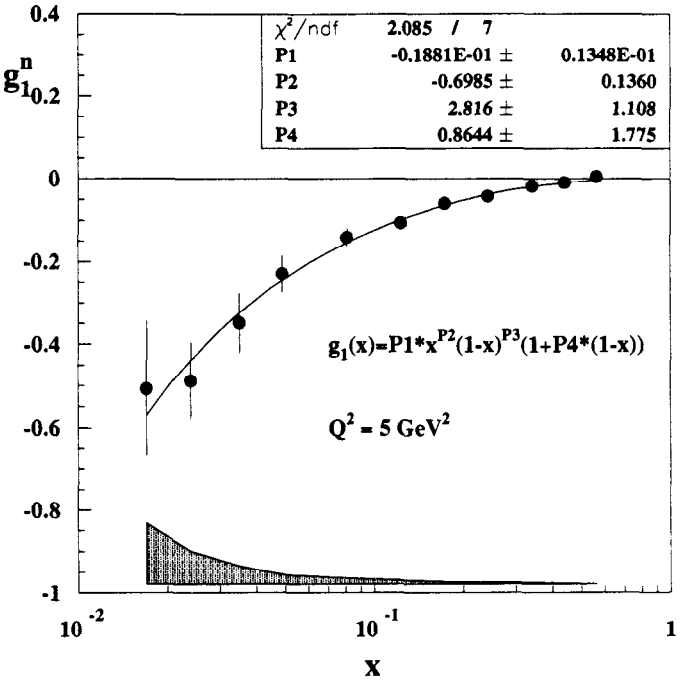

Fig. 4.4. The structure function g_1^n evaluated at $Q^2 = 5$ GeV^2. Overlaid is a fit to the data. The shaded area represents one standard deviation systematic errors.

4.1.3 Combining data from two spectrometers

The structure function g_1^n was evolved to the average $Q^2 = 5$ GeV^2 assuming the scaling of g_1^n/F_1^n, and the values of g_1 from the two spectrometers were averaged at $Q^2 = 5$ GeV^2 in the common x bins (weighted by the statistical error of g_1^n at 5 GeV^2). The average Bjorken $\langle x \rangle$ and $\langle Q^2 \rangle$ for each bin were also weighted by the statistical error of g_1^n. The average values for the structure function g_1^n and the asymmetry A_1^n are given in Table 4.4. The structure function g_1^n, evaluated at 5 GeV^2, is shown in Fig. 4.4.

4.2 Systematic errors

Many of the systematic uncertainties that affected the determination of the structure functions were mentioned in the previous sections. The contributions from

Table 4.4. Results on A_1^n and g_1^n at the measured Q^2, along with g_1^n evaluated at $Q^2 = 5$ (GeV)^2 assuming that the ratio g_1^n/F_1^n scales with Q^2. The data of two spectrometers have been averaged.

x bin	$\langle x \rangle$	$\langle Q^2 \rangle$ GeV^2	$g_1^n \pm$ stat. $\pm$ syst.	$A_1^n \pm$ stat. $\pm$ syst.	$g_1^n \pm$ stat. $\pm$ syst. ($Q^2 = 5$ GeV^2)
0.014 – 0.02	0.017	1.2	$-0.351 \pm 0.115 \pm 0.104$	$-0.058 \pm 0.019 \pm 0.017$	$-0.497 \pm 0.163 \pm 0.148$
0.02 – 0.03	0.024	1.6	$-0.374 \pm 0.071 \pm 0.063$	$-0.080 \pm 0.015 \pm 0.014$	$-0.481 \pm 0.092 \pm 0.081$
0.03 – 0.04	0.035	2.0	$-0.290 \pm 0.061 \pm 0.039$	$-0.078 \pm 0.018 \pm 0.011$	$-0.345 \pm 0.073 \pm 0.046$
0.04 – 0.06	0.049	2.6	$-0.204 \pm 0.040 \pm 0.022$	$-0.086 \pm 0.016 \pm 0.010$	$-0.228 \pm 0.045 \pm 0.024$
0.06 – 0.10	0.081	4.4	$-0.137 \pm 0.021 \pm 0.016$	$-0.092 \pm 0.013 \pm 0.011$	$-0.139 \pm 0.022 \pm 0.016$
0.10 – 0.15	0.123	6.6	$-0.108 \pm 0.015 \pm 0.011$	$-0.106 \pm 0.014 \pm 0.012$	$-0.105 \pm 0.014 \pm 0.011$
0.15 – 0.20	0.173	8.2	$-0.061 \pm 0.014 \pm 0.007$	$-0.092 \pm 0.021 \pm 0.011$	$-0.060 \pm 0.014 \pm 0.007$
0.20 – 0.30	0.242	9.8	$-0.042 \pm 0.011 \pm 0.005$	$-0.112 \pm 0.028 \pm 0.016$	$-0.043 \pm 0.011 \pm 0.005$
0.30 – 0.40	0.342	11.7	$-0.017 \pm 0.011 \pm 0.004$	$-0.068 \pm 0.065 \pm 0.021$	$-0.018 \pm 0.013 \pm 0.005$
0.40 – 0.50	0.441	13.3	$-0.007 \pm 0.011 \pm 0.002$	$-0.003 \pm 0.142 \pm 0.017$	$-0.009 \pm 0.014 \pm 0.002$
0.50 – 0.70	0.564	15.0	$0.003 \pm 0.008 \pm 0.001$	$0.100 \pm 0.294 \pm 0.032$	$0.005 \pm 0.012 \pm 0.001$

the various sources to the systematic error on $g_1^n(x)$ and on the integral in the measured range are summarized in Table 4.5.

The biggest contributions to the error on the integral in the measured range come from the scale uncertainties: dilution factor (relative error is approximately independent of x) and the target polarization. The biggest uncertainty at the lowest $x = 0.017$ is due to the asymmetry in the charge-symmetric processes. This error could potentially be reduced if some theoretical guidance (regarding the kinematic dependence of the asymmetry or its relation to the well measured pion asymmetry) was available (see Section 3.9.2).

4.3 Discussion of the results

The E154 data on g_1^n give the most precise determination of the spin-dependent structure function of the neutron to date. Our results are compared with the data from the previous SLAC experiments E142[9] and E143[10,11] in Fig. 4.5. The agreement among the data sets is very good. The E154 data extends the measurement of g_1^n to lower values of x and improves the precision by about factor of 2. Our results are compared to the data of the SMC experiment at CERN[12,13] in Fig. 4.6. The two data sets are complementary at low x since the SMC data extends to $x \approx 0.003$, albeit with large uncertainties.

The most striking feature of the E154 data is the behavior of the structure function at low x. Not only does it not converge to zero as x becomes smaller, but the behavior is very divergent (see Fig. 4.4). This is even more evident if the data are plotted on a log-log scale (Fig. 4.7). The data below $x = 0.1$ can be accurately fitted with a $g_1^n \sim x^{-0.8}$ power law. The low x power of the global fit (see Fig. 4.4) is -0.7 ± 0.1, or several standard deviations away from the naive Regge expectation[1]

[1]To actually estimate the statistical significance of the results one needs to take into account the correlations between the parameters of the fit. We will return to this question in Section 4.4.3.

Table 4.5. Contributions to the systematic error on g_1^n for every x bin and on the integral over the measured range.

Contribution	$\langle x \rangle$											Integral
	0.017	0.024	0.035	0.049	0.081	0.123	0.173	0.242	0.342	0.441	0.564	
P_b	0.0177	0.0171	0.0113	0.0070	0.0044	0.0033	0.0019	0.0014	0.0007	0.0004	0.0000	0.0012
P_t	0.0328	0.0316	0.0209	0.0130	0.0081	0.0061	0.0036	0.0026	0.0013	0.0007	0.0001	0.0023
f	0.0436	0.0291	0.0173	0.0094	0.0077	0.0054	0.0037	0.0029	0.0011	0.0017	0.0004	0.0024
F_2	0.0088	0.0074	0.0051	0.0039	0.0022	0.0018	0.0010	0.0008	0.0004	0.0003	0.0002	0.0007
R	0.0196	0.0182	0.0131	0.0070	0.0030	0.0017	0.0006	0.0002	0.0000	0.0000	0.0001	0.0008
E'	0.0105	0.0100	0.0071	0.0047	0.0032	0.0026	0.0019	0.0019	0.0009	0.0005	0.0009	0.0008
p_n	0.0116	0.0112	0.0080	0.0053	0.0032	0.0024	0.0014	0.0010	0.0004	0.0002	0.0001	0.0008
p_p	0.0041	0.0038	0.0035	0.0032	0.0028	0.0026	0.0024	0.0021	0.0016	0.0012	0.0007	0.0011
g_1^p	0.0282	0.0221	0.0078	0.0047	0.0027	0.0015	0.0015	0.0010	0.0005	0.0004	0.0004	0.0004
RC	0.0189	0.0163	0.0083	0.0046	0.0034	0.0028	0.0022	0.0004	0.0004	0.0006	0.0005	0.0011
Rate	0.0376	0.0261	0.0153	0.0084	0.0032	0.0015	0.0011	0.0007	0.0006	0.0002	0.0001	0.0012
A_π	0.0049	0.0031	0.0014	0.0008	0.0004	0.0002	0.0001	0.0000	0.0000	0.0000	0.0000	0.0001
π/e	0.0056	0.0067	0.0031	0.0011	0.0008	0.0004	0.0001	0.0000	0.0000	0.0000	0.0000	0.0002
A_{e^+}	0.1208	0.0469	0.0231	0.0063	0.0066	0.0021	0.0008	0.0007	0.0037	0.0000	0.0000	0.0011
e^+/e^-	0.0238	0.0098	0.0024	0.0005	0.0004	0.0001	0.0000	0.0000	0.0000	0.0000	0.0000	0.0003
EW	0.0010	0.0008	0.0006	0.0006	0.0006	0.0005	0.0005	0.0004	0.0003	0.0003	0.0002	0.0002
Total	0.1476	0.0809	0.0459	0.0242	0.0162	0.0110	0.0072	0.0054	0.0047	0.0025	0.0014	0.0045

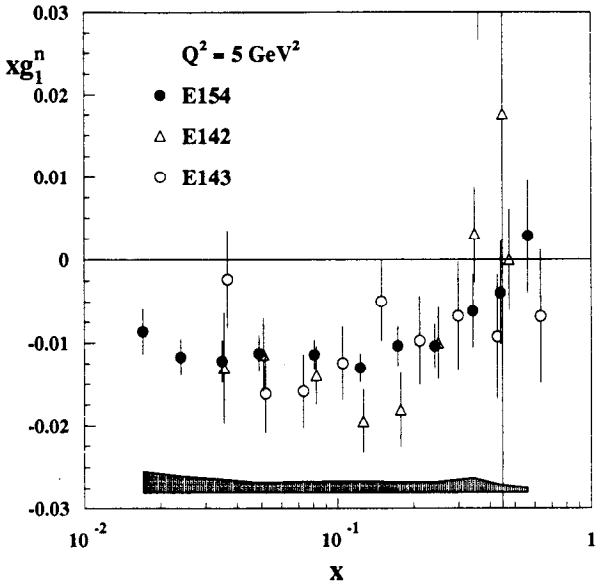

Fig. 4.5. The E154 results on the structure function xg_1^n (closed circles) compared to the E142 (open triangles) and E143 (open circles) data. The E142 and E143 data points are slightly offset in x for clarity. The shaded area represents one sigma systematic errors of E154.

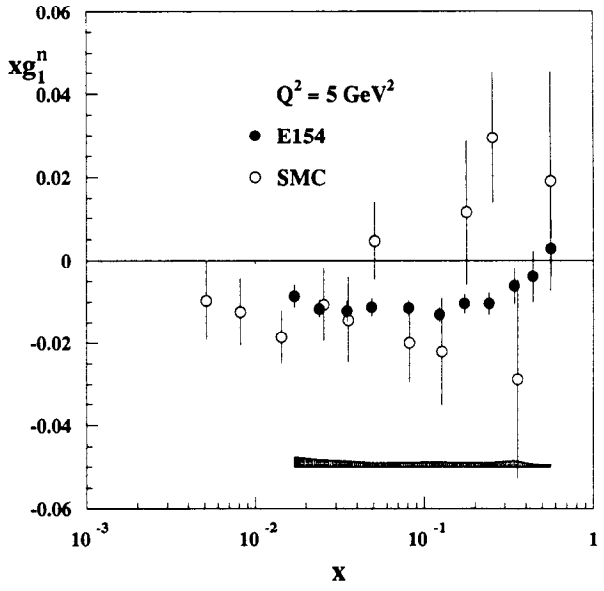

Fig. 4.6. A comparison of the E154 (closed circles) and SMC (open circles) data. The shaded are represents one standard deviation systematic errors.

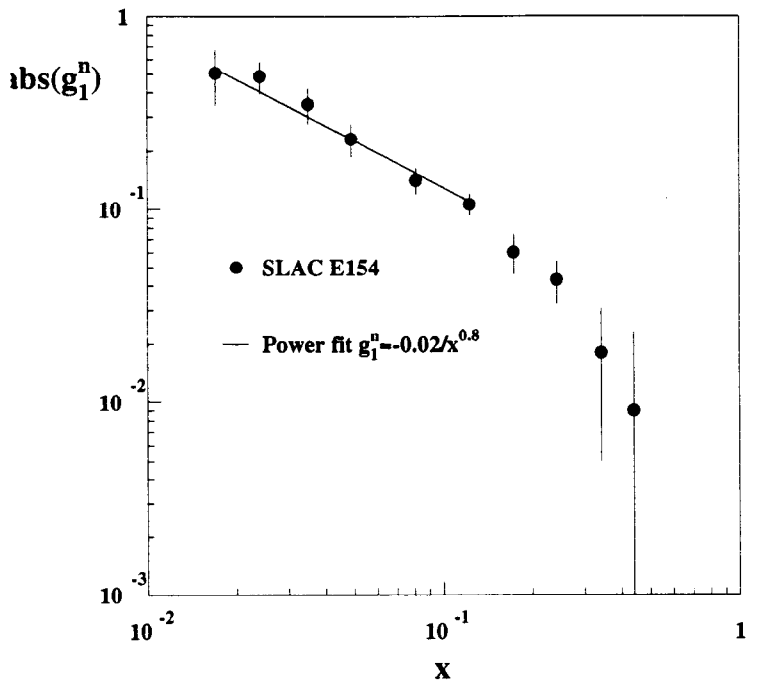

Fig. 4.7. The absolute value of structure function g_1^n is plotted on a log-log scale. The low x data points of E154 are fitted with a power-law function $g_1 \sim x^{-0.8}$.

$\alpha = 0$. Such a divergent behavior makes the extrapolation to $x = 0$ problematic, as will be discussed in the following Section.

4.4 Integrals

4.4.1 Data range

The integral of g_1^n in the data range was obtained by summing the values of the structure function in every bin multiplied by the width of the bin. The statistical errors are uncorrelated from bin to bin, and are added in quadrature. Most of the systematic errors are largely correlated bin-to-bin and therefore are added linearly. The uncorrelated errors (errors on positron asymmetry, pion asymmetry, and g_1^p) are added in quadrature. The final result for the integral in the data range is

$$\int_{0.0135}^{0.7} dx\ g_1^n(x) = -0.0360 \pm 0.0039 \pm 0.0045\ , \tag{4.2}$$

where the first uncertainty is statistical, and the second is systematic.

4.4.2 High x extrapolation

The kinematic range of any experiment is limited, and the data need to be extrapolated to $x = 0$ and $x = 1$ in order to compute the full integral of g_1 and test the sum rules. The extrapolation to $x = 1$ is straightforward. The quark-counting rules predict (see Section 1.4.1) the leading twist contribution of the structure function to fall off as $g_1 \sim (1-x)^3$ (or even faster due to the Q^2 evolution) as $x \to 1$. The higher-twist contributions may have a slower dependence (see Section 1.3.2.2), but it is the leading twist contribution that we are interested in. We assume the $(1-x)^3$ dependence of g_1^n at high x and use the value of g_1^n in the last bin to set the scale. The contribution to the integral from the unmeasured high x region is then

$$\int_{0.7}^{1} dx\ g_1^n(x) = (0.15 \pm 0.42 \pm 0.04) \cdot 10^{-3}\ , \tag{4.3}$$

where the first uncertainty is statistical, and the second is systematic.

4.4.3 Low x extrapolation

A much more important contribution comes from the unmeasured low-x region. While the high-x extrapolation is well justified theoretically and the contribution to the integral is negligible, the extrapolation to $x = 0$ is much less certain. As was discussed in Section 1.5, the theoretical models vary widely in this region. The traditional approach, taken by all spin structure experiments prior to E154, was to assume the convergent Regge behavior $g_1 \sim x^{-\alpha}$ where the Regge intercept α is associated with the trajectory of the a_1 meson and is bound between -0.5 and 0.[65,66] This assumption was consistent with the E142 neutron data,[9] and the E143 proton[10] and deuteron[11] data (which was limited to $x > 0.03$), but just barely agreed with the high energy SMC proton data.[12] The Regge theory does not explicitly specify the kinematic domain in which the prediction of the asymptotic behavior is applicable (see Section 1.5). The approach adopted by the experimental

collaborations[9–11] was to fit the data with the Regge-type function $g_1 \sim x^{-\alpha}$, $\alpha < 0$ below $x = 0.1$ (that corresponds to $\sqrt{s} > 6$ GeV cutoff at $Q^2 \approx 5$ GeV^2, and the total γp cross sections are successfully described in that kinematic range by Regge theory[64]). This function does not apparently fit the E154 neutron data. Fitting the g_1^n data with a $g_1^n = const$ form (*i.e.* saturating the upper limit on the a_1 intercept) results in a $\chi^2 = 24$ for 4 degrees of freedom (where only uncorrelated errors are taken into account). This χ^2 corresponds to the confidence level of $0.8 \cdot 10^{-4}$; inclusion of the point-to-point correlated errors increases the confidence level to $0.4 \cdot 10^{-3}$. However, one may still fit the three lowest x points ($x < 0.04$) to a constant with a reasonable $\chi^2 = 1.7$ for 2 degrees of freedom. Since the Regge prediction is not very specific, we may not *a priori* discard the possibility that the convergent behavior sets in at this, or even lower value of x.

Lacking a satisfactory description of the low x data by a conventional theory, we shall resort to other phenomenological fits to the data. Several possible functional forms have been discussed in Section 1.5. To illustrate the possible spread among models divergent at low x, we fit the data to the Pomeron-Pomeron cut form[67,68] $g_1^n \sim 1/(x \ln^2 x)$, and to the generic power law $g_1^n \sim x^{-\alpha}$ with α being a free parameter. The Pomeron-Pomeron form fits reasonably well the four lowest x points ($x \leq 0.06$). To fit the power-law form we use the five lowest x points ($x \leq 0.1$). In addition, a "global" parameterization of the form

$$g_1^n = Cx^{-\alpha}(1-x)^{\beta} \tag{4.4}$$

that does not require a low-x cutoff, could be used to extrapolate the data to $x = 0$. All eleven data points are used to obtain the parameters of the "global" fit (Fig. 4.4). The results of the fits are listed in Table 4.6 together with the integral from the unmeasured low x region and the resulting integral over the full x range[2]. Three

[2]For the multi-parameter fits, the parameter correlation matrix was used to calculate the error on the integrals.

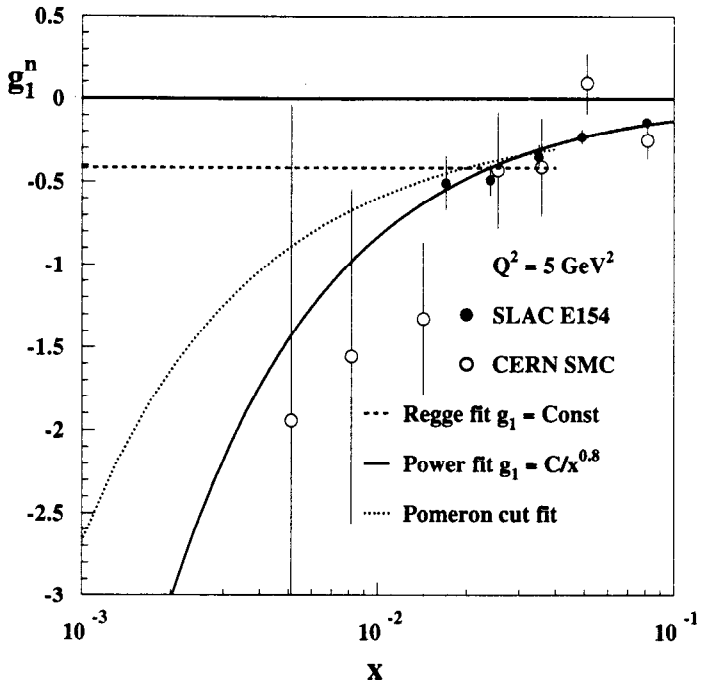

Fig. 4.8. Three representative fits to the low x data of E154. Also included are the low-x data of SMC (open circles).

representative fits are shown in Fig. 4.8 for which the low-x power was fixed at 0.8, the average of the "global" and free power fit.

The spread of the possible contributions from the low x region is very big even for moderately convergent models. Note that the free-power fit gives a value of the exponent α that is very close to unity, in fact, $\alpha > 1$ is consistent with the data within statistical or systematic errors. Since the integral diverges if $\alpha > 1$, we do not quote any uncertainty; the integral is simply *less than 1 standard deviation from infinity.* This is not very satisfactory; clearly, precise high energy data are needed to determine the behavior of the structure functions at low x.

4.5 Sum rules

Given the spread of the models at low x, we feel that the evaluation of the Ellis-Jaffe sum rule is not possible at present. Relatively large values of the neutron

Table 4.6. Results of the fits to the low x data of E154. The first uncertainty is statistical and the second is systematic.

Fit	points	Parameters	$\int_0^{0.0135} dx\ g_1^n$	$\int_0^1 dx\ g_1^n$
$g_1^n = C$	3	$C = -0.41 \pm 0.05 \pm 0.06$	$-0.0055 \pm 0.0007 \pm 0.0008$	$-0.0414 \pm 0.0044 \pm 0.0057$
$g_1^n = C/(x \ln^2 x)$	4	$C = -0.125 \pm 0.014 \pm 0.016$	$-0.0291 \pm 0.0032 \pm 0.0036$	$-0.0649 \pm 0.0062 \pm 0.0085$
$g_1^n = Cx^{-\alpha}$	5	$C = -0.014 \pm 0.007 \pm 0.004$ $\alpha = 0.92 \pm 0.16 \pm 0.09$	$-0.14 \pm \infty \pm \infty$	-0.17
$g_1^n = Cx^{-\alpha}(1-x)^{\beta}$	11	$C = -0.034 \pm 0.021 \pm 0.011$ $\alpha = 0.70 \pm 0.18 \pm 0.10$ $\beta = 3.2 \pm 1.6 \pm 0.7$	$-0.031 \pm 0.022 \pm 0.013$	$-0.067 \pm 0.024 \pm 0.017$

spin structure function g_1^n at low x question the validity of a naive application of the Regge theory to the present-day spin structure experiments. It would seem unnatural if the situation was any better with the proton and deuteron structure functions: most likely, the experiments have not yet reached the kinematic range and precision required to see the true asymptotic behavior at low x. A possible interpretation of our data is that the neutron structure function (or at least its derivative with respect to x) is dominated by the sea quark and gluon contributions, which in fact could produce very divergent behavior at low x[71] (we will return to this question in Chapter 5). Consequently, we do not quote a number for the quark helicity contribution $\Delta\Sigma = \Delta u + \Delta d + \Delta s$.

Figures 4.9 and 4.10 show the values of the Ellis-Jaffe and Bjorken integrals integrated from a given $x_{\min}$ value to 1. The integral over the data range of the neutron structure function exceeds the Ellis-Jaffe prediction by about factor of two, and the Bjorken sum rule is almost saturated by the integral over the measured range.

Even if the neutron and proton integrals diverge, the Bjorken sum rule could still be evaluated from the present data. The difference $(g_1^p - g_1^n)(x)$ is a purely non-singlet, valence quark distribution (if one assumed $\Delta\bar{u} = \Delta\bar{d}$) and is expected to behave much softer at low x than its singlet counterpart.[71] The difference $(g_1^p - g_1^n)(x)$ is plotted versus x in Fig. 4.11. We take E143[10] and SMC[12] data to evaluate the contribution from the proton structure function. The difference of two structure functions indeed shows a more convergent behavior; fitting a free power-law function $(g_1^p - g_1^n) = Cx^{-\alpha}$ to the first five points ($x \leq 0.1$), we get

$$\begin{aligned} C &= 0.120 \pm 0.036\ (\text{stat.}) \pm 0.005\ (\text{syst.}) \\ \alpha &= 0.52 \pm 0.10\ (\text{stat.}) \pm 0.04\ (\text{syst.})\ . \end{aligned} \tag{4.5}$$

The contributions to the integral are

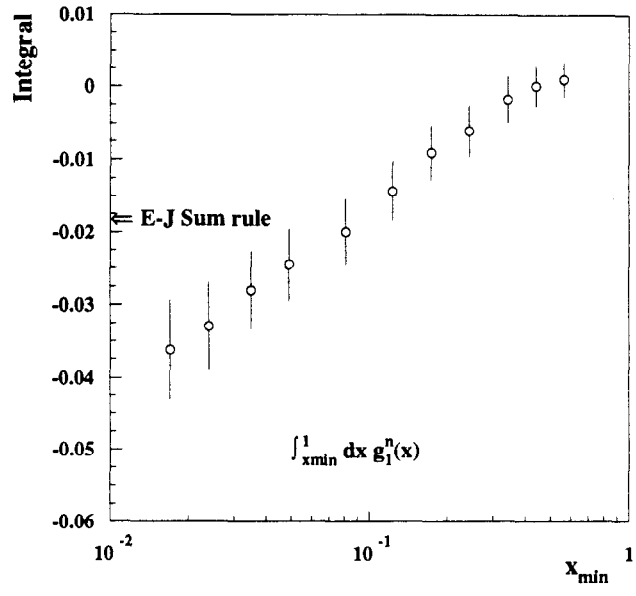

Fig. 4.9. The spin dependent structure function $g_1^n(x)$ of the neutron integrated from $x_{\min}$ to 1 and plotted versus $x_{\min}$. The statistical and systematic errors have been added in quadrature. The errors in the plot are strongly correlated from point to point.

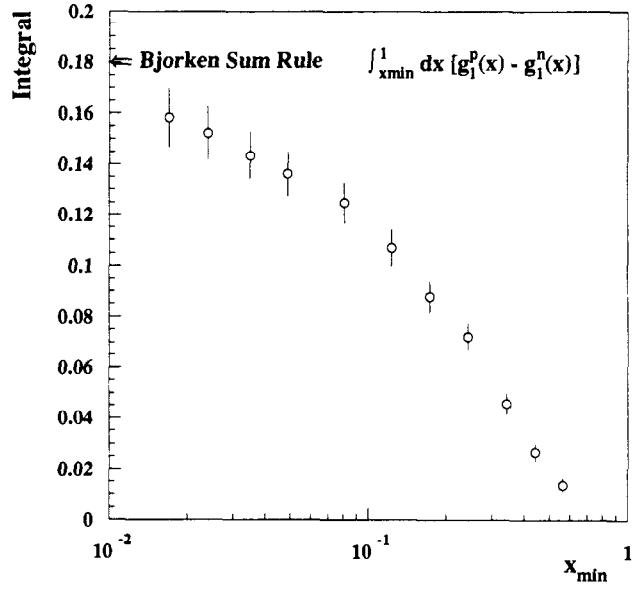

Fig. 4.10. The difference between the spin dependent structure functions g_1 of the proton and neutron integrated from $x_{\min}$ to 1 and plotted versus $x_{\min}$. E154 data was used to evaluate g_1^n, and a fit to the E143 and SMC data was used for g_1^p. The statistical and systematic errors have been added in quadrature. The errors in the plot are strongly correlated from point to point.

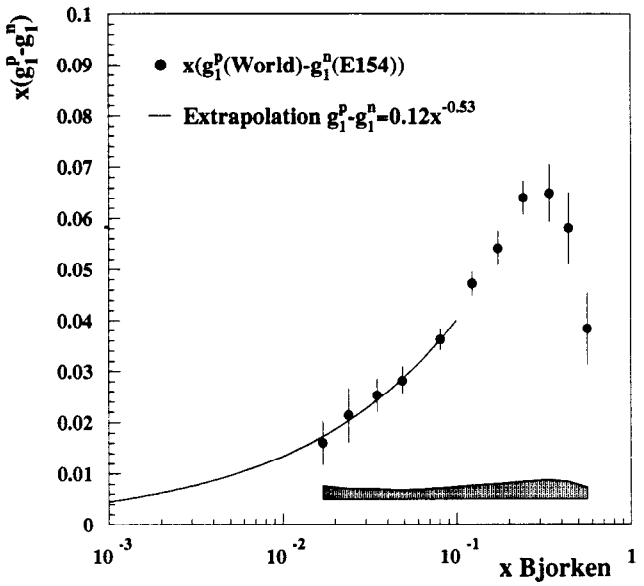

Fig. 4.11. The difference between the spin dependent structure functions xg_1 of the proton and neutron. E154 data was used to evaluate g_1^n, and a fit to the E143 and SMC data was used for g_1^p.

$$\begin{aligned}
\int_{0.0135}^{0.7} dx\ (g_1^p - g_1^n) &= 0.1583 \pm 0.0052\ (\text{stat.}) \pm 0.0103\ (\text{syst.}) \\
\int_{0}^{0.0135} dx\ (g_1^p - g_1^n) &= 0.0321 \pm 0.0130\ (\text{stat.}) \pm 0.0071\ (\text{syst.}) \qquad (4.6) \\
\int_{0.7}^{1} dx\ (g_1^p - g_1^n) &= 0.0017 \pm 0.0003\ (\text{stat.}) \pm 0.0001\ (\text{syst.})\ ,
\end{aligned}$$

and the full integral is

$$\int_0^1 dx\ (g_1^p - g_1^n) = 0.192 \pm 0.016\ (\text{stat.}) \pm 0.018\ (\text{syst.}) \qquad (4.7)$$

in a reasonable agreement with the prediction $\Gamma^{p-n} = 0.181 \pm 0.003$ evaluated at $Q^2 = 5$ GeV^2 to $O(\alpha_S^3)$ with $\alpha_S(M_Z) = 0.118 \pm 0.003$.[20] This result is quite robust against possible variations in the low x behavior: even if we assumed "Regge" behavior $(g_1^p - g_1^n) \sim const$ at low x, the full integral would be $\Gamma^{p-n} = 0.170 \pm 0.006 \pm 0.011$, consistent within uncertainties with the value in Eq. (4.7).

CHAPTER 5

NEXT-TO-LEADING ORDER QCD ANALYSIS OF THE POLARIZED DEEP INELASTIC SCATTERING DATA

5.1 Introduction

For more than two decades since the pioneering experiments in the late 1970's at SLAC,[6,7] deep inelastic scattering (DIS) of polarized leptons off polarized targets has provided information about the internal spin structure of the proton and neutron. Recent progress in both experiment and theory has made polarized DIS into a powerful tool for QCD phenomenology. On the theoretical side, a full calculation of the Next-to-Leading Order (NLO) spin-dependent anomalous dimensions has been recently completed.[37] This provides for a perturbative QCD (pQCD) analysis of polarized DIS analogous to the treatment of the unpolarized data.[144–146] At the same time, improvement in the precision of the experimental data and increased kinematic coverage has made such an analysis increasingly more meaningful.

The data reported in this dissertation is the newest addition to the world data on the spin-dependent structure functions. They are the most precise up to date determination of the neutron structure function g_1^n. The kinematic range of the measurement was extended compared to the previous SLAC experiments[9–11] to $0.014 \leq x \leq 0.7$ in the Bjorken variable and $1\ \mathrm{GeV}^2 \leq Q^2 \leq 17\ \mathrm{GeV}^2$ in the four-momentum transfer. Two independent spectrometers used in E154 also provided for a possibility to study the Q^2 dependence of the structure function g_1^n. The kinematic coverage of the polarized DIS experiments is illustrated in Fig. 5.1. Although, as we mentioned in Section 4.1.2, the present data are consistent with the assumption that the asymmetry A_1 (or the ratio g_1/F_1) is independent of Q^2, information on

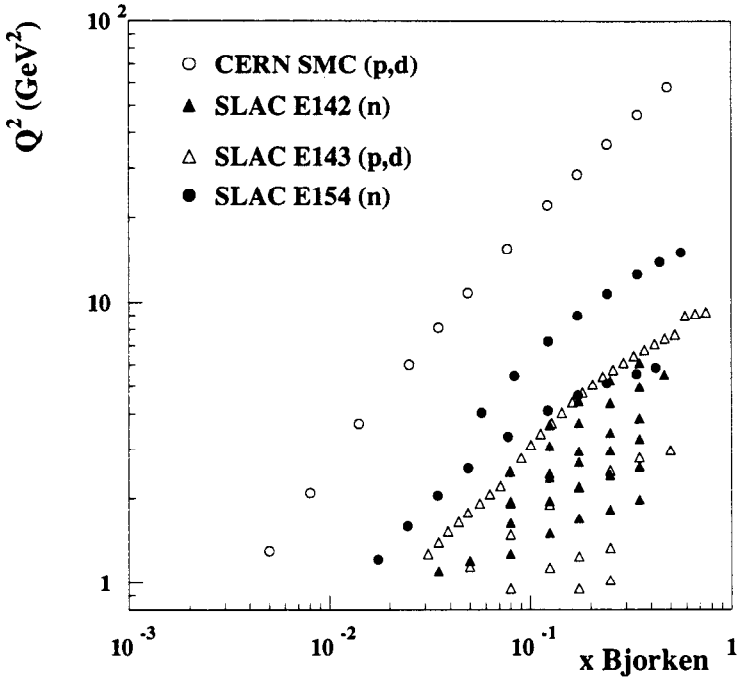

Fig. 5.1. Kinematic coverage of the present polarized DIS experiments.

the evolution of asymmetries can be extracted from the data in the framework of a consistent pQCD analysis.

As was discussed in Section 4.4.3, the relatively large values of g_1^n at low x show an apparent disagreement with a traditional Regge behavior that could be attributed to a large contribution to g_1^n from the singlet quark distribution. This implies the importance of the dynamics of polarized quark and gluon distributions, and in particular, a possibly sizable Q^2 dependence of the experimental asymmetries. It is therefore important to perform a consistent NLO analysis of the available data that would take into account theoretical and experimental uncertainties, both statistical and systematic. Among the analyses performed so far,[63,86,147] only Ref. [63] gives a detailed treatment of errors involved in extraction of the first moments of polarized parton distributions; however, the effect of experimental systematic uncertainties was underestimated. The analyses of Ref. [63,86,147] had been done before the E154

results became available, and it is interesting to see what additional information can be extracted from the new data.

In this Chapter, while paying a careful attention to the theoretical and experimental errors involved in the analysis, we will:

1. Discuss the results on the Next-to-Leading Order perturbative QCD analysis of the world data on polarized deep inelastic scattering;

2. Estimate the Q^2 dependence of the experimental asymmetries;

3. Discuss additional constraints that can be placed on the low x extrapolation of the experimental data;

4. Extract the first moments of the polarized parton distributions and structure functions.

5.2 Formalism

In the following, we will follow the notation introduced in Section 1.3. The helicity-dependent distribution functions of the quarks and antiquarks will be denoted as $\delta q(x)$ and $\delta\bar{q}(x)$, respectively. The total polarized distribution of the quarks of flavor q will be denoted as $\Delta q(x) \equiv \delta q(x) + \delta\bar{q}(x)$. The polarized gluon distribution is $\Delta G(x)$. Whenever the explicit x dependence is not specified, we will imply the *first moment* of a polarized distribution, *i.e.* $\Delta q \equiv \int_0^1 dx\ \Delta q(x)$ and $\Delta G \equiv \int_0^1 dx\ \Delta G(x)$.

In the QCD-improved parton model, the polarized structure function $g_1(x)$ of the nucleon is related to the polarized quark, antiquark, and gluon distributions $\delta q(x)$, $\delta\bar{q}(x)$, and $\Delta G(x)$ via the factorization theorem[148]

$$g_1(x,Q^2) = \frac{1}{2}\sum_q^{N_f} e_q^2 \left[C_q \otimes (\delta q + \delta\bar{q}) + \frac{1}{N_f} C_G \otimes \Delta G \right] \tag{5.1}$$

with the convolution $\otimes$ defined as

$$(C \otimes q)(x,Q^2) = \int_x^1 \frac{dz}{z} C\left(\frac{x}{z}, \alpha_S\right) q(z,Q^2). \tag{5.2}$$

The sum is over all active quark flavors N_f.

The first moments of the structure functions of the proton and neutron g_1^p and g_1^n allow one to test the fundamental Bjorken sum rule[26] and determine the helicity contents of the proton. The information on the x and Q^2 dependence gives insight into the perturbative and non-perturbative dynamics of quarks and gluons inside the nucleon. Coefficient functions $C_{q,G}(x, \alpha_S)$ correspond to the hard scattering photon-quark(gluon) cross sections and are also referred to as Wilson coefficients. They are calculated in perturbative QCD as an expansion in powers of the strong coupling constant α_S:

$$C(x, \alpha_S) = C^{(0)}(x) + \frac{\alpha_S(Q^2)}{2\pi} C^{(1)}(x) + \cdots . \tag{5.3}$$

In the leading order, $C_q^{(0)} = \delta(1-x)$ and $C_G^{(0)} = 0$ according to the simple partonic picture (*i.e.* gluons carry no net electric charge and do not couple directly to the photons, so the structure functions depend only on quark contributions, *cf.* Eq. (1.48)). The polarized NLO coefficient functions $C_q^{(1)}$ and $C_G^{(1)}$ in the modified minimal subtraction ($\overline{\text{MS}}$) renormalization and factorization schemes are given in Ref. [37]. In the following, we will follow the conventional approach[86,145] and use the fixed-flavor scheme and set $N_f = 3$ in Eq. (5.1). This is justified since the Q^2 of the experiments is relatively low and even above the pair-creation threshold the heavy quarks (charm and bottom) contribute very little to the structure function g_1. The heavy quark contributions will be included in the two-loop running of α_S[20]

$$\frac{\alpha_S(Q^2)}{4\pi} = \frac{1}{\beta_0 \ln(Q^2/\Lambda_{(f)}^2)} - \frac{\beta_1}{\beta_0^3} \frac{\ln\left(\ln(Q^2/\Lambda_{(f)}^2)\right)}{\left(\ln(Q^2/\Lambda_{(f)}^2)\right)^2} \tag{5.4}$$

where the coefficients of the QCD beta function are $\beta_0 = 11 - 2f/3$ and $\beta_1 = 102 - 38f/3$. The number of active flavors f in $\alpha_S(Q^2)$ is determined by the number of quarks with $m_q^2 \leq Q^2$, $\Lambda_{(f)}$ are determined by the matching condition at the quark threshold $\alpha_S(m_q^2, f) = \alpha_S(m_q^2, f+1)$. For consistency with the evolution of the unpolarized distributions, we take[145]

$$\Lambda_{(3,4,5)}^{\overline{\text{MS}}} = 248,\ 200,\ 131 \quad \text{MeV} \tag{5.5}$$

with $m_c = 1.5$ GeV and $m_b = 4.5$ GeV that corresponds to $\alpha_S(M_Z^2) = 0.109$ or $\alpha_S(5\ \mathrm{GeV}^2) = 0.237$. We include the uncertainty associated with the value of α_S as will be discussed below. The parton distributions in Eq. (5.1) are those of the proton. The neutron structure function is obtained by the isospin interchange $u \Leftrightarrow d$, and the deuteron structure function is defined as

$$g_1^d = (1/2)(g_1^p + g_1^n)(1 - 1.5\omega_D)\ , \tag{5.6}$$

where the D-state probability $\omega_D = 0.05 \pm 0.01$.[149]

The Q^2 evolution of the parton densities is governed by the DGLAP equations[41–43]

$$\begin{aligned} Q^2\frac{d}{dQ^2}\Delta q_{\rm NS}^{\eta}(x) &= \frac{\alpha_S(Q^2)}{2\pi}P_{\rm NS}^{\eta}\otimes\Delta q_{\rm NS}^{\eta}, \quad \eta = \pm 1 \\ \text{and}\quad Q^2\frac{d}{dQ^2}\begin{pmatrix}\Delta\Sigma(x)\\ \Delta G(x)\end{pmatrix} &= \frac{\alpha_S(Q^2)}{2\pi}\begin{pmatrix}P_{qq} & P_{qG}\\ P_{Gq} & P_{GG}\end{pmatrix}\otimes\begin{pmatrix}\Delta\Sigma\\ \Delta G\end{pmatrix}\ , \end{aligned} \tag{5.7}$$

where the index NS stands for the the non-singlet quark distributions: valence ($\eta = 1$) $\Delta u_V(x,Q^2) = \delta u - \delta\bar{u}$, $\Delta d_V(x,Q^2) = \delta d - \delta\bar{d}$, and the $SU(3)_{\rm flavor}$ non-singlet combinations ($\eta = -1$) $\Delta q_3(x,Q^2) = \Delta u(x,Q^2) - \Delta d(x,Q^2)$ and $\Delta q_8(x,Q^2) = \Delta u(x,Q^2) + \Delta d(x,Q^2) - 2\Delta s(x,Q^2)$. The $SU(3)_{\rm flavor}$ singlet distribution is $\Delta\Sigma = \Delta u(x,Q^2) + \Delta d(x,Q^2) + \Delta s(x,Q^2)$. The splitting functions $P_{\rm NS}^{\eta}$ and P_{ij} are calculated perturbatively

$$P(x,\alpha_S) = P^{(0)}(x) + \frac{\alpha_S(Q^2)}{2\pi}P^{(1)}(x) + \cdots \tag{5.8}$$

with the leading order functions given in Eq. (1.58), and the next-to-leading order expressions recently obtained in Ref. [37]. Note that in the leading order, the evolution of both types of non-singlet distributions is the same: $P_{\rm NS}^{(0)\eta=-1} = P_{\rm NS}^{(0)\eta=+1} = P_{qq}^{(0)}$ and the differences only appear in the next-to-leading order. Starting with a parameterization of the parton densities at some initial scale Q_0^2, the distributions at any

value of $Q^2 > Q_0^2$ are obtained using the solutions of the NLO DGLAP equations in the Mellin n-moment space[39,150] with the n-th moment defined by

$$f(n) = \int_0^1 dx\, x^{n-1} f(x). \tag{5.9}$$

In Mellin space, the DGLAP evolution is controlled by the matrix of anomalous dimensions that are related to the n-th moments of the splitting functions. We use the convention of Ref. [150] for the anomalous dimensions

$$\gamma_{ij}(n) = \left(\frac{\alpha_S(Q^2)}{4\pi}\right) \gamma_{ij}^{(0)}(n) + \left(\frac{\alpha_S(Q^2)}{4\pi}\right)^2 \gamma_{ij}^{(1)}(n) + \cdots \tag{5.10}$$

with $\gamma_{ij}^{(0)}(n) = -4 \int_0^1 dx\, x^{n-1} P_{ij}^{(0)}(x)$ and $\gamma_{ij}^{(1)}(n) = -8 \int_0^1 dx\, x^{n-1} P_{ij}^{(1)}(x)$. The complete set of the LO and NLO anomalous dimensions can be found in Appendix B. The parton densities evolved in Mellin space are inverted back to Bjorken x space using the prescription of Ref. [150] (see Appendix B).

One of the primary uncertainties in the interpretation of the deep inelastic scattering data at the next-to-leading order is the relative freedom in defining the hard scattering cross sections $C_{q,G}^{(1)}$ and the singlet quark density $\Delta\Sigma$ in Eq. (5.1), known as the factorization scheme dependence.[39,61,62] The factorization theorem states that at some scale Q^2, the DIS cross section can be separated into the hard part that can be calculated in perturbation theory, and soft non-perturbative quantities sensitive to the nucleon wavefunction, the parton distribution functions. Such separation is *a priori* arbitrary; since the hard-scattering cross sections $C_{q,G}$ are calculated perturbatively and need to be renormalized, one defines them by specifying an explicit renormalization procedure (*factorization scheme*)[39,62][1]. In the polarized case, the situation is further complicated by the freedom of a definition

[1]In DIS, the dependence on the renormalization procedure comes in two places. The *factorization scheme* applies to renormalization of the hard-scattering cross sections in Eq. (5.1). There is also a genuine *renormalization scheme* that defines the way the strong coupling is renormalized in Eq. (5.7). The two renormalization procedures do not have to be the same. However, one most often chooses the same schemes, such as $\overline{\text{MS}}$ in both cases.

of the γ_5 matrix and the Levi-Civita tensor in $n \neq 4$ dimensions[61] in dimensional regularization.[151] The choice of scale at which the factorization theorem is applied (a *factorization scale*) is also *a priori* arbitrary[152]; so in a complete calculation one always specifies a particular factorization scheme, and chooses a scale (in DIS one typically uses Q^2 as a factorization scale, as we did in Eq. (5.1)). Additional uncertainty comes from the lack of knowledge of the higher order corrections, and is conventionally referred to as a *renormalization scale* dependence (*i.e.* dependence of the results on a choice of the scale for the coupling constant in Eq. (5.3)). Several prescriptions for setting the renormalization scale exist.[153] Typically, one chooses Q^2 to be the renormalization scale and the uncertainty is estimated by varying the scale.

Given the anomalous dimensions and Wilson coefficients in one factorization scheme, any other factorization scheme can be constructed by a transformation[39]

$$\begin{aligned} \gamma_{\rm NS}^{\eta}(n) &\rightarrow \gamma_{\rm NS}^{\eta}(n) + 4\beta_0 Z_{qq}(n) \\ \gamma_{ij}^{(1)}(n) &\rightarrow \gamma_{ij}^{(1)}(n) + 2\left[Z(n), \gamma^{(0)}(n)\right]_{ij} + 4\beta_0 Z_{ij}(n) \qquad (5.11) \\ \text{and} \quad C_q^{(1)}(n) &\rightarrow C_q^{(1)}(n) - Z_{qq}(n) \\ C_G^{(1)}(n) &\rightarrow C_G^{(1)}(n) - Z_{qG}(n)\,, \qquad (5.12) \end{aligned}$$

where $Z(n)$ is an arbitrary 2×2 scheme transformation matrix. The NLO anomalous dimensions and coefficient functions are given in Ref. [37] in the $\overline{\rm MS}$ scheme with the definition of the γ_5 matrix following Ref. [151]. The specific feature of this scheme is that the first moment of the gluon coefficient function vanishes $C_G^{(1)}(n=1) = 0$, and the gluon density does not contribute to the integral of g_1. This has been a matter of debate[56–58,61] with several authors advocating the scheme change by which the axial anomaly contribution $-(\alpha_S(Q^2)/4\pi)\sum_q e_q^2 \Delta G$ is included into the integral of g_1. This implies that for the first moment of the gluon coefficient function

$$C_G^{(1)}(n=1) = -N_f\,. \qquad (5.13)$$

An attractive feature of such a scheme is that the total quark helicity in this case is redefined as

$$\Delta\Sigma \to \Delta\Sigma(Q^2) + \frac{N_f \alpha_S(Q^2)}{2\pi}\Delta G(Q^2) \tag{5.14}$$

and is independent of Q^2 even beyond the leading order. It could also resurrect the intuitive Quark-Parton model expectation $\Delta\Sigma \approx 0.6 - 0.7$ and explain the violation of the Ellis-Jaffe sum rule if the product $\alpha_S(Q^2)\Delta G(Q^2)$ turned out to be large.[56–58]

The product $\alpha_S(Q^2)\Delta G(Q^2)$ is independent of Q^2 in the leading order since its anomalous dimension expansion starts at order α_S^2.[154] This implies that as α_S decreases logarithmically with Q^2, ΔG grows as $1/\alpha_S(Q^2)$. This growth is compensated by the increasing (with opposite sign) orbital angular momentum contribution $\langle L_z \rangle$[66,155] in order to satisfy the proton angular momentum sum rule

$$\frac{1}{2}\Delta\Sigma + \Delta G + \langle L_z \rangle = \frac{1}{2}. \tag{5.15}$$

Another consequence is that the ambiguity in the definition of the total quark helicity in Eq. (5.14) does not vanish at infinite Q^2, or in other words, the quark helicity can only be defined up to a Q^2-independent (in the leading order) constant. However, one does not lose the predictive power of perturbative QCD: as long as the factorization and renormalization schemes are used consistently, NLO predictions can be made for the spin dependent structure functions and other hadronic processes involving spin degrees of freedom (once the parton distributions are determined in one scheme and at one scale).

A transformation from the $\overline{\text{MS}}$ scheme of t'Hooft and Veltman[151] to the so-called Adler-Bardeen (AB hereafter) scheme that satisfies Eq. (5.13) was constructed in Ref. [63]. The inverse Mellin transform $Z(x)$ of matrix $Z(n)$ in Equations (5.11) and (5.12) was taken to be independent of x, the first moments of the matrix elements were fixed by the conservation of the non-singlet axial current ($Z_{qq}(n = 1) = 0$) and

Table 5.1. NLO initial unpolarized parton distributions at $Q_0^2 = 0.34$ GeV^2.[145]

$u_V(x,Q_0^2)$	=	$0.988x^{-0.457}(1-x)^{3.380}(1+1.58x^{1/2}+2.58x+18.1x^{3/2})$
$d_V(x,Q_0^2)$	=	$0.182x^{-0.684}(1-x)^{4.113}(1+2.51x^{1/2}+25.0x+11.4x^{3/2})$
$\bar{Q}(x,Q_0^2)$	=	$0.545x^{-0.70}(1-x)^{8.33}(1+2.65x)$
$G(x,Q_0^2)$	=	$26.2x^{0.9}(1-x)^{4.0}$

by Eq. (5.13), and the lower entries of the matrix were taken to be zero. Hence, the transformation matrix is

$$Z(n)_{\overline{\rm MS}\to{\rm AB}} = \frac{1}{n}\begin{pmatrix} 0 & N_f \\ 0 & 0 \end{pmatrix} . \tag{5.16}$$

This scheme is the minimal modification of $\overline{\rm MS}$ since it preserves the low and high x behavior of the coefficient functions and anomalous dimensions, and thus the asymptotic behavior of parton distributions is not modified. In order to demonstrate the effects of the factorization scheme dependence, we perform our calculations in both $\overline{\rm MS}$ and AB schemes.

5.3 Fits

Following the ansatz of Ref. [86], we parameterize the polarized parton distribution at the low initial scale $Q_0^2 = 0.34$ GeV^2 as follows:

$$\Delta f(x,Q_0^2) = A_f x^{\alpha_f}(1-x)^{\beta_f} f(x,Q_0^2) , \tag{5.17}$$

where $\Delta f = \Delta u_V$, Δd_V, $\Delta\bar{Q}$, ΔG are the polarized valence, sea, and gluon distributions (see below for the definition of $\Delta\bar{Q}$), and $f(x,Q_0^2)$ are the unpolarized parton distributions from Ref. [145] (Table 5.1).

Since the inclusive deep inelastic scattering does not provide sufficient information about the flavor separation of the polarized sea, we assume isospin symmetry

$$\delta\bar{u} = \delta\bar{d} \equiv \frac{1}{2}\left(\delta\bar{u} + \delta\bar{d}\right) . \tag{5.18}$$

Under this assumption, the sea quark contribution to the polarized structure functions of the proton and neutron is the same:

$$g_1^{p\ \mathrm{sea}} = g_1^{n\ \mathrm{sea}} = (5/9)C_q \otimes \left[1/2(\delta\bar{u} + \delta\bar{d}) + 1/5\delta\bar{s}\right] . \tag{5.19}$$

Thus, the inclusive DIS does not probe the light and strange sea independently[2], and the only sensitivity to the difference between $\delta\bar{u}$, $\delta\bar{d}$, and $\delta\bar{s}$ comes from the difference in the evolution of the two types of non-singlet distributions ($\eta = \pm 1$ in Eq. (5.7)). However, if one started with the equal sea distributions ($\delta\bar{u} = \delta\bar{d} = \delta\bar{s}$) at $Q_0^2 = 0.34$ GeV^2, at $Q^2 = 100$ GeV^2 and $x = 0.001$ the difference between the light and strange sea distributions would only be $\approx 2\%$ (and smaller at higher x), beyond the reach of the present-day experiments. Hence, we will parameterize a particular combination of the sea quark distributions that appears in Eq. (5.19):

$$\Delta\bar{Q} \equiv 1/2(\delta\bar{u} + \delta\bar{d}) + 1/5\delta\bar{s} . \tag{5.20}$$

Furthermore, we assume the x dependence of the polarized strange and light sea to be the same and fix the normalization of the strange sea by

$$\delta s = \lambda_s \frac{\delta\bar{u} + \delta\bar{d}}{2} = \frac{\lambda_s}{1 + \lambda_s/5}\Delta\bar{Q} , \tag{5.21}$$

with the $SU(3)_{\mathrm{flavor}}$ symmetry breaking parameter λ_s varying between 1 and 0 (where the latter choice corresponds to the unpolarized strange sea).

The positivity constraint,

$$|\delta f(x)| \leq f(x) \tag{5.22}$$

enforced (within uncertainties) at the initial scale Q_0^2 holds at all scales $Q^2 > Q_0^2$; it leads to constraints $\alpha_f \geq 0$ and $\beta_f \geq 0$. In addition, we assume the helicity retention properties of the parton distributions[49] (see Section 1.4.1) that constrain[3] $\beta_f = 0$.

[2]Information on the flavor separation of the polarized sea could be obtained from the *semi-inclusive* reactions, *i.e.* when a hadron that carries the struck quark is observed in the final state.

[3]We have checked that the data are consistent with this assumption.

Table 5.2. Fitted values of the free parameters in Eq. (5.17) in $\overline{\text{MS}}$ and AB schemes. Also quoted are the statistical, systematic, and theoretical errors.

	$\overline{\text{MS}}$				AB			
	Value	Stat.	Syst.	Theory	Value	Stat.	Syst.	Theory
A_u	0.99	$^{+0.08}_{-0.08}$	$^{+0.04}_{-0.05}$	$^{+0.97}_{-0.11}$	0.96	$^{+0.07}_{-0.06}$	$^{+0.03}_{-0.05}$	$^{+0.96}_{-0.09}$
A_d	−0.74	$^{+0.14}_{-0.21}$	$^{+0.05}_{-0.07}$	$^{+0.05}_{-1.28}$	−0.82	$^{+0.05}_{-0.05}$	$^{+0.07}_{-0.06}$	$^{+0.31}_{-1.21}$
A_Q	−0.01	$^{+0.02}_{-0.05}$	$^{+0.01}_{-0.02}$	$^{+0.01}_{-0.35}$	−0.03	$^{+0.01}_{-0.02}$	$^{+0.01}_{-0.01}$	$^{+0.03}_{-0.06}$
A_G	1.3	$^{+1.1}_{-0.7}$	$^{+0.7}_{-0.5}$	$^{+0.2}_{-1.3}$	0.1	$^{+2.3}_{-1.1}$	$^{+1.7}_{-1.1}$	$^{+0.1}_{-0.6}$
α_u	0.64	$^{+0.06}_{-0.07}$	$^{+0.03}_{-0.05}$	$^{+0.36}_{-0.06}$	0.54	$^{+0.08}_{-0.06}$	$^{+0.03}_{-0.04}$	$^{+0.56}_{-0.05}$
α_d	0.25	$^{+0.16}_{-0.11}$	$^{+0.07}_{-0.04}$	$^{+0.75}_{-0.03}$	0.40	$^{+0.20}_{-0.12}$	$^{+0.07}_{-0.13}$	$^{+0.53}_{-0.34}$
α_Q	0.01	$^{+0.19}_{-0.01}$	$^{+0.13}_{-0.01}$	$^{+0.55}_{-0.01}$	0.00	$^{+0.17}_{-0.00}$	$^{+0.17}_{-0.00}$	$^{+0.00}_{-0.00}$
α_G	0.7	$^{+0.4}_{-0.5}$	$^{+0.3}_{-0.3}$	$^{+0.1}_{-0.6}$	0.0	$^{+0.7}_{-0.0}$	$^{+1.0}_{-0.0}$	$^{+1.0}_{-0.0}$

The remaining eight coefficients are determined by the fit to the available data on the spin dependent structure function $g_1^{p,n,d}$ of the proton, neutron, and deuteron with $Q^2 > 0.95$ GeV^2. We determine the structure functions at the experimental values of Q^2 using the quoted results for g_1/F_1. The unpolarized structure function F_1 is obtained from the recent parameterization of $F_2(x, Q^2)$ from NMC[129] and the fit to the data on $R(x, Q^2)$, the ratio of longitudinal to transverse photoabsorption cross sections, from SLAC.[79] The weight of each point is determined by the statistical error. The multi-parameter fit is performed using MINUIT from the CERN program library.[156] The best fit coefficients are listed in Table 5.2 and the χ^2 contributions from various experiments are listed in Table 5.3.

Table 5.3. Contributions to the total χ^2 from each experiment.

Exp.	E142	E143-p	E143-d	SMC-p	SMC-d	E154	total
Source	[9]	[10,77]	[11,77]	[12]	[13]	Chapter 4	
Points	32	40	34	12	12	18	149
χ^2 ($\overline{\text{MS}}$)	24.6	45.5	33.7	11.0	15.9	9.8	140.4
χ^2 (AB)	24.6	48.6	31.9	11.3	16.5	9.4	142.3

5.4 Error analysis

5.4.1 Experimental errors

The statistical errors on the parameters of the fit could in principle be extracted from the correlation matrix returned by the fitting program.[156] However, the estimates provided by MINUIT should be taken with some caution: the χ^2 distribution around the minimum in the parameter space is quite shallow (the precision of the data is still limited), and the correlation matrix returned by the program is not always accurate. In addition, the correlation matrix in the parameter space is not very practical if one wants to calculate the errors on the structure functions, or uncertainty in the Q^2 evolution. Moreover, it is not trivial to include the systematic errors into the χ^2 formalism.[157]

Instead of relying on MINUIT estimates, we use the standard error propagation technique. The statistical errors on the parameters of the fit as well as on the extracted parton densities δq, $\delta\bar{q}$, and ΔG can be calculated by adding in quadrature statistical contributions from experimental points. The weight of every point is obtained by varying the point within its statistical error and calculating the change in the parton density. This is equivalent to taking a derivative of the quantity in question with respect to the value of g_1 at every experimental point by finite differences[4]; thus

[4] *cf.* Section 3.11 where such a technique was applied to the radiative corrections

$$\sigma^2_{\rm stat}(\Delta f) = \sum_i \left(\frac{\partial \Delta f}{\partial g_1^i}\right)^2 \sigma^2_{\rm stat}(g_1^i)\ , \tag{5.23}$$

where f is, for instance, a parton density, and the sum is over all experimental points g_1^i.

One has to keep in mind the fact that the standard error propagation similar to Eq. (5.23) is limited to the case when the errors on each point are small compared to the ratio of the second and first derivatives $(\partial^2 \Delta f/\partial^2 g_1^i)/(\partial \Delta f/\partial g_1^i)$ (so that the Taylor expansion that leads to this formula converges fast).[20] If this is not the case, the higher order derivatives have to be taken into account. The RMS of such distribution may not be a good measure of the uncertainty and one has to define the error in terms of a probability interval. We define σ_+ and σ_- errors in such a way that the probability is 34% that the value Δf is within intervals $[f - \sigma_-(\Delta f); \langle \Delta f \rangle]$ and $[\langle \Delta f \rangle; \Delta f + \sigma_+(\Delta f)]$ (where $\langle \Delta f \rangle$ is the value of the maximum likelihood[5] of the distribution of Δf. The distributions of the quantities Δf (for instance, a parton density, or a value of g_1 at some particular x and Q^2) is obtained by randomizing every experimental point independently according to a Gaussian distribution with mean of the measured value of g_1^i and variance of $\sigma^2_{\rm stat}(g_1^i)$ and repeating the NLO fit. A typical "statistical" sample consists of 800 fits. The distribution of first moments of the polarized parton densities is shown in Fig. 5.2.

The systematic errors for every point are usually dominated by the normalization errors (target and beam polarizations, dilution factor, etc.). Thus the systematic errors are to a large extent correlated point to point within one experiment[6]. We therefore assume 100% correlated systematic errors for any given experiment and add systematic contributions within one experiment linearly. The propagated sys-

[5]Note that for asymmetric distributions $\langle \Delta f \rangle$ may not coincide with the mean of the distribution.

[6]This includes both proton and deuteron data taken in a single experiment, such as E143 and SMC.

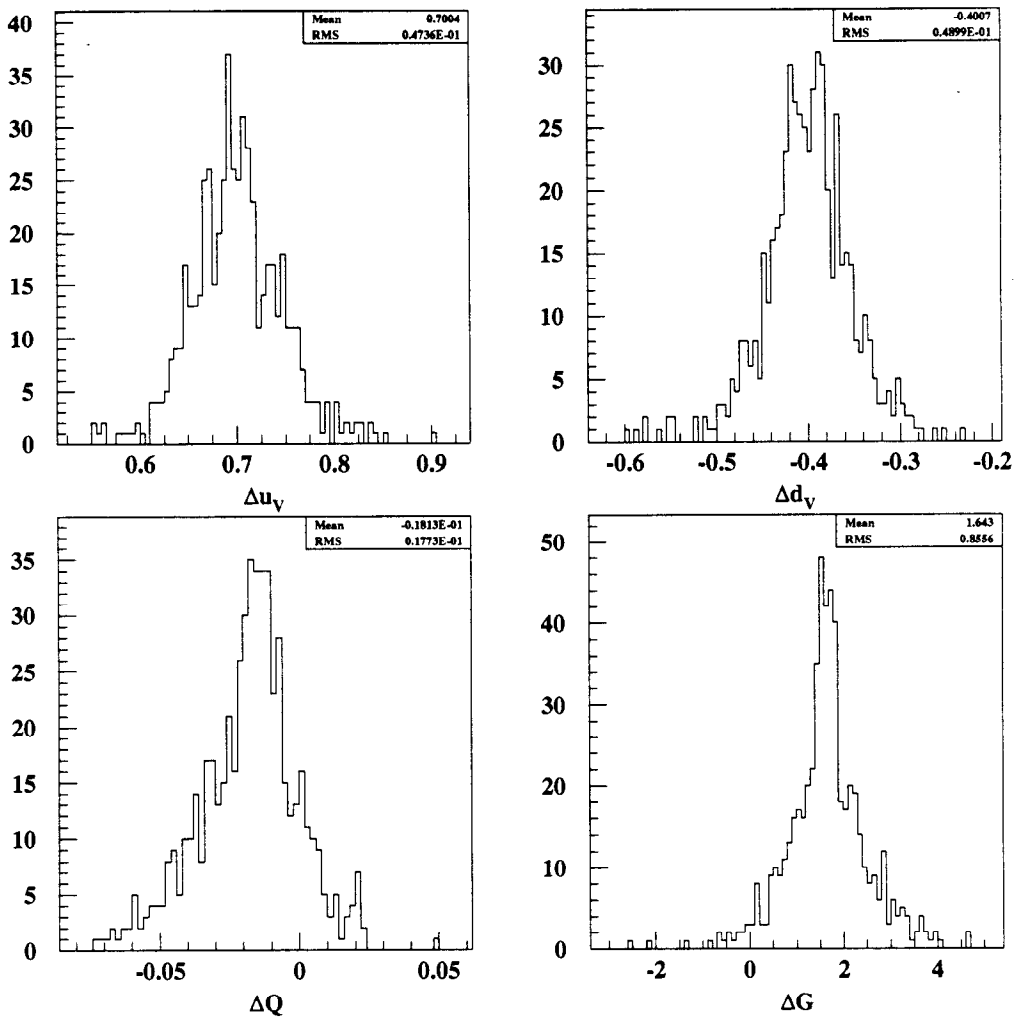

Fig. 5.2. Distributions of the first moments of the polarized parton densities obtained in the $\overline{\text{MS}}$ scheme by randomizing the input values of g_1 as described in the text.

tematic errors of each experiment are then added quadratically to obtain the systematic errors on parton densities. Within our "Monte Carlo" framework, it means that one random variable (with normal Gaussian distribution) that represents the fraction of the systematic error is generated for every experiment, and all points are shifted by that fraction.

5.4.2 Theoretical errors

The biggest source of theoretical uncertainty is the error on the value of α_S. We estimate it by repeating the fits[7] with $\alpha_S(M_Z^2)$ varied in the range allowed by the unpolarized DIS experiments[20] $\alpha_S(M_Z^2) = 0.108 - 0.116$. The scale uncertainty is included in the error on α_S. We also vary current quark masses in the range $m_c = 1 - 2$ GeV and $m_b = 4 - 5$ GeV. The sensitivity to the shape of the initial distributions and the value of the starting scale Q_0^2 is estimated by repeating the fit with initial unpolarized distributions taken from Ref. [144] at $Q_0^2 = 1$ GeV^2. The effect of the $SU(3)_{\text{flavor}}$ breaking is estimated by varying the parameter λ_s from 1 to 0. Possible higher twist effects are neglected since they are expected to drop as $1/W^2$[55] and the cut $W^2 > 4$ GeV^2 has been applied to all the data with the majority of them exceeding $W^2 > 8$ GeV^2.

5.5 Results and discussion

Results for the structure functions of the proton and neutron g_1^p and g_1^n at 5 GeV^2 are compared to the experimental data in Fig. 5.3. They are compared to the fits from Ref. [63,86] in Fig. 5.4. While the low x behavior of our parameterization is similar to that of Ref. [63,86], our fit is somewhat better constrained at high x. It is interesting to note that all analyses predict that the proton structure function crosses zero between $x = 0.001$ and $x = 0.01$ (at $Q^2 = 5$ GeV^2). This is due to the

[7] We also relax the positivity constraints Eq. (5.22).

sea and gluon contributions that start to dominate at sufficiently low x. Since the neutron structure function g_1^n is large and negative, the deuteron structure function g_1^d is expected to cross zero near $x = 0.01$. If this is true, the effect could potentially be observed by E155.[48]

The values of the first moments of parton distributions, as well as the first moments of structure functions at $Q^2 = 5$ GeV^2, are given in Table 5.4. We observe that the first moments of the valence quark distributions are determined fairly well and the moments of the sea quarks and gluons are only qualitatively constrained. One may note an apparent $\approx 1.9\sigma$ disagreement of Δq_3 with the value extracted from the neutron beta-decay[20] $\Delta q_3 = g_A = 1.2601 \pm 0.0025$. This is due to the fact that the calculation is done in NLO and thus the higher order corrections to the Bjorken sum rule are not taken into account. The corrections can be as big as 5%[28] at the weighted world average $Q^2 \approx 5$ GeV^2 and they would bring Δq_3 in better agreement with the beta decay data. For consistency with the NLO approximation, we do not include this correction; it has no effect on the physical observable g_1.

The contribution of the experimental systematic errors to the errors on the first moments of the parton distributions is comparable to the statistical contribution. Due to that, the full error on the first moment of the gluon distribution ΔG is bigger than quoted in Ref. [63] despite the fact that the new data from E154 were added. This illustrates the importance of the experimental systematic errors which were (incorrectly) assumed to be uncorrelated from point to point in Ref. [63]. The gluon distribution is constrained entirely by the evolution of the polarized structure functions, and no single experiment covers significantly broad kinematic range. Therefore, changes in relative normalization of the experiments (*i.e.* systematic errors) smear out evolution effects and impair the determination of the gluon polarization density. The theoretical uncertainty is also quite large; it could potentially be reduced if the simultaneous analysis of the unpolarized and polarized

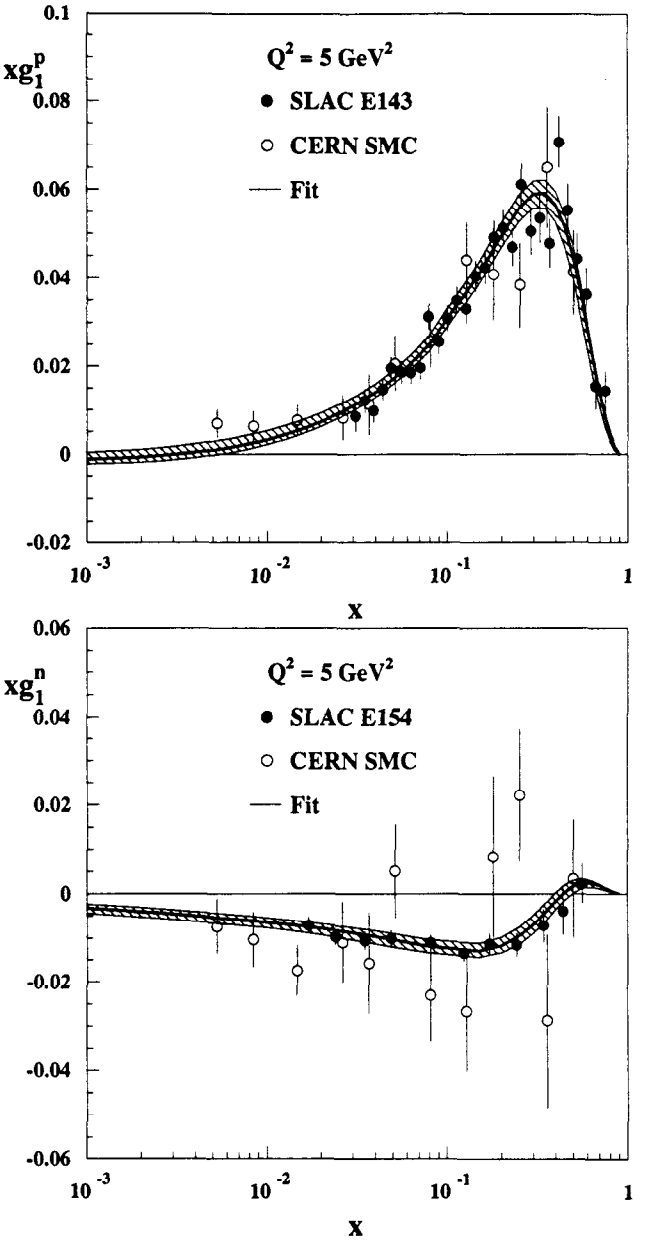

Fig. 5.3. The structure functions (top) xg_1^p and (bottom) xg_1^n at $Q^2 = 5$ GeV^2. E143, SMC, and E154 data have been evolved to $Q^2 = 5$ GeV^2 using a procedure described in the text. The result of the $\overline{\text{MS}}$ fit is shown by the solid line and the hatched area represents the total error of the fit.

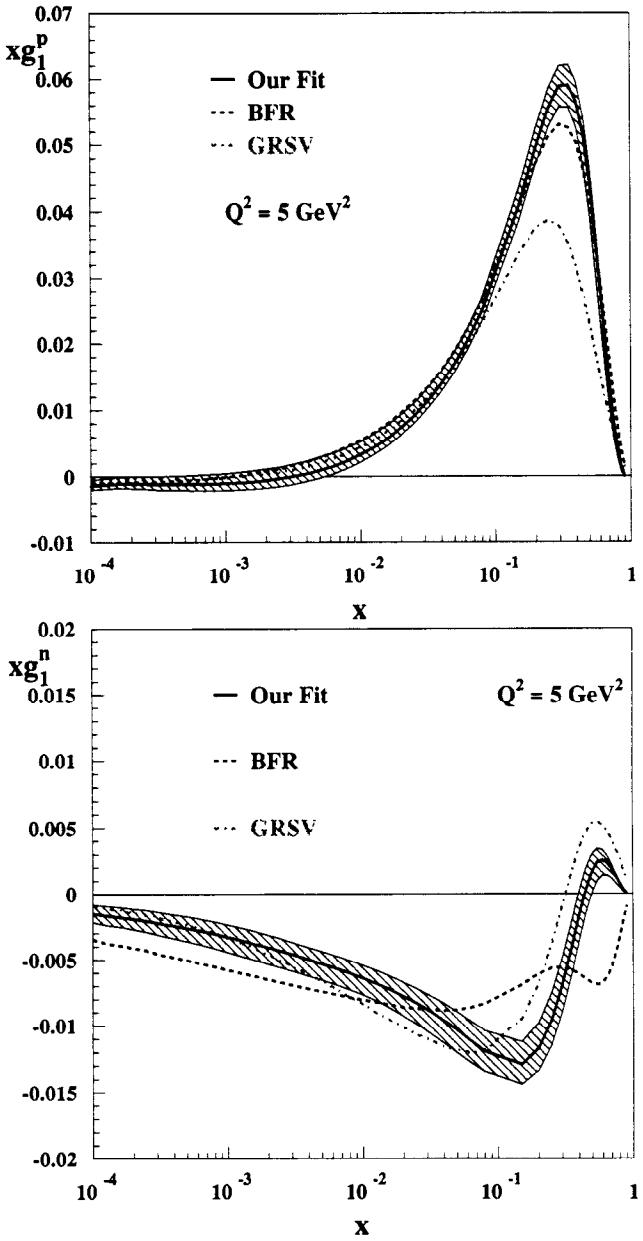

Fig. 5.4. The results of our fit for the structure functions (a) xg_1^p and (b) xg_1^n are compared to the parameterizations of Ref. [63,86] at $Q^2 = 5$ GeV^2. The AB parameterization of Ref. [63,158] is shown as dashed lines, and the "standard" NLO set of Ref. [86,159] is shown by dot-dashed lines. The result of our $\overline{\text{MS}}$ fit is shown by the solid line and the hatched area represents the total error of the fit.

Table 5.4. First moments of the polarized parton distributions and structure functions of the proton, neutron, and deuteron in $\overline{\text{MS}}$ and AB schemes evaluated at $Q^2 = 5$ GeV^2. Errors are statistical, systematic, and theoretical.

	$\overline{\text{MS}}$				AB			
	Value	Stat.	Syst.	Theory	Value	Stat.	Syst.	Theory
Δu_V	0.69	$^{+0.02}_{-0.02}$	$^{+0.05}_{-0.04}$	$^{+0.14}_{-0.01}$	0.74	$^{+0.02}_{-0.03}$	$^{+0.02}_{-0.03}$	$^{+0.07}_{-0.01}$
Δd_V	−0.40	$^{+0.04}_{-0.04}$	$^{+0.03}_{-0.03}$	$^{+0.07}_{-0.00}$	−0.33	$^{+0.03}_{-0.04}$	$^{+0.03}_{-0.05}$	$^{+0.01}_{-0.03}$
$\Delta \bar{Q}$	−0.02	$^{+0.01}_{-0.02}$	$^{+0.01}_{-0.01}$	$^{+0.00}_{-0.03}$	−0.03	$^{+0.02}_{-0.02}$	$^{+0.01}_{-0.01}$	$^{+0.01}_{-0.01}$
ΔG	1.6	$^{+0.7}_{-0.7}$	$^{+0.3}_{-0.6}$	$^{+0.1}_{-0.6}$	0.4	$^{+1.0}_{-0.6}$	$^{+0.9}_{-0.6}$	$^{+1.1}_{-0.1}$
Δq_3	1.09	$^{+0.03}_{-0.02}$	$^{+0.06}_{-0.05}$	$^{+0.06}_{-0.01}$	1.07	$^{+0.03}_{-0.02}$	$^{+0.05}_{-0.06}$	$^{+0.10}_{-0.01}$
Δq_8	0.30	$^{+0.06}_{-0.05}$	$^{+0.06}_{-0.04}$	$^{+0.23}_{-0.01}$	0.41	$^{+0.05}_{-0.08}$	$^{+0.02}_{-0.06}$	$^{+0.03}_{-0.01}$
$\Delta \Sigma$	0.22	$^{+0.05}_{-0.06}$	$^{+0.04}_{-0.05}$	$^{+0.01}_{-0.01}$	0.26	$^{+0.07}_{-0.07}$	$^{+0.06}_{-0.06}$	$^{+0.05}_{-0.02}$
Γ_1^p	0.115	$^{+0.006}_{-0.006}$	$^{+0.008}_{-0.008}$	$^{+0.009}_{-0.001}$	0.114	$^{+0.005}_{-0.006}$	$^{+0.008}_{-0.011}$	$^{+0.001}_{-0.003}$
Γ_1^n	−0.054	$^{+0.005}_{-0.007}$	$^{+0.005}_{-0.006}$	$^{+0.002}_{-0.001}$	−0.051	$^{+0.005}_{-0.007}$	$^{+0.006}_{-0.007}$	$^{+0.001}_{-0.012}$
Γ_1^d	0.028	$^{+0.005}_{-0.006}$	$^{+0.005}_{-0.005}$	$^{+0.005}_{-0.001}$	0.029	$^{+0.005}_{-0.006}$	$^{+0.006}_{-0.007}$	$^{+0.001}_{-0.007}$
Γ_1^{p-n}	0.169	$^{+0.005}_{-0.004}$	$^{+0.009}_{-0.008}$	$^{+0.007}_{-0.001}$	0.165	$^{+0.004}_{-0.004}$	$^{+0.007}_{-0.009}$	$^{+0.013}_{-0.001}$

data was performed (including α_S as one of the parameters). The uncertainties on the values of $\Delta\Sigma$ are larger than originally estimated[30,82] due to the uncertainty in the evolution effects and low-x extrapolation embedded in our analysis.

The results of the fits in both $\overline{\rm MS}$ and AB schemes are consistent within errors. The fits are significantly less stable in the AB scheme. Note that the values of the singlet axial charge ($a_0 = \Delta\Sigma$ in $\overline{\rm MS}$ scheme and $a_0 = \Delta\Sigma - N_f\alpha_S\Delta G/(2\pi)$ in AB scheme) are almost exactly the same in two schemes.

Using the parameterization of the parton distributions, one can obtain the polarized structure function (Eq. (5.1)) and evolve the experimental data points to a common $\langle Q^2\rangle$ using the formula:

$$g_1^{\rm exp}(x_i,\langle Q^2\rangle) = g_1^{\rm exp}(x_i,Q_i^2) - \Delta g_1^{\rm fit}(x_i,Q_i^2,\langle Q^2\rangle) \tag{5.24}$$

with

$$\Delta g_1^{\rm fit}(x_i,Q_i^2,\langle Q^2\rangle) = g_1^{\rm fit}(x_i,Q_i^2) - g_1^{\rm fit}(x_i,\langle Q^2\rangle)\ , \tag{5.25}$$

where $g_1^{\rm exp}(x_i,Q_i^2)$ is the structure function measured at the experimental kinematics, and $g_1^{\rm fit}$ is the fitted value. The errors on $g_1^{\rm exp}(x_i,\langle Q^2\rangle)$ have three sources:

$$\sigma^2(g_1^{\rm exp}(x_i,\langle Q^2\rangle)) = \sigma^2(g_1^{\rm exp})_{\rm stat.} + \sigma^2(g_1^{\rm exp})_{\rm syst.} + \sigma^2(g_1)_{\rm evol.}\ , \tag{5.26}$$

where statistical and systematic uncertainties should take into account the correlation between $g_1^{\rm exp}(x_i,Q_i^2)$ and $g_1^{\rm fit}$, and the evolution uncertainty includes only uncorrelated experimental uncertainties as well as theoretical uncertainties added in quadrature. Table 5.5 lists the E154 data points evolved to the common $\langle Q^2\rangle = 5$ GeV^2 using this procedure. For comparison, we have included the values of $g_1^n(5\ {\rm GeV}^2)$ obtained assuming that the ratio g_1/F_1 is independent of Q^2, as has been traditionally done (*cf.* Table 4.4). The difference between the NLO QCD evolution and the naive assumption is comparable to the precision of the present-day experiments and cannot be neglected.

Table 5.5. E154 results on g_1^n evolved to $\langle Q^2 \rangle = 5$ GeV^2 assuming g_1/F_1 is independent of Q^2 and according to Eq. (5.24). Errors were propagated as described in the text.

x_i	Q_i^2 GeV^2	$g_1^n(x_i, Q_i^2) \cdot \frac{F_1^n(x_i, 5\ \mathrm{GeV}^2)}{F_1^n(x_i, Q_i^2)}$ ±stat.±syst.	$g_1^n(x_i, 5\ \mathrm{GeV}^2)$ ±stat.±syst.±evol.
		2.75° spectrometer	
0.017	1.21	$-0.497 \pm 0.163 \pm 0.147$	$-0.419 \pm 0.115 \pm 0.104 \pm 0.014$
0.024	1.59	$-0.481 \pm 0.092 \pm 0.079$	$-0.409 \pm 0.071 \pm 0.062 \pm 0.006$
0.035	2.05	$-0.345 \pm 0.073 \pm 0.044$	$-0.304 \pm 0.061 \pm 0.037 \pm 0.005$
0.049	2.57	$-0.237 \pm 0.046 \pm 0.024$	$-0.215 \pm 0.041 \pm 0.021 \pm 0.004$
0.078	3.32	$-0.127 \pm 0.033 \pm 0.014$	$-0.117 \pm 0.031 \pm 0.013 \pm 0.002$
0.123	4.09	$-0.077 \pm 0.031 \pm 0.009$	$-0.073 \pm 0.030 \pm 0.009 \pm 0.001$
0.173	4.63	$-0.071 \pm 0.033 \pm 0.009$	$-0.069 \pm 0.033 \pm 0.009 \pm 0.001$
0.241	5.09	$-0.053 \pm 0.028 \pm 0.007$	$-0.053 \pm 0.028 \pm 0.007 \pm 0.000$
0.340	5.51	$0.002 \pm 0.037 \pm 0.004$	$0.001 \pm 0.036 \pm 0.004 \pm 0.000$
0.423	5.82	$0.028 \pm 0.061 \pm 0.008$	$0.027 \pm 0.059 \pm 0.007 \pm 0.000$
		5.5° Spectrometer	
0.057	4.03	$0.233 \pm 0.297 \pm 0.037$	$0.224 \pm 0.285 \pm 0.035 \pm 0.001$
0.084	5.47	$-0.150 \pm 0.029 \pm 0.019$	$-0.152 \pm 0.029 \pm 0.019 \pm 0.001$
0.123	7.23	$-0.113 \pm 0.016 \pm 0.012$	$-0.121 \pm 0.017 \pm 0.012 \pm 0.002$
0.172	8.94	$-0.058 \pm 0.015 \pm 0.007$	$-0.065 \pm 0.016 \pm 0.007 \pm 0.003$
0.242	10.71	$-0.041 \pm 0.012 \pm 0.005$	$-0.047 \pm 0.012 \pm 0.005 \pm 0.003$
0.342	12.55	$-0.021 \pm 0.013 \pm 0.005$	$-0.023 \pm 0.012 \pm 0.005 \pm 0.001$
0.442	13.83	$-0.011 \pm 0.014 \pm 0.003$	$-0.011 \pm 0.012 \pm 0.002 \pm 0.001$
0.564	15.00	$0.005 \pm 0.012 \pm 0.002$	$0.004 \pm 0.008 \pm 0.001 \pm 0.000$

The Q^2 dependence of the ratio g_1/F_1 for the proton and neutron is shown for several x bins in Fig. 5.5. For the neutron, the evolution if g_1^n is slower than that of F_1^n. Therefore, assuming scaling of g_1^n/F_1^n, one typically overestimates the absolute value of $g_1^n(x, \langle Q^2 \rangle)$ at low x (where $Q_i^2 < \langle Q^2 \rangle$), and underestimates it at high x (where $Q_i^2 > \langle Q^2 \rangle$). The two effects approximately cancel for the integral over the measured range in case of E154. However, the shape of the structure function at low x affects the extrapolation to $x = 0$ (the effective low x power decreases, see below). The effect of the perturbative evolution is qualitatively the same for the proton.

The data on g_1^n at $Q^2 = 5$ GeV^2 averaged between two spectrometers are given in Table 5.6. For the integral of the neutron structure function in the measured

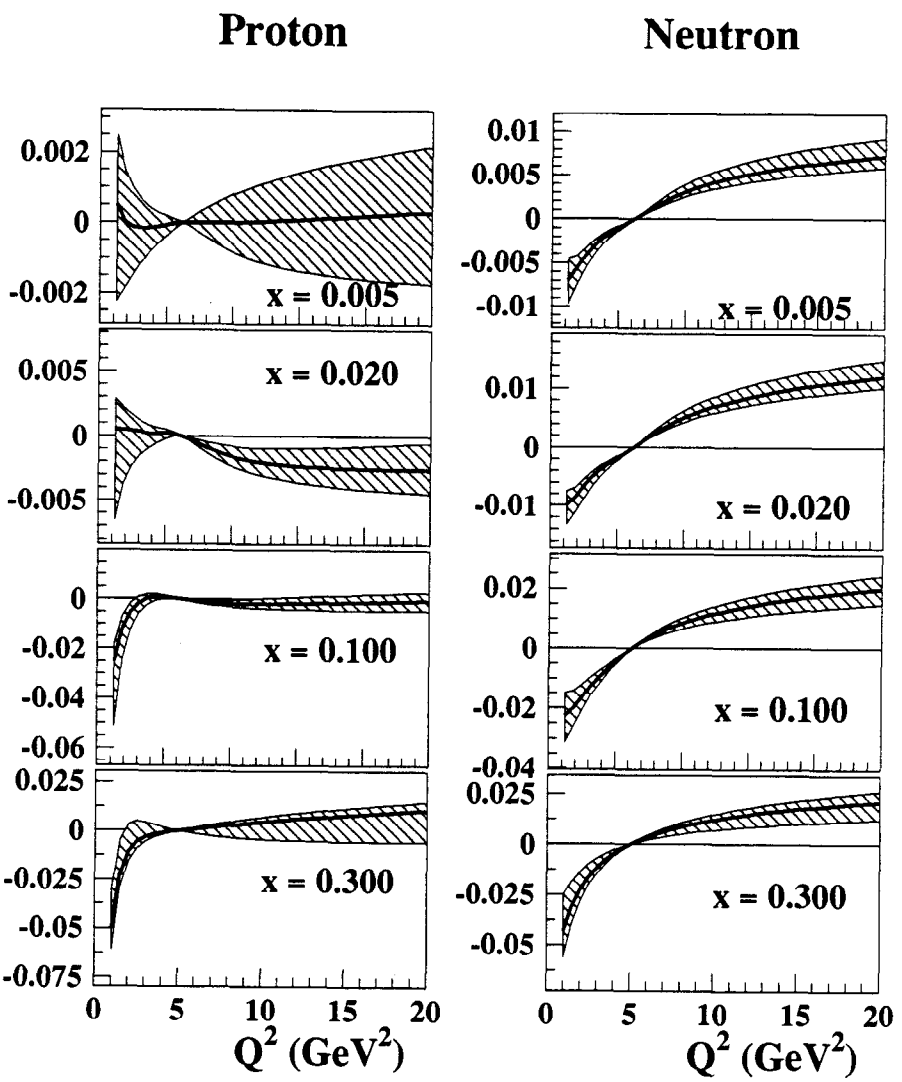

Fig. 5.5. Evolution of the ratios g_1/F_1 for proton (left) and neutron (right). Plotted is the difference $\frac{g_1}{F_1}(x, Q^2) - \frac{g_1}{F_1}(x, 5\ \mathrm{GeV}^2)$. $\overline{\mathrm{MS}}$ fit is shown in solid and the hatched area represents the total (experimental and theoretical) uncertainty.

Table 5.6. E154 results on g_1^n evolved to $Q^2 = 5$ GeV^2 according to the NLO DGLAP equations. The data of the two spectrometers have been averaged.

x	$g_1^n(x, 5\ \text{GeV}^2) \pm$ stat. $\pm$ syst. $\pm$ evol.
0.017	$-0.419 \pm 0.115 \pm 0.104 \pm 0.014$
0.024	$-0.409 \pm 0.071 \pm 0.062 \pm 0.006$
0.035	$-0.304 \pm 0.061 \pm 0.037 \pm 0.005$
0.049	$-0.206 \pm 0.041 \pm 0.021 \pm 0.004$
0.081	$-0.136 \pm 0.021 \pm 0.016 \pm 0.001$
0.123	$-0.109 \pm 0.015 \pm 0.011 \pm 0.002$
0.172	$-0.066 \pm 0.014 \pm 0.007 \pm 0.003$
0.242	$-0.048 \pm 0.011 \pm 0.005 \pm 0.003$
0.342	$-0.021 \pm 0.011 \pm 0.005 \pm 0.001$
0.441	$-0.009 \pm 0.012 \pm 0.002 \pm 0.001$
0.564	$0.004 \pm 0.008 \pm 0.001 \pm 0.000$

range, we obtain

$$\int_{0.0135}^{0.7} dx\ g_1^n(x) = -0.035 \pm 0.003 \pm 0.005 \pm 0.001\ , \tag{5.27}$$

where the first error is statistical, the second is systematic, and the third is due to the uncertainty in the evolution. This value agrees well with the originally quoted number (*cf.* Eq. (4.2)).

5.6 Low x extrapolation updated

It is interesting to note that the low-x behavior of the valence distributions is reasonably convergent ($\Delta u_V(x) \sim x^{0.18^{+0.37}_{-0.10}}$ and $\Delta d_V(x) \sim x^{-0.43^{+0.77}_{-0.12}}$ as $x \to 0$), and is consistent with the Regge predictions[65] at low $Q^2 \approx Q_0^2 = 0.34$ GeV^2. In the singlet sector, the data seem to prefer small values of α_Q, and the uncertainties on α_Q and α_G are large. The reason for that is that the data are not yet sensitive enough to the true asymptotic behavior of the sea and gluon distributions at low x. The parameters α_Q and α_G should be viewed as effective powers obtained in the range $x \approx 0.005 - 0.1$ (compared to the unpolarized case where the measurements extend down to $x \approx 10^{-5}$). At higher $Q^2 = Q^2_{\text{data}} > 1$ GeV$^2 > Q_0^2$, the perturbative

Table 5.7. Results of the fits to the low x data of E154, evolved to $Q^2 = 5$ GeV^2 according to Eq. (5.24). The first uncertainty is statistical, the second is systematic, and the third is due to evolution.

Fit	$g_1^n = C$	$g_1^n = Cx^{-\alpha}$
Points	3	5
C	$-0.36 \pm 0.04 \pm 0.06 \pm 0.01$	$-0.018 \pm 0.008 \pm 0.001 \pm 0.001$
α		$0.81 \pm 0.15 \pm 0.06 \pm 0.01$
$\int_0^{0.0135} dx\ g_1^n$	$-0.005 \pm 0.001 \pm 0.001 \pm 0.000$	$-0.042 \pm 0.063 \pm 0.016 \pm 0.004$
$\int_0^1 dx\ g_1^n$	$-0.040 \pm 0.004 \pm 0.006 \pm 0.001$	$-0.077 \pm 0.063 \pm 0.021 \pm 0.005$

evolution leads to a divergent behavior of the valence distributions and amplifies the divergent behavior of the sea and gluon distributions,[71] which is evident in the neutron structure function below $x = 0.1$ (see Chapter 4). The low x behavior of the singlet distributions is to a large extent decoupled from the distributions at the low initial scale; it is determined primarily by evolution. This makes the data at high Q^2 even less sensitive to the initial shape of the sea and gluon distributions.

It is interesting to compare the low x extrapolation done with the E154 data evolved according to the NLO DGLAP equations with the results presented in Section 4.4.3 (where the data have been evolved to $Q^2 = 5$ GeV^2 assuming the scaling of g_1^n/F_1^n). Results of the two fits are summarized in Table 5.7: the "Regge" fit $g_1^n = const$, and a "free power" fit. Again, although the behavior of the free-power fit is now slightly softer and it is (barely) integrable within one standard deviation, two fits give quite different values of the total integral of the neutron structure function.

One should note that the convergent behavior of the structure functions at low x and high Q^2 would be incompatible with the pQCD predictions.[160,161] In fact, at next-to-leading order, the polarized parton distributions, and therefore g_1, are expected to rise faster than any power of $\log(1/x)$ (but slower than any power of x) even if the initial distributions at low scale are convergent. At sufficiency low

x (and/or high enough Q^2), the singlet distributions start to dominate, and both proton and neutron structure functions have the same asymptotic behavior. This can be seen in Fig. 5.6 where we plotted the structure functions of proton and neutron at $Q^2 = 5$ GeV^2 and $x = 10^{-4} - 10^{-1}$. In addition to the $\overline{\text{MS}}$ parameterization discussed in this Chapter, we show the behavior of the structure functions for the cases where we fix the low x power of all polarized distributions to 0 or 1 at the initial scale $Q^2 = 0.34$ GeV^2. Evidently, the asymptotic behavior for both proton and neutron is the same in all cases (Fig. 5.6, top); the structure functions are insensitive to the shape of the initial distributions below $x = 0.001$. The initial distributions, however, dictate at what values of x and Q^2 the low x behavior sets in. Thus, for the neutron, the region is between $x = 0.01$ (for soft initial distributions) and $x = 0.1$ (for our fit), but for the proton the asymptotic behavior sets in near $x = 10^{-4}$ (Fig. 5.6, bottom). Therefore, extrapolating the present proton data (limited to $x > 0.005$) at moderate Q^2 could be problematic.

To evaluate the integrals of the neutron and proton structure functions, we evolve the E154 neutron data and the E143 proton data[10] to $Q^2 = 5$ GeV^2 according to the procedure discussed above. The contributions to the integrals over the range measured by these experiments are summarized in Table 5.8. Using the $\overline{\text{MS}}$ parameterization of Table 5.2, we have also evaluated the contributions to the first moments of g_1^n and g_1^p from unmeasured regions (high and low x) and obtained for the Bjorken sum

$$\Gamma_1^{p-n}(5\text{ GeV}^2) = \int_0^1 dx\ (g_1^p - g_1^n) = 0.172 \pm 0.004(\text{stat.}) \pm 0.010(\text{syst.}) \pm 0.007(\text{evol.}) \tag{5.28}$$

in agreement with the $O(\alpha_S^3)$[28] prediction 0.186 evaluated with $\alpha_S(M_Z^2) = 0.109$. This number agrees very well with the value in Table 5.4 obtained by direct integration of the parton densities. The result is fairly insensitive to the details of the low-x extrapolation which for the difference $[g_1^p - g_1^n](x)$ is determined by the valence

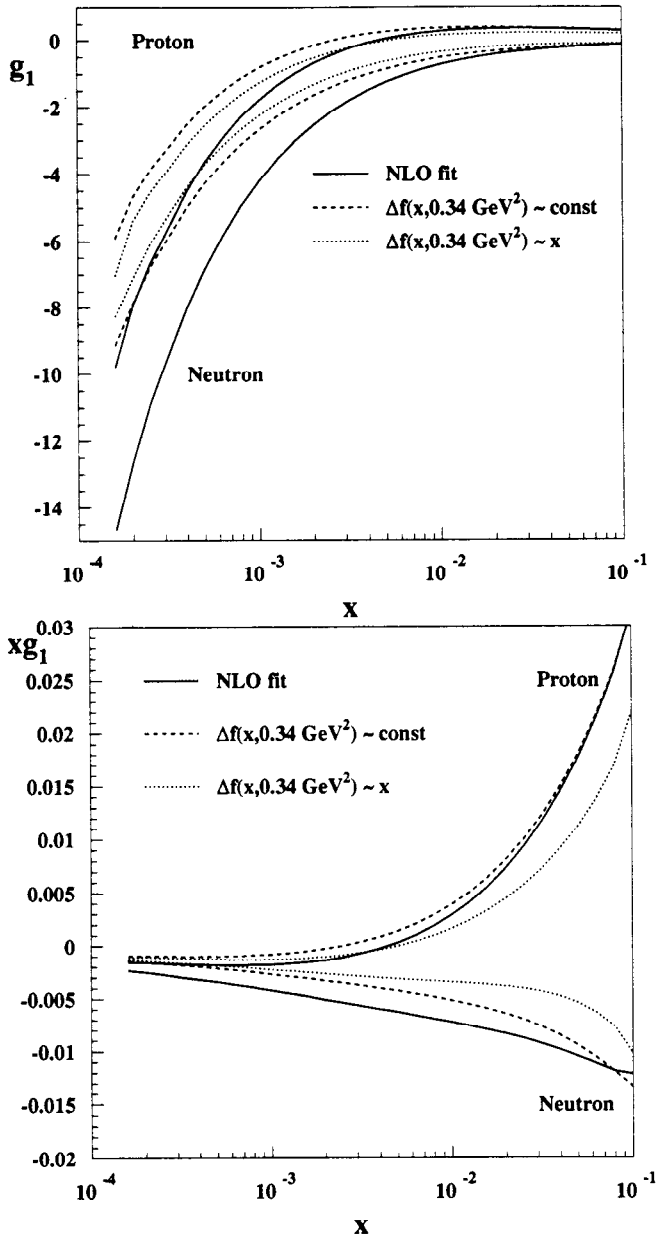

Fig. 5.6. The low x behavior of the structure functions g_1^p and g_1^n (top) and xg_1^p and xg_1^n (bottom) for different choices of the initial parton distributions. The result of the $\overline{\text{MS}}$ fit (Table 5.2) are plotted in solid, and parameterizations with constrained low x behavior $\Delta f \sim const$ and $\Delta f \sim x$ are shown as dashed and dotted lines, respectively.

Table 5.8. Integrals of the proton and neutron polarized structure functions evaluated at $Q^2 = 5$ GeV^2. The first error is statistical, the second is systematic, and third is due to evolution.

	E154 (g_1^n)	E143 (g_1^p)
$x_{\min}$	0.014	0.029
$x_{\max}$	0.7	0.8
$\int_{x_{\min}}^{x_{\max}}$	$-0.035 \pm 0.003 \pm 0.005 \pm 0.001$	$0.113 \pm 0.003 \pm 0.007 \pm 0.001$
$\int_0^{x_{\min}} + \int_{x_{\max}}^1$	$-0.018 \pm 0.002 \pm 0.002 \pm 0.005$	$0.005 \pm 0.003 \pm 0.002 \pm 0.009$
$\int_0^1$	$-0.053 \pm 0.004 \pm 0.007 \pm 0.006$	$0.119 \pm 0.005 \pm 0.009 \pm 0.010$

quark distributions, and is well constrained by the data. The low x behavior in the non-singlet polarized sector is also relatively insensitive to the higher-order corrections.[162] On the other hand, the low-x extrapolation of the proton and neutron integrals alone still relies on the assumption that the asymptotic behavior of sea quark and gluon distributions can be determined from the present data, and that the effects of higher-order resummations are small. These assumptions, and therefore evaluation of the total quark helicity $\Delta\Sigma$, are on potentially weaker grounds. Precise higher energy data on the polarized structure functions of both proton and neutron are required to determine this quantity.

CHAPTER 6

CONCLUSIONS AND OUTLOOK

Spin-dependent deep inelastic scattering still remains one of the most fascinating fields of particle physics. New experimental data, such as the results presented in this dissertation, increase our knowledge and understanding of the structure of the proton and neutron. At the same time, as we get a closer look into the structure and dynamics of quarks and gluons inside the nucleon, new questions arise, some of our naive expectations fall, and our uncertainty grows. The results of this experiment is one example of such *evolution* of knowledge that probably is inevitable, as was postulated seventy years ago by Heisenberg.

The results of the experiment E154 at SLAC, described in this dissertation, is the most precise determination of the spin dependent structure function g_1^n of the neutron. Compared to the previous SLAC spin structure experiments, the kinematic coverage was significantly increased. The increased beam energy allowed us to extend the measurements to lower values of Bjorken variable x and to increase the four-momentum transfer Q^2, providing for a possibility to constrain the evolution of the polarized parton distributions. Thus, not only the information about the quark contribution to the structure functions can be obtained from the present data, but also first constraints on the gluon helicity distribution are emerging.

At the same time, the data presented us with some surprises. We have observed relatively large values of g_1^n at low x, and the behavior of the structure function seems to be quite divergent. This apparently disagrees with predictions of the conventional Regge theory, and poses certain problems for extrapolating the data to $x = 0$ in order to evaluate the first moment of g_1^n and test the Ellis-Jaffe sum rule. While

such a behavior is qualitatively understood in perturbative QCD, firm quantitative predictions are not yet available.

In order to reduce the ambiguity in the interpretation of the results, we have performed a Next-to-Leading Order QCD analysis of the world data on polarized deep inelastic scattering. Careful attention has been paid to the uncertainties involved, both experimental and theoretical. We find that the data constrain the first moments of the polarized valence quark distributions; the polarized gluon and sea quark distributions can only be qualitatively constrained. We determine the Q^2 dependence of the ratio g_1/F_1 for the proton and neutron and find that it is significant compared to the present experimental errors. Assuming the validity of the NLO approximation, we determine the first moments of the spin dependent structure functions of the proton and neutron, and find agreement with the Bjorken sum rule. However, for an unambiguous determination of the total quark helicity and the polarized gluon distribution, data at the higher energies are needed.

The spin structure program will continue, and is likely to bring us more exciting discoveries about the internal structure of the nucleon. At SLAC, the experiment E155[48] will utilize the 50 GeV electron beam and the same detector system as E154 (with an addition of another spectrometer arm at 10.5° relative to the beam line). Using ammonia and ^{6}LiD targets similar to the targets used in E143, the experimenters will measure the spin dependent structure functions of the proton and deuteron over the same x range as E154, and with increased (due to the new spectrometer) Q^2 coverage. This precision data, especially on the deuteron structure function, will be of great use for understanding the nucleon spin structure at low x.

In Europe, the HERMES experiment[80] at DESY is continuing to collect data. The first preliminary results from the 1995 run with the polarized ^{3}He target on the neutron spin structure function were released last summer, and are expected to be published soon. The studies of the *semi-inclusive* reactions (in which the flavor

of the leading hadron is tagged) allow one to probe directly the valence and sea quark distributions inside the nucleon. The future of HERMES looks very promising, and it should continue to run into the next century. The SMC experiment[12,13] at CERN has finished taking data in 1996. The results of the 1995 deuteron run will be published soon, and the proton 1996 results are expected to be released this year.

In the 21st century, the style of the spin structure experiments will change. The HERMES experiment is likely to be the last in the generation of the "traditional" inclusive lepton-nucleon DIS experiments. A lot of attention has been devoted recently to the problem of polarizing proton beams. Such beams are planned for the RHIC collider at BNL, for the UNK at Serpukhov, Russia, and are proposed for the Fermilab Main Injector and HERA at DESY. Having polarized protons in the HERA ring would be particularly interesting since one would be able to extend the kinematic range of the polarized deep-inelastic scattering experiments to $x \approx 10^{-5}$ and $Q^2 \approx 10^4$ GeV^2, similar to the unpolarized scattering. A complementary DIS fixed target program would be possible at the Next Linear Collider (NLC). This would allow for precise determination of the behavior of the spin structure functions at low x. A perturbative QCD analysis of such data, similar to the NLO analysis described in Chapter 5, would determine the spin dependent parton distributions, including that of the gluon, with a precision comparable to the present unpolarized analyses. At the proton machines, the studies of the nuclear spin structure are planned by measuring the single- and double-spin asymmetries in the Drell-Yan muon pair production $pp \to \mu^+\mu^- X$ that at low energies (UNK and Fermilab fixed target experiments) are sensitive to the polarization of the sea quarks, and at higher energies probe the gluon helicity distributions. Another good measure of the gluon polarization is the asymmetry in the hard photon production which probes the process $g^*q \to q\gamma$. The asymmetry in the open charm lepto- or photo-production is

also sensitive to the gluon polarization. Such experiments are proposed at SLAC and CERN.

There is still a lot to learn about the internal spin structure of the nucleon. Future experimental program promises to be very exciting, and the author will follow the developments in the field with great interest.

APPENDIX A

LIGHT-CONE PERTURBATION THEORY

One of the most convenient frameworks to explore the properties of hadronic structure at large momentum transfers is the time-ordered perturbation theory, or, equivalently, perturbation theory on the light cone with time variable $\tau = t + z/c$.[45,46] Let us define

$$p^{\pm} \equiv p^0 \pm p^3 \tag{A.1}$$

and

$$p^{\mu} = (p^+, p^-, \vec{p}_{\perp}). \tag{A.2}$$

The mass-shell condition is, obviously,

$$p^+ p^- - \vec{p}_{\perp}{}^2 = p^2 = m^2. \tag{A.3}$$

The light-cone energy $p^- > 0$ and then $p^+ > 0$; therefore, there are no vacuum-creation graphs (Fig. A.1). The Fock expansion constructed on the vacuum state provides a complete relativistic many-particle basis; for a hadronic wave function we can write

$$|\Psi_H\rangle = \sum_n |n\rangle \psi_n(x_i, k_{\perp i}, \lambda_i), \tag{A.4}$$

where $|n\rangle = |qqq\rangle, |qqqg\rangle \ldots$ for baryons ($|n\rangle = |q\bar{q}\rangle, |q\bar{q}g\rangle \ldots$ for mesons), and $\psi_n(x_i, k_{\perp i}, \lambda_i)$ is a Lorenz-frame independent wave function for a state with n on-

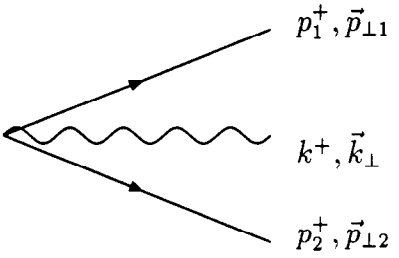

Fig. A.1. Vacuum creation graphs vanish in light-cone perturbation theory.

mass-shell constituents, and λ is the polarization index. The 4-momentum for each constituent has been parameterized as

$$k_i^\mu \equiv (k_i^+, k_i^-, \vec{k}_{\perp i}) = (x_i p^+, \frac{\vec{k}_\perp^2 + m^2}{x p^+}, \vec{k}_\perp). \tag{A.5}$$

Momentum conservation requires

$$\sum_{i=1}^{n} x_i = 1 \quad \sum_{i=1}^{n} \vec{k}_{\perp i} = 0. \tag{A.6}$$

Moreover, since $p^+ > 0$ and $k_i^+ > 0$, $x_i > 0$.

The Feynman rules for light-cone perturbation theory can be found in Ref. [46]. We will repeat some of the particularly important ones:

1. Assign a momentum k^μ to each line so that

   (a) k^+ and $\vec{k}_\perp$ are conserved at each vertex

   (b) $k^2 = m^2$, or $k^- = (\vec{k}_\perp^2 + m^2)/k^+$.

2. Include a factor $\theta(k^+)/k^+$ for each fermion, anti-fermion, or scalar. For vector bosons, assign the factor $d_{\mu\nu}\theta(k^+)/k^+$ where $d_{\mu\nu}$ is the (gauge-dependent) polarization sum. In the Feynman gauge $d_{\mu\nu} = -g_{\mu\nu}$. In the axial gauge ($\eta \cdot A = 0$ where η is an arbitrary fixed 4-vector)

$$d_{\mu\nu}(k) = \sum_{\lambda=1,2} \epsilon_\mu(k,\lambda)\epsilon_\nu(k,\lambda)$$

$$= -g_{\mu\nu} + \frac{\eta_\mu k_\nu + \eta_\nu k_\mu}{\eta \cdot k} \tag{A.7}$$

where $\eta \cdot \epsilon = k \cdot \epsilon = 0$. The light-cone gauge where $\nu = (0, 2, \vec{0}_\perp)$ is particularly convenient.

3. The gluon(photon)-fermion vertices are

$$e_0 \bar{u}\gamma^\mu u,\ e_0 \bar{u}\gamma^\mu v,\ -e_0 \bar{u}\gamma^\mu v,\ -e_0 \bar{v}\gamma^\mu v\ . \tag{A.8}$$

4. For each intermediate state there is a factor

$$\frac{1}{\sum_{\text{inc}} k^- - \sum_{\text{interm}} k^- + i\epsilon} \tag{A.9}$$

where the summation is over the light-cone energies of the incoming and intermediate particles. This factor is a measure of virtuality of the intermediate state (although each particle is assumed on-shell). Thus, for a Fock state with one of the constituents having $x \sim 1$, the denominator becomes

$$\frac{1}{p^+}\left[M^2 - \sum_{i=1}^{n} \frac{\vec{k}_{\perp i}^2 + m_i^2}{x_i}\right] \sim O(\frac{\vec{k}_\perp^2 + m^2}{1-x}) \to \infty, \tag{A.10}$$

and the state is said to be far off-shell.

5. Integrate $\int dk^+ \int d^2\vec{k}_\perp / 16\pi^3$ for each independent k and sum over internal spins and polarizations.

The distribution functions $G_{q/H}(x, \lambda, Q)$ can be calculated from the overlaps of the light-cone wave functions

$$G_{q/H}(x, \lambda, Q) = \sum_n \int^{k_\perp^2 < Q^2} \pi d^2\vec{k}_{\perp i} dx_i |\psi_n^\lambda(x_i, \vec{k}_{\perp i}, \lambda_i)|^2 \delta(x - x_q)\ , \tag{A.11}$$

where the summation is over all relevant Fock states. The asymptotic behavior of the light-cone wave functions is obtained by iterating the interaction kernel.[40] Thus, for $q\bar{q}$ mesonic states the diagram of Fig. A.2 yields:

$$\psi(x, \vec{k}_\perp) = \frac{1}{M^2 - \frac{\vec{k}_\perp^2 + m^2}{x(1-x)}} \int d^2 l_\perp V(x, \vec{k}_\perp; y, \vec{l}_\perp)\psi(y, \vec{l}_\perp) \overset{x\to 1}{\sim} (1-x), \tag{A.12}$$

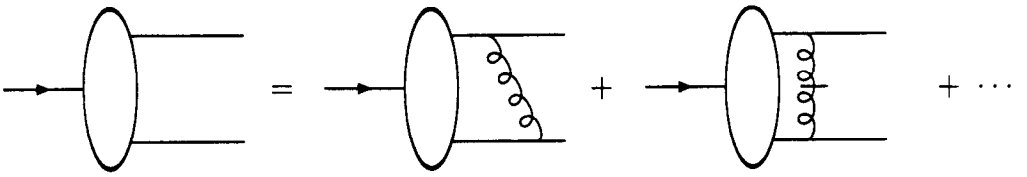

Fig. A.2. Calculation of the mesonic light-cone wave function. The second term is the instantaneous part of the gluon propagator.

where the integration represents the transition from the initial configuration with quark momentum $k_0 = (yp^+, (\vec{l}_\perp^2 + m^2)/yp^+, \vec{l}_\perp)$ and is of order α_s. The end-point $x \sim 1$ behavior of the mesonic distribution amplitude is then

$$G_{q/M}(x) \sim (1-x)^2. \tag{A.13}$$

Similarly, the leading end-point behavior of the quark distribution function $G_{q/p}(x)$ for the proton is computed from the diagram of Fig. A.3:

$$G_{q/p}(x) \sim (1-x)^3. \tag{A.14}$$

The contribution of Fig. A.4 is suppressed by two orders of $(1-x)$. It is interesting to note that the diagram of Fig. A.3 only contributes if the spectator quarks with momenta y_2 and y_3 have opposite helicities.[40] At high x it translates into the requirement that the helicity of the struck quark be aligned with the proton helicity. If it is anti-aligned, the leading behavior is

$$G_{q\downarrow/p\uparrow}(x) \sim (1-x)^5. \tag{A.15}$$

This fact illustrates the helicity retention property of the gauge interactions. Equations (A.13), (A.14), and (A.15) are the manifestation of the quark counting rules.[47]

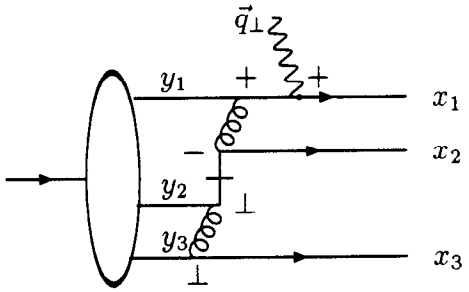

Fig. A.3. The leading contribution to the proton distribution function $G_{q/p}$ at $x \sim 1$. $+$, $-$, and $\perp$ denote the current components. The quark propagator is instantaneous.

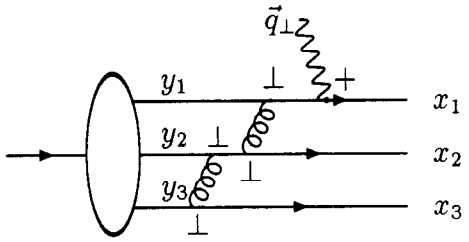

Fig. A.4. $(1-x)^5$ contribution to the proton distribution function.

APPENDIX B

NEXT-TO-LEADING ORDER EVOLUTION OF PARTON DISTRIBUTIONS

The solution of the DGLAP equations in the Mellin n-moment space is significantly simplified. A key feature of the Mellin transform is that the moment of a convolution of two functions is given simply by the product of two moments: if

$$C(x) = (f \otimes g)(x) \equiv \int_x^1 \frac{dz}{z} f\left(\frac{x}{z}\right) g(z) \,, \tag{B.1}$$

the moment is given by

$$C(n) \equiv \int_0^1 dx\ x^{n-1} C(x) = f(n) g(n) \,. \tag{B.2}$$

Thus, complicated integro-differential DGLAP equations are reduced to simple linear equations (or a system of equations in the singlet sector). One typically evolves the parton distributions and calculates the moments of the structure functions in the Mellin space, and then inverts the structure functions into the Bjorken x space. Thus, only one (numerical) integration is required. In Mellin space, the structure functions are given by (*cf.* Eq. (5.1))

$$g_1(n, Q^2) = \frac{1}{2} \sum_q^{N_f} e_q^2 \left[C_q(n) \Delta q(n, Q^2) + \frac{1}{N_f} C_G(n) \Delta G(n, Q^2) \right] \,, \tag{B.3}$$

where

$$\begin{aligned} C_q(n, \alpha_S) &= 1 + \frac{\alpha_S(Q^2)}{2\pi} C_q^{(1)}(n) + \cdots \\ C_G(n, \alpha_S) &= \frac{\alpha_S(Q^2)}{2\pi} C_G^{(1)}(n) + \cdots \end{aligned} \tag{B.4}$$

and the NLO spin dependent Wilson coefficients in $\overline{\text{MS}}$ scheme are given by[37]

$$C_q^{(1)} = C_F \left[-S_2(n) + S_1(n) \left(S_1(n) + \frac{3}{2} - \frac{1}{n(n+1)} \right) + \frac{1}{n^2} + \frac{1}{2n} + \frac{1}{n+1} - \frac{9}{2} \right]$$

$$C_G = 2T_f \left[-\frac{n-1}{n(n+1)} (S_1(n)+1) - \frac{1}{n^2} + \frac{2}{n(n+1)} \right] . \quad \text{(B.5)}$$

Here $C_F = 4/3$ and $T_f = N_f/2$ are Casimir invariants for the quark representation of $SU(3)_{\text{flavor}}$ ($N_f = 3$ is the number of active flavors). The factors $S_k(n)$ will be given below.

Note that in $\overline{\text{MS}}$ scheme the first moment of the gluon coefficient function vanishes $C_G^{(1)}(n = 1) = 0$, the first moment of the quark Wilson coefficient is $C_q^{(1)}(n = 1) = 3C_F/2$, and the first moments of the spin-dependent structure functions are simply given by

$$\Gamma_1(Q^2) = \frac{1}{2} \sum_q e_q^2 \left(1 - \frac{\alpha_S(Q^2)}{\pi} \right) \Delta q(Q^2) . \quad \text{(B.6)}$$

The total gluon density does not couple to the first moment of the structure function g_1 in $\overline{\text{MS}}$ scheme. A transformation to other schemes, in which the gluon contributes to the first moment of g_1 (such as Adler-Bardeen scheme), are given in Chapter 5.

The Q^2 evolution of the parton densities is governed by the the anomalous dimensions[150] which in NLO are defined as

$$\gamma_{NS} = \frac{\alpha_S}{4\pi} \gamma_{qq}^{(0)} + \left(\frac{\alpha_S}{4\pi} \right)^2 \gamma_{NS}^{(1)\eta} , \quad \eta = \pm 1 \quad \text{(B.7)}$$

$$\gamma_{ij} = \frac{\alpha_S}{4\pi} \gamma_{ij}^{(0)} + \left(\frac{\alpha_S}{4\pi} \right)^2 \gamma_{ij}^{(1)} , \quad i,j = q,g \quad \text{(B.8)}$$

where we suppressed the n-dependence. The non-singlet (NS) densities evolve according to[39,150]

$$\Delta q_{NS}^{\eta}(Q^2) = \left[1 + \frac{\alpha_S(Q^2) - \alpha_S(Q_0^2)}{4\pi} \left(\frac{\gamma_{NS}^{(1)\eta}}{2\beta_0} - \frac{\beta_1 \gamma_{qq}^{(0)}}{2\beta_0^2} \right) \right] \cdot \left(\frac{\alpha_S(Q^2)}{\alpha_S(Q_0^2)} \right)^{\gamma_{qq}^{(0)}/(2\beta_0)} \Delta q_{NS}^{\eta}(Q_0^2) , \quad \text{(B.9)}$$

where Q_0^2 is the input scale ($Q_0^2 = 0.34$ GeV^2 in our case). The distribution $\Delta q_{NS}^{\eta=+1}$ corresponds to the polarized valence quark distributions $\Delta u_V(x,Q^2) = \delta u - \delta \bar{u}$ and $\Delta d_V(x,Q^2) = \delta d - \delta \bar{d}$, and $\Delta q_{NS}^{\eta=+1}$ corresponds to the $SU(3)_{\text{flavor}}$ non-singlet

combinations $\Delta q_3(x,Q^2) = \Delta u(x,Q^2) - \Delta d(x,Q^2)$ and $\Delta q_8(x,Q^2) = \Delta u(x,Q^2) + \Delta d(x,Q^2) - 2\Delta s(x,Q^2)$ (that is opposite to the situation with the unpolarized parton distributions[150]).

The NLO evolution in the flavor singlet sector

$$\Gamma(Q^2) \equiv \begin{pmatrix} \Delta\Sigma(Q^2) \\ \Delta G(Q^2) \end{pmatrix} \tag{B.10}$$

where $\Delta\Sigma = \Delta u + \Delta d + \Delta s$, is given by[39,150]

$$\begin{aligned} \Gamma(Q^2) \;=\; & \left\{ \left(\frac{\alpha_S(Q^2)}{\alpha_S(Q_0^2)}\right)^{\lambda_-/(2\beta_0)} \left[P_- - \frac{1}{2\beta_0}\frac{\alpha_S(Q_0^2)-\alpha_S(Q^2)}{4\pi} P_-\gamma P_- \right.\right. \\ & \left.\left. - \left(\frac{\alpha_S(Q_0^2)}{4\pi} - \frac{\alpha_S(Q^2)}{4\pi}\left(\frac{\alpha_S(Q^2)}{\alpha_S(Q_0^2)}\right)^{(\lambda_+-\lambda_-)/(2\beta_0)} \right) \frac{P_-\gamma P_+}{2\beta_0+\lambda_+-\lambda_-} \right] \right. \\ & \left. +(+ \Leftrightarrow -) \right\} . \end{aligned} \tag{B.11}$$

The miscellaneous quantities are

$$\gamma = \gamma^{(1)} - \frac{\beta_1}{\beta_0}\gamma^{(0)} \tag{B.12}$$

$$P_\pm = \pm\frac{1}{\lambda_+-\lambda_-}\left(\gamma^{(0)} - \lambda_\mp \mathbb{I}\right) \tag{B.13}$$

$$\lambda_\pm = \frac{1}{2}\left(\gamma_{qq}^{(0)} + \gamma_{GG}^{(0)} \pm \sqrt{(\gamma_{GG}^{(0)} - \gamma_{qq}^{(0)})^2 + 4\gamma_{qG}^{(0)}\gamma_{Gq}^{(0)}} \right) , \tag{B.14}$$

where $\lambda_\pm$ are the eigenvalues of the leading order anomalous dimension matrix $\gamma_{ij}^{(0)}$, and $\mathbb{I}$ is the identity matrix.

In all equations above, the strong coupling constant is defined by the two-loop expression[20]

$$\frac{\alpha_S(Q^2)}{4\pi} = \frac{1}{\beta_0 \ln(Q^2/\Lambda_{(f)}^2)} - \frac{\beta_1}{\beta_0^3}\frac{\ln\left(\ln(Q^2/\Lambda_{(f)}^2)\right)}{\left(\ln(Q^2/\Lambda_{(f)}^2)\right)^2} \tag{B.15}$$

where the coefficients of the QCD beta function are $\beta_0 = 11 - 2f/3$ and $\beta_1 = 102 - 38f/3$. The number of active flavors f in $\alpha_S(Q^2)$ is determined by the number

of quarks with $m_q^2 \leq Q^2$. The QCD parameters $\Lambda_{(f)}$ are determined by the matching condition at the quark threshold

$$\alpha_S(m_q^2, f) = \alpha_S(m_q^2, f+1) \, . \tag{B.16}$$

Thus, the derivative of α_S is discontinuous across the quark threshold in this approach. Since the coefficients β depend on the number of active flavors f, the evolution is done in steps: for $m_c^2 < Q^2 < m_b^2$ we first evolve the parton densities with $f = 3$ to the charm threshold, and then from the charm threshold to Q^2 (we would go first to m_b^2 if $Q^2 > m_b^2$).

In all equations above, the leading order (LO) results could be obtained by dropping higher order terms $(\beta_1, \gamma^{(1)}, C_{q,G}^{(1)})$.

Given the moments of the structure function $g_1(n)$, the structure function in the Bjorken x space is obtained by the inverse Mellin transform

$$g_1(x) = \frac{1}{2\pi i} \int_{c-i\infty}^{c+i\infty} dn \; x^{-n} g_1(n) \, , \tag{B.17}$$

where c is the real number that has to be chosen in such a way that $\int_0^1 dx \; x^{c-1} g_1(x)$.[163] Thus, c has to lie to the right of the rightmost singularity $n_{\max}$ of $g_1(n)$ in the complex n space. The contour of integration $\mathbf{C_0}$ in Eq. (B.17) is shown in Fig. B.1. Also shown is a deformed contour $\mathbf{C_1}$ that yields the same result since all singularities for the structure functions (denoted by crosses in Fig. B.1) are on the real axis. Converting to the integration over a real variable, we get

$$g_1(x, Q^2) = \frac{1}{\pi} \int_0^\infty dz \; Im \left(e^{i\phi} x^{-c-ze^{i\phi}} g_1(n = c + ze^{i\phi}, Q^2) \right) \, . \tag{B.18}$$

We take $c = 2.1$ and $\phi = 1.9$, and the limit of integration in Eq. (B.18) is 10. These parameters have been found to give stable results for $x > 10^{-4}$. We approximate the integral in Eq. (B.18) by the 24-point Gauss-Legendre quadrature formula using a CERN program library routine RGQUAD.[164]

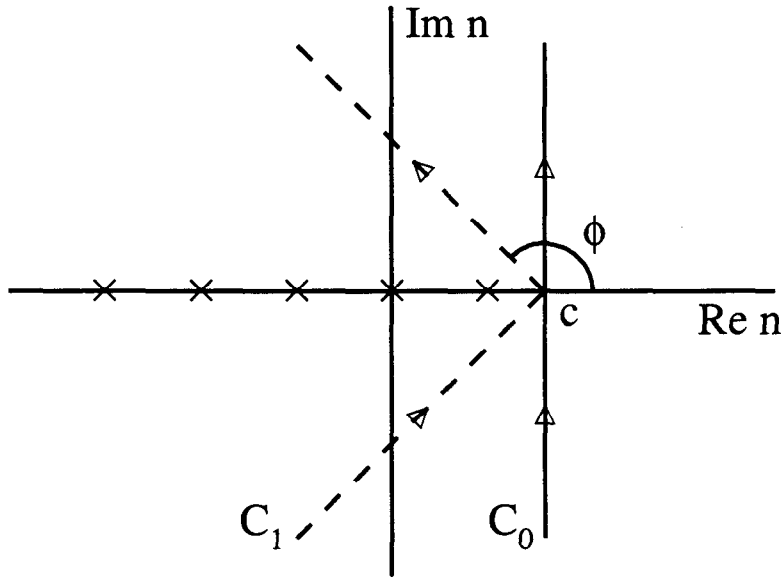

Fig. B.1. The integration contours used for the inverse Mellin transform in Equations (B.17) and (B.18). The singularities of the structure function g_1 are denoted by crosses on the real axis.

The LO spin-dependent anomalous dimensions are given by[43]

$$\begin{aligned}
\gamma_{qq}^{(0)}(n) &= 4C_F\left[2S_1(n) - \frac{1}{n(n+1)} - \frac{3}{2}\right] \\
\gamma_{qG}^{(0)}(n) &= -8T_f\,\frac{n-1}{n(n+1)} \\
\gamma_{Gq}^{(0)}(n) &= -4C_F\,\frac{n+2}{n(n+1)} \\
\gamma_{GG}^{(0)}(n) &= 4C_A\left[2S_1(n) - \frac{4}{n(n+1)} - \frac{11}{6}\right] + \frac{8}{3}T_f\,,
\end{aligned} \tag{B.19}$$

where we take $N_f = 3$ for the number of active flavors. The Casimir invariant for the adjoint representation of $SU(3)_{\text{flavor}}$ $C_A = 3$. Note that $\gamma_{NS}^{(0)}(n) = \gamma_{qq}^{(0)}(n) = \tilde{\gamma}_{qq}^{(0)}(n)$, where the $\tilde{\gamma}_{qq}^{(0)}(n)$ is the spin-averaged anomalous dimension. Thus, in the leading order, the moments of the polarized and unpolarized non-singlet distributions evolve identically, and the ratio g_1/F_1 is almost independent of Q^2 at high x where the non-singlet densities dominate. For the first $n = 1$ moment we have $\gamma_{qq}^{(0)}(1) = \gamma_{qG}^{(0)}(1) = 0$ as a consequence of helicity conservation at the quark-gluon vertex, so the first moments of the quark distributions are conserved in the leading order.

The spin-dependent NLO anomalous dimensions in the non-singlet sector $\gamma_{NS}^{\eta}(n)$ are the same as in the spin-averaged case. In the $\overline{\rm MS}$ scheme, they are given by[38]

$$\begin{aligned}
\gamma_{NS}^{(1)\,\eta}(n) = \quad & C_F^2 \quad \left[\frac{16S_1(n)(2n+1)}{n^2(n+1)^2} + 24S_2(n) + 64\tilde{S}(n,\eta) - 8S_3'(n/2,\eta) - 3 + \right. \\
& \left. 16\left(2S_1(n) - \frac{1}{n+1}\right)(S_2(n) - S_2'(n/2,\eta)) - \right. \\
& \left. 8\frac{3n^3+n^2-1+2\eta(2n^2+2n+1)}{n^3(n+1)^3}\right] + \\
& C_F C_A \quad \left[\frac{536}{9}S_1(n) - 8\left(2S_1(n) - \frac{1}{n(n+1)}\right)(2S_2(n) - S_2'(n/2,\eta)) - \right. \\
& \left. \frac{88}{3}S_2(n) - 32\tilde{S}(n,\eta) + 4S_3'(n/2,\eta) - \frac{17}{3} - \right. \\
& \left. \frac{\frac{4}{9}(151n^4+236n^3+88n^2+3n+18) - 8\eta(2n^2+2n+1)}{n^3(n+1)^3}\right] + \\
& C_F T_f \quad \left[-\frac{160}{9}S_1(n) + \frac{32}{3}S_2(n) + \frac{4}{3} + \frac{16}{9}\frac{11n^2+5n-3}{n^2(n+1)^2}\right] . \qquad \text{(B.20)}
\end{aligned}$$

Note that for $\eta = -1$, the first moment of the non-singlet anomalous dimension vanishes ($\gamma_{NS}^{(1)\,\eta=-1}(n=1) = 0$), therefore the matrix elements Δq_3 and Δq_8 are independent of Q^2 (the the flavor non-singlet axial current is conserved).

The NLO flavor singlet anomalous dimensions in the $\overline{\rm MS}$ scheme are given by[37]

$$\gamma_{qq}^{(1)}(n) = \gamma_{NS}^{(1)\,\eta=-1}(n) + 16C_F T_f \frac{n^4+2n^3+2n^2+5n+2}{n^3(n+1)^3} , \qquad \text{(B.21)}$$

where $\gamma_{NS}^{(1)\,\eta=-1}(n)$ are given by Eq. (B.20). Other elements of the two-loop anomalous dimension matrix are

$$\begin{aligned}
\gamma_{qG}^{(1)}(n) = \quad & 8C_F T_f \quad \left[2\frac{n-1}{n(n+1)}\left(S_2(n) - S_1^2(n)\right) + 4\frac{n-1}{n^2(n+1)}S_1(n) - \right. \\
& \left. \frac{5n^5+5n^4-10n^3-n^2+3n-2}{n^3(n+1)^3}\right] + \\
& 16C_A T_f \quad \left[\frac{n-1}{n(n+1)}\left(-S_2(n) + S_2'(n/2,-1) + S_1^2(n)\right) - \right. \\
& \left. \frac{4}{n(n+1)^2}S_1(n) - \frac{n^5+n^4-4n^3+3n^2-7n-2}{n^3(n+1)^3}\right] \qquad \text{(B.22)} \\
\gamma_{Gq}^{(1)}(n) = \quad & 32C_F T_f \quad \left[-\frac{n+2}{3n(n+1)}S_1(n) + \frac{5n^2+12n+4}{9n(n+1)^2} + \right] +
\end{aligned}$$

$$
\begin{aligned}
& 4C_F^2 \quad \left[2\frac{n+2}{n(n+1)}\left(S_2(n)+S_1^2(n)\right)-2\frac{3n^2+7n+2}{n(n+1)^2}S_1(n)+\right. \\
& \left.\frac{9n^5+30n^4+24n^3-7n^2-16n-4}{n^3(n+1)^3}\right]+ \\
& 8C_AC_F \quad \left[\frac{n+2}{n(n+1)}\left(-S_2(n)+S_2'(n/2,-1)-S_1^2(n)\right)+\right. \\
& \frac{11n^2+22n+12}{3n^2(n+1)}S_1(n)- \\
& \left.\frac{76n^5+271n^4+254n^3+41n^2+72n+36}{9n^3(n+1)^3}\right] \qquad \text{(B.23)} \\
\gamma_{GG}^{(1)}(n) = \quad & 8C_FT_f \quad \left[\frac{n^6+3n^5+5n^4+n^3-8n^2+2n+4}{n^3(n+1)^3}\right]+ \\
& 32C_AT_f \quad \left[-\frac{5}{9}S_1(n)+\frac{3n^4+6n^3+16n^2+13n-3}{9n^2(n+1)^2}\right]+ \\
& 4C_A^2 \quad \left[-S_3'(n/2,-1)-4S_1(n)S_2'(n/2,-1)+8\tilde{S}(n,-1)+\right. \\
& \frac{8}{n(n+1)}S_2'(n/2,-1)+ \\
& 2\frac{67n^4+134n^3+67n^2+144n+72}{9n^2(n+1)^2}S_1(n)- \qquad \text{(B.24)} \\
& \left.\frac{48n^6+144n^5+469n^4+698n^3+7n^2+258n+144}{9n^3(n+1)^3}\right]
\end{aligned}
$$

The finite sums $S_k(n)$, $S_k'(n/2,\eta)$, and $\tilde{S}(n,\eta)$ used in the expressions above are defined as[86,150]

$$
\begin{aligned}
S_k(n) &\equiv \sum_{j=1}^{n}\frac{1}{j^k} \qquad \text{(B.25)} \\
S_k'(n/2,\eta) &\equiv 2^{k-1}\sum_{j=1}^{n}\frac{1+(-)^j}{j^k} \\
&= \frac{1}{2}(1+\eta)S_k\left(\frac{n}{2}\right)+\frac{1}{2}(1-\eta)S_k\left(\frac{n-1}{2}\right) \qquad \text{(B.26)} \\
\tilde{S}(n,\eta) &\equiv \sum_{j=1}^{n}\frac{(-)^j}{j^2}S_1(j) \\
&= -\frac{5}{8}\zeta(3)+\eta\left[\frac{S_1(n)}{n^2}+\frac{\zeta(2)}{2}G(n)+\int_0^1 dx\ x^{n-1}\frac{\mathrm{Li}_2(x)}{1+x}\right], \qquad \text{(B.27)}
\end{aligned}
$$

where $G(n) \equiv \psi\left(\frac{n+1}{2}\right)-\psi\left(\frac{n}{2}\right)$, $\mathrm{Li}_2(x) = -\int_0^x dz\ \ln(1-z)/z$ is the Dilogarithm function, and $\eta = \pm 1$ for the non-singlet anomalous dimensions $\gamma_{NS}^{(1)\ \eta=\pm 1}(n)$, and

$\eta = -1$ for the flavor singlet anomalous dimensions $\gamma_{ij}^{(1)}$.

The analytical continuations of the finite sums for complex n, required for the inverse Mellin transform, are given by[150]

$$S_1(n) = \gamma_E + \psi(n+1), \quad \gamma_E = 0.577216 \tag{B.28}$$

$$S_2(n) = \zeta(2) - \psi'(n+1), \quad \zeta(2) = \pi^2/6 \tag{B.29}$$

$$S_3(n) = \zeta(3) + \psi''(n+1), \quad \zeta(3) = 1.202057\,. \tag{B.30}$$

The functions $\psi^{(k)}(n) = d^{(k+1)} \ln\Gamma(n)/dn^{(k+1)}$ can be sufficiently accurately expressed by the following asymptotic sums valid for $Re\ n \geq 10$[150]:

$$\psi(n) \approx \ln(n) - \frac{1}{2n} - \frac{1}{12n^2} + \frac{1}{120n^4} - \frac{1}{256n^6} \tag{B.31}$$

$$\psi' \approx \frac{1}{n} + \frac{1}{2n^2} + \frac{1}{6n^3} - \frac{1}{30n^5} + \frac{1}{42n^7} - \frac{1}{30n^9} \tag{B.32}$$

$$\psi'' \approx -\frac{1}{n^2} - \frac{1}{n^3} - \frac{1}{2n^4} + \frac{1}{6n^6} - \frac{1}{6n^8} + \frac{3}{10n^{10}} - \frac{5}{6n^{12}}\,. \tag{B.33}$$

For $Re\ n < 10$, a recursion relation is used:

$$\psi^{(k)}(n+1) = \psi^{(k)}(n) + \frac{(-)^k\ k!}{n^{k+1}}\,. \tag{B.34}$$

Furthermore, the integral in Eq. (B.27) involving the Dilogarithm can be approximated by[150]

$$\int_0^1 dx\ x^{n-1} \frac{\mathrm{Li}_2(x)}{1+x} \approx \frac{1.010}{n+1} - \frac{0.846}{n+2} + \frac{1.155}{n+3} - \frac{1.074}{n+4} + \frac{0.550}{n+5}\,. \tag{B.35}$$

The evolution and fitting code was optimized for speed. The most time-consuming part was evaluation of the anomalous dimensions. Fortunately, since we are not varying the strong coupling constant in the fit, it only has to be done once for every point n used in the integration (the points in the quadrature formula are fixed). The matrices used in the singlet evolution (Eq. (B.11)) are calculated once for every number of flavors f. The moments of the initial parton distributions are calculated every time a parameter of the fit changes. One fit with 8 free parameters

(149 data points in the range $0.005 \leq x \leq 0.75$ and $0.95\ \text{GeV}^2 \leq Q^2 \leq 58\ \text{GeV}^2$) typically takes 3–4 min on a DEC Alpha 600 5/266 computer (that corresponds to 800-1000 iterations in MINUIT[156]).

We tested our code against the parameterizations of Ref. [86]. Using the "standard" NLO parameterization at initial $Q_0^2 = 0.34\ \text{GeV}^2$, we evolved the GRSV[86] partons to $Q^2 = 100\ \text{GeV}^2$ and compared with the output of the code provided by one of the authors.[159] The comparison is shown in Fig. B.2; two codes are in perfect agreement. In addition, we directly integrated the leading order DGLAP equations in Bjorken space evolving the structure functions by small steps in Q^2,[83,84] and found that the direct technique gave results very close to the Mellin evolution code.

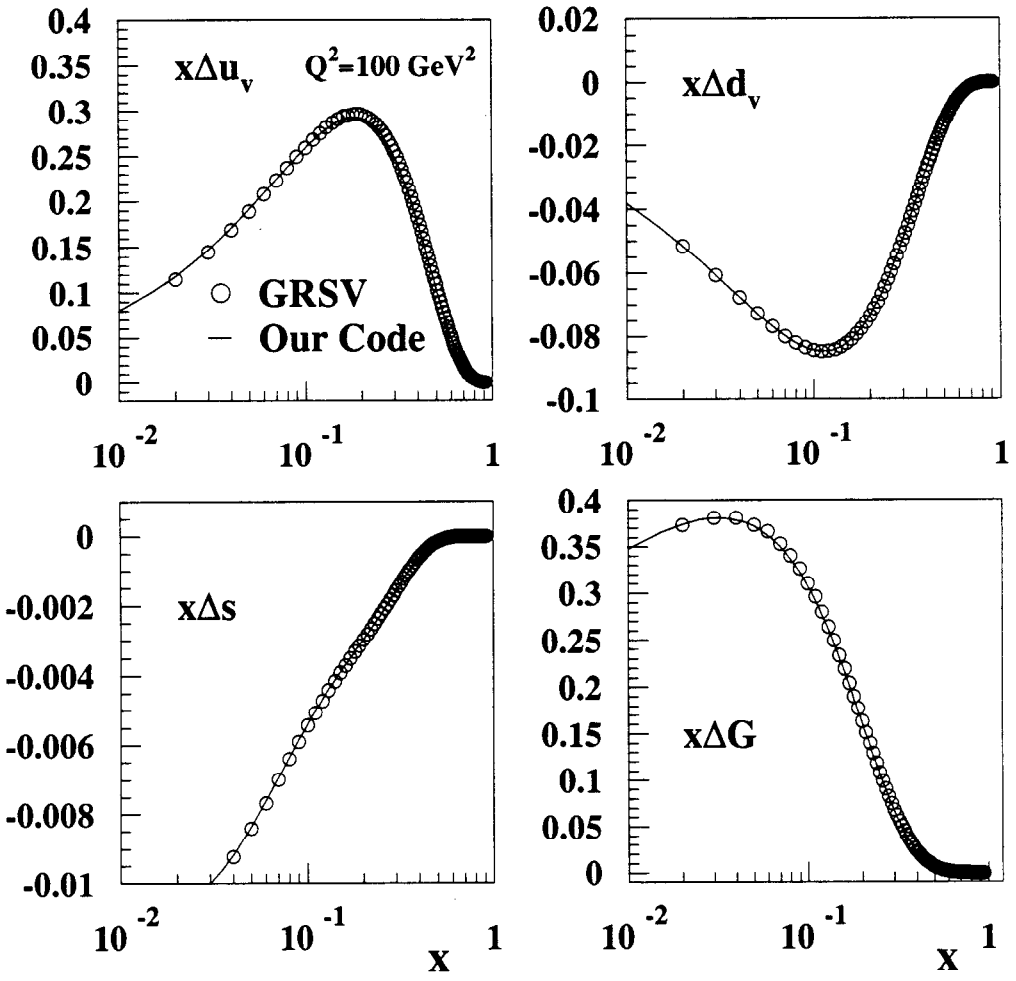

Fig. B.2. The parton distributions evolved from $Q_0^2 = 0.34$ GeV^2 to $Q^2 = 100$ GeV^2 are compared to the output of the GRSV code.[86,159]

APPENDIX C

RESULTS OF THE CALTECH ANALYSIS

The results for the structure functions and the photon-nucleon asymmetries, averaged between the two analyses, were given Chapter 4. For completeness, we will summarize here the results of the Caltech analysis.

Table C.1. The spin dependent structure function g_1^n and the photon-nucleon asymmetry A_1^n.

$\langle x \rangle$	$\langle Q^2 \rangle$ (GeV^2)	$g_1^n \pm$ stat. $\pm$ syst.	$A_1^n \pm$ stat. $\pm$ syst.
		2.75° spectrometer	
0.017	1.21	$-0.371 \pm 0.115 \pm 0.105$	$-0.061 \pm 0.019 \pm 0.017$
0.024	1.59	$-0.387 \pm 0.071 \pm 0.062$	$-0.082 \pm 0.015 \pm 0.014$
0.035	2.05	$-0.310 \pm 0.061 \pm 0.038$	$-0.083 \pm 0.018 \pm 0.012$
0.049	2.57	$-0.201 \pm 0.041 \pm 0.021$	$-0.084 \pm 0.016 \pm 0.009$
0.078	3.32	$-0.123 \pm 0.031 \pm 0.013$	$-0.081 \pm 0.019 \pm 0.010$
0.123	4.09	$-0.070 \pm 0.030 \pm 0.009$	$-0.081 \pm 0.031 \pm 0.010$
0.173	4.63	$-0.082 \pm 0.033 \pm 0.009$	$-0.123 \pm 0.052 \pm 0.016$
0.241	5.09	$-0.057 \pm 0.027 \pm 0.007$	$-0.096 \pm 0.075 \pm 0.019$
0.340	5.51	$-0.001 \pm 0.035 \pm 0.004$	$-0.256 \pm 0.197 \pm 0.071$
0.423	5.82	$0.024 \pm 0.059 \pm 0.006$	$0.133 \pm 0.606 \pm 0.034$
		5.5° spectrometer	
0.057	4.03	$0.234 \pm 0.280 \pm 0.036$	$0.047 \pm 0.118 \pm 0.012$
0.084	5.47	$-0.149 \pm 0.029 \pm 0.019$	$-0.103 \pm 0.017 \pm 0.013$
0.123	7.23	$-0.112 \pm 0.016 \pm 0.012$	$-0.107 \pm 0.015 \pm 0.012$
0.172	8.94	$-0.053 \pm 0.015 \pm 0.007$	$-0.079 \pm 0.023 \pm 0.010$
0.242	10.71	$-0.039 \pm 0.011 \pm 0.005$	$-0.109 \pm 0.030 \pm 0.015$
0.342	12.55	$-0.011 \pm 0.012 \pm 0.004$	$-0.031 \pm 0.065 \pm 0.021$
0.442	13.83	$-0.012 \pm 0.011 \pm 0.003$	$-0.091 \pm 0.139 \pm 0.020$
0.564	15.00	$0.002 \pm 0.008 \pm 0.001$	$0.083 \pm 0.279 \pm 0.031$

Table C.2. The spin dependent structure function g_2^n and the photon-nucleon asymmetry A_2^n.

$\langle x \rangle$	$\langle Q^2 \rangle$ (GeV^2)	$g_2^n \pm$ stat. $\pm$ syst.	$A_2^n \pm$ stat. $\pm$ syst.
		2.75° spectrometer	
0.017	1.21	$6.523 \pm 15.214 \pm 2.145$	$0.030 \pm 0.074 \pm 0.010$
0.024	1.59	$-1.479 \pm 7.232 \pm 0.993$	$-0.015 \pm 0.056 \pm 0.008$
0.035	2.05	$-9.065 \pm 4.890 \pm 1.042$	$-0.122 \pm 0.064 \pm 0.014$
0.049	2.57	$4.559 \pm 2.504 \pm 0.540$	$0.098 \pm 0.056 \pm 0.012$
0.078	3.32	$1.520 \pm 1.330 \pm 0.254$	$0.068 \pm 0.065 \pm 0.013$
0.123	4.09	$1.033 \pm 0.952 \pm 0.229$	$0.107 \pm 0.106 \pm 0.026$
0.173	4.63	$0.097 \pm 0.794 \pm 0.145$	$0.003 \pm 0.176 \pm 0.032$
0.241	5.09	$-0.388 \pm 0.490 \pm 0.097$	$-0.207 \pm 0.229 \pm 0.046$
0.340	5.51	$0.787 \pm 0.442 \pm 0.197$	$0.919 \pm 0.522 \pm 0.161$
0.423	5.82	$0.050 \pm 0.580 \pm 0.020$	$0.177 \pm 1.414 \pm 0.041$
		5.5° spectrometer	
0.057	4.03	$43.265 \pm 31.639 \pm 4.648$	$0.997 \pm 0.727 \pm 0.107$
0.084	5.47	$4.362 \pm 2.377 \pm 0.455$	$0.173 \pm 0.098 \pm 0.018$
0.123	7.23	$0.459 \pm 0.987 \pm 0.199$	$0.028 \pm 0.079 \pm 0.016$
0.172	8.94	$0.214 \pm 0.711 \pm 0.150$	$0.025 \pm 0.110 \pm 0.023$
0.242	10.71	$0.362 \pm 0.396 \pm 0.094$	$0.107 \pm 0.132 \pm 0.030$
0.342	12.55	$-0.136 \pm 0.299 \pm 0.032$	$-0.128 \pm 0.263 \pm 0.028$
0.442	13.83	$-0.059 \pm 0.228 \pm 0.014$	$-0.157 \pm 0.506 \pm 0.029$
0.564	15.00	$-0.011 \pm 0.125 \pm 0.009$	$-0.062 \pm 0.904 \pm 0.059$

Table C.3. Results on A_1^n and g_1^n at the measured Q^2, along with g_1^n evaluated at $Q^2 = 5$ (GeV)^2 assumin scales with Q^2. The data of two spectrometers have been averaged.

x bin	$\langle x \rangle$	$\langle Q^2 \rangle$ GeV^2	$g_1^n \pm$ stat. $\pm$ syst.	$A_1^n \pm$ stat. $\pm$ syst.	$g_1^n \pm$ sta ($Q^2 =$
0.014 – 0.02	0.017	1.2	$-0.371 \pm 0.115 \pm 0.105$	$-0.061 \pm 0.019 \pm 0.017$	-0.524 ± 0
0.02 – 0.03	0.024	1.6	$-0.387 \pm 0.071 \pm 0.064$	$-0.082 \pm 0.015 \pm 0.014$	-0.499 ± 0
0.03 – 0.04	0.035	2.0	$-0.310 \pm 0.061 \pm 0.040$	$-0.083 \pm 0.018 \pm 0.012$	-0.369 ± 0
0.04 – 0.06	0.049	2.6	$-0.192 \pm 0.040 \pm 0.021$	$-0.082 \pm 0.016 \pm 0.009$	-0.215 ± 0
0.06 – 0.10	0.081	4.5	$-0.137 \pm 0.021 \pm 0.016$	$-0.093 \pm 0.013 \pm 0.011$	-0.140 ± 0
0.10 – 0.15	0.123	6.6	$-0.103 \pm 0.014 \pm 0.011$	$-0.102 \pm 0.014 \pm 0.011$	-0.101 ± 0
0.15 – 0.20	0.173	8.2	$-0.058 \pm 0.014 \pm 0.007$	$-0.086 \pm 0.021 \pm 0.011$	-0.057 ± 0
0.20 – 0.30	0.242	9.8	$-0.041 \pm 0.011 \pm 0.005$	$-0.107 \pm 0.027 \pm 0.016$	-0.042 ± 0
0.30 – 0.40	0.342	11.7	$-0.010 \pm 0.011 \pm 0.004$	$-0.054 \pm 0.062 \pm 0.021$	-0.011 ± 0
0.40 – 0.50	0.441	13.4	$-0.011 \pm 0.011 \pm 0.002$	$-0.080 \pm 0.136 \pm 0.019$	-0.013 ± 0
0.50 – 0.70	0.564	15.0	$0.002 \pm 0.008 \pm 0.001$	$0.083 \pm 0.279 \pm 0.031$	0.004 ± 0

References

[1] E. D. Bloom *et al.*, *Phys. Rev. Lett.* **23** (1969) 930;
M. Breidenback *et al.*, *Phys. Rev. Lett.* **23** (1969) 935.

[2] CERN Courier, Volume 30, number 9 (December 1990) 1.

[3] R. P. Feynman, *Phys. Rev. Lett.* **23** (1969) 1415.

[4] J. D. Bjorken, *Phys. Rev.* **D1** (1970) 1376.

[5] J. D. Bjorken and E. A. Paschos, *Phys. Rev.* **185** (1969) 1975.

[6] The E80 Collaboration, M. J. Alguard *et al.*, *Phys. Rev. Lett.* **37** (1976) 1258, *Phys. Rev. Lett.* **37** (1976) 1261, *Phys. Rev. Lett.* **41** (1978) 70.

[7] G. Baum *et al.*, *Phys. Rev. Lett.* **51** (1983) 1135.

[8] The EMC Collaboration, J. Ashman *et al.*, *Phys. Lett.* **B206** (1988) 364, *Nucl. Phys.* **B328** (1990) 1;
V. Hughes *et al.*, *Phys. Lett.* **B212** (1988) 511.

[9] The E142 Collaboration, P. L. Anthony *et al.*, *Phys. Rev. Lett.* **71** (1993) 959; *Phys. Rev.* **D54** (1996) 6620.

[10] The E143 Collaboration, K. Abe *et al.*, *Phys. Rev. Lett.* **74** (1995) 346.

[11] The E143 Collaboration, K. Abe *et al.*, *Phys. Rev. Lett.* **75** (1995) 25.

[12] The SMC Collaboration, D. Adams *et al.*, *Phys. Lett.* **B329** (1994) 399.

[13] The SMC Collaboration, B. Adeva *et al.*, *Phys. Lett.* **B302** (1993) 533;
D. Adams *et al.*, *Phys. Lett.* **B357** (1995) 248;
CERN-PPE/97-008 (1997).

[14] The E154 Proposal, E. W. Hughes *et al.*, October 1993, unpublished.

[15] F. E. Close, *An Introduction to Quarks and Partons*, Academic Press (1979).

[16] E. Rutherford, *Phil. Mag.* **21** (1911) 669.

[17] T. Pussieux and R. Windmolders, in *Internal Spin Structure of the Nucleon*, ed. V. W. Hughes and C. Cavata, World Scientific (1995).

[18] E. Leader and E. Predazzi, *An Introduction to Gauge Theories and the New Physics*, Cambridge University Press (1985).

[19] D. J. Gross and F. Wilczek, *Phys. Rev.* **D9** (1974) 980.

[20] Review of Particle Properties, Particle Data Group (R. M. Barnett *et al.*), *Phys. Rev.* **D55** (1996) 1.

[21] M. Bourquin *et al.*, *Z. Phys.* **C21** (1983) 27.

[22] The E143 Collaboration, K. Abe *et al.*, *Phys. Rev. Lett.* **76** (1996) 587.

[23] The SMC Collaboration, B. Adeva *et al.*, *Phys. Lett.* **B336** (1994) 125.

[24] See, for example, R. L. Jaffe and A. Manohar, *Nucl. Phys.* **B337** (1990) 509; S. J. Brodsky, J. Ellis, and M. Karliner, *Phys. Lett.* **B206** (1988) 309.

[25] X. Ji, MIT-CTP-2517, hep-ph/9603249 (1996).

[26] J. D. Bjorken, *Phys. Rev.* **148** (1966) 1467; *Phys. Rev.* **D1** (1970) 1376.

[27] J. Kodaira *et al.*, *Phys. Rev.* **D20** (1979) 627, *Nucl. Phys.* **B159** (1979) 99.

[28] S. G. Gorishny and S. A. Larin, *Phys. Lett.* **B172** (1986) 109; S. A. Larin and J. A. M. Vermaseren, *Phys. Lett.* **B259** (1991) 345.

[29] J. Ellis and R. Jaffe, *Phys. Rev.* **D9** (1974) 1444.

[30] J. Ellis and M. Karliner, *Phys. Lett.* **B313** (1993) 131.

[31] H. Burkhardt and W. N. Cottingham, *Ann. Phys.* **56** (1970) 453.

[32] B. L. Ioffe, V. A. Khoze and L. N. Lipatov, *Hard Processes*, **Vol.1** (North-Holland, Amsterdam, 1984).

[33] T. P. Cheng and W. K. Tung, *Phys. Rev. Lett.* **24** (1970) 851.

[34] J. B. Bronzan *et al.*, *Phys. Rev.* **157** (1967) 1448;
H. D. I. Abarbanel *et al.*, *Phys. Rev.* **160** (1967) 1239;
V. Singh, *Phys. Rev. Lett.* **18** (1967) 36;
A. Mueller and L. Trueman, *Phys. Rev.* **160** (1967) 1296.

[35] R. L. Jaffe and X. Ji, *Phys. Rev.* **D43** (1991) 724.

[36] S. Wandzura and F. Wilczek, *Phys. Lett.* **B172** (1977) 195.

[37] R. Mertig and W.L. van Neerven, *Z. Phys.* **C70** (1996) 637;
W. Vogelsang, *Phys. Rev.* **D54** (1996) 2023 and references therein.

[38] E. G. Floratos, C. Kounnas, and R. Lacaze, *Nucl. Phys.* **B192** (1981) 417.

[39] W. Furmanski and R. Petronzio, *Z. Phys.* **C11** (1982) 293.

[40] S. J. Brodsky and G. P. Lepage, *Proceedings of the 1979 SLAC Summer Instutute on Particle Physics*, SLAC (1979).

[41] V. N. Gribov and L. N. Lipatov, *Sov. J. Nucl. Phys.* **15** (1972) 438; *Sov. J. Nucl. Phys.* **15** (1972) 675.

[42] Yu. L. Dokshitzer, *Sov. Phys. JETP* **46** (1977) 461.

[43] G. Altarelli and G. Parisi, *Nucl. Phys.* **B126** (1977) 298.

[44] T. Gehrmann and W. J. Stirling, *Phys. Lett.* **B365** (1996) 347.

[45] S. D. Drell, B. Levy, and T. M. Yan, *Phys. Rev.* **187** (1969) 2159, *Phys. Rev.* **D1** (1970) 1035, *Phys. Rev.* **D1** (1970) 1617.

[46] S. J. Brodsky and G. P. Lepage, *Phys. Rev.* **D22** (1980) 2157 and references therein.

[47] R. Blankenbecler and S. J. Brodsky, *Phys. Rev.* **D10** (1974) 2973.

[48] The E155 Proposal, R. Arnold, J. McCarthy *et al.*, October 1993, unpublished.

[49] S. J. Brodsky, M. Burkardt, and I. Schmidt, *Nucl. Phys.* **B441** (1994) 197.

[50] R. Blankenbecler and S. J. Brodsky, Ref. [47];
J. F. Gunion, *Phys. Rev.* **D10** (1974) 242;
S. J. Brodsky and G. P. Lepage, Ref. [40].

[51] J. D. Bjorken, *Phys. Rev.* **D1** (1970) 1376.

[52] E. Bloom and F. Gilman, *Phys. Rev. Lett.* **25** (1970) 1140.

[53] A. Lung *et al.*, *Phys. Rev. Lett.* **70** (1993) 718.

[54] S. J. Brodsky and G. P. Lepage, in *Perturbative Quantum Chromodynamics*, Ed. by A. H. Muller, World Scientific (1989).

[55] S. J. Brodsky, P. Hoyer, A. H. Mueller, and W. Tang, *Nucl. Phys.* **B369** (1992) 519.

[56] A.V. Efremov and O.V. Teryaev, JINR-E2-88-287 (1988); *Phys. Lett.* **B240** (1990) 200.

[57] G. Altarelli and G. Ross, *Phys. Lett.* **B212** (1988) 391.

[58] R. D. Carlitz, J.D. Collins and A.H. Mueller, *Phys. Lett.* **B214** (1988) 229. See also the comments in R.L. Jaffe and A. Manohar, *Nucl. Phys.* **B337** (1990) 509.

[59] S. D. Bass and A. W. Thomas, *Prog. Part. Nucl. Phys.* **33** (1994) 449, preprint hep-ph/9310306 (1993).

[60] T. Gehrmann and W. J. Striling, *Z. Phys.* **C65** (1995) 461.

[61] G. T. Bodwin and J. Qiu, in *Proceedings of Polarized Collider Workshop*, University Park, PA, (1990);
G. T. Bodwin and J. Qiu, *Phys. Rev.* **D41** (1990) 2755.

[62] J. Chyla, *Phys. Rev.* **D48** (1993) 4385.

[63] R. D. Ball, S. Forte, and G. Ridolfi, *Phys. Lett.* **B378** (1996) 255.

[64] A. Donnachie and P.V. Landshoff, *Phys. Lett.* **B296** (1992) 227.

[65] R. L. Heimann, *Nucl. Phys.* **B64** (1973) 429.

[66] M. Anselmino, A. Efremov, and E. Leader, *Phys. Rep.* **261** (1995) 1.

[67] J. Kuti, preprint MIT CTP #234 (1971);
J. Kuti, in *Internal Spin Structure of the Nucleon*, ed. V. W. Hughes and C. Cavata, World Scientific (1995).

[68] F. E. Close and R. G. Roberts, *Phys. Rev. Lett.* **60** (1988) 1471.

[69] R. D. Ball and S. Forte, *Phys. Lett.* **B335** (1994) 77.

[70] S. D. Bass and P. V. Landshoff, *Phys. Lett.* **B336** (1994) 537.

[71] J. Bartels, B. I. Ermolaev, and M. G. Ryskin, *Z. Phys.* **C70** (1996) 273; preprint DESY-96-025 (1996).

[72] J. L. Friar *et al.*, *Phys. Rev.* **C42** (1990) 2310.

[73] C. Coffi degli Atti *et al.*, *Phys. Rev.* **C48** (1993) 968.

[74] J. Aubert *et al.*, *Phys. Lett.* **B123** (1983) 275.

[75] M. Borghini, *Phys. Rev. Lett.* **20** (1968) 419.

[76] G. G. Petratos *et al.*, Report No. SLAC-PUB-5678 (1991), unpublished.

[77] The E143 Collaboration, K. Abe *et al.*, *Phys. Lett.* **B364** (1995) 61.

[78] J. Ellis and M. Karliner, *Phys. Lett.* **B341** (1995) 397.

[79] L. W. Whitlow *et al.*, *Phys. Lett.* **B250** (1990) 193; S. Dasu *et al.*, *Phys. Rev.* **D49** (1994) 5641.

[80] The HERMES Proposal, K. Coulter *et al.*, DESY/PRC **90-1** (1990);
M. Veltri *et al.*, Proc. Physics at HERA, Vol. 1, **447** (1991);
the HERMES Collaboration, *Technical Design Report*, July 1993.

[81] A. Simon, Proc. 12th Int. Symposium on High Energy Spin Physics, SPIN '96, Amsterdam (1996), to be published in the proceedings.

[82] J. Ellis and M. Karliner, preprint CERN-TH/95-279, hep-ph/9510402.

[83] G. Altarelli, P. Nason, and G. Ridolfi, *Phys. Lett.* **B320** (1994) 152; *ERRATUM-ibid.* **B325** (1994) 538.

[84] C. Bourrely *et al.*, preprint CPT-96-PE-3327, hep-ph/9604204.

[85] M. Gluck, E. Reya, and W. Vogelsang, *Phys. Lett.* **B359** (1995) 201.

[86] M. Gluck *et al.*, *Phys. Rev.* **D53** (1996) 4775.

[87] T. Gehrmann and W. J. Stirling, *Phys. Rev.* **D53** (1996) 6100.

[88] R. Alley *et al.*, *Nucl. Instrum. Methods* **A365** (1995) 1.

[89] M. Woods, Report No. SLAC-PUB-7320 (1996), unpublished.

[90] R. A. Erickson, E154 collaboration meeting, March 1996, unpublished.

[91] H. R. Band *et al.*, E154 Tech. Note # 40 (1996), unpublished.

[92] C. C. Young, E154 technical note # 35, unpublished.

[93] C. Møller, *Ann. Phys.* **14** (1932) 532;
J. Arrington *et al.*, *Nucl. Instrum. and Meth.* **A311** (1992) 39.

[94] H. R. Band, *AIP Conf. Proc.* **343** (1994) 245.

[95] H. R. Band and R. Prepost, E143 Technical Note # 110 (1996), unpublished.

[96] G. G. Scott and H. W. Sturner, *Phys. Rev.* **184** (1969) 490.

[97] L. G. Levchuk, *Nucl. Instrum. Methods* **A345** (1994) 496.

[98] H. Middleton, Ph. D. thesis, Princeton University (1994), unpublished.

[99] W. Happer, *Rev. Mod. Phys.* **44** (1972) 169.

[100] T. E. Chupp *et al.*, *Phys. Rev.* **C36** (1987) 2244.

[101] K. D. Bonin, T. D. Walker, and W. Happer, *Phys. Rev.* **A37** (1988) 2877;
K. P. Coulter *et al.*, *Nucl. Instrum. Methods* **A276** (1989) 29.

[102] M. V. Romalis, E154 Technical Note # 34 (1996), unpublished.

[103] M. V. Romalis and T. B. Smith, E154 Technical Note (1996), unpublished.

[104] A. Abragam, Principles of Nuclear Magnetism (Oxford University Press, New York, 1961).

[105] N. R. Newbury *et al.*, *Phys. Rev.* **A48** (1993) 558;
A. S. Barton *et al.*, *Phys. Rev.* **A49** (1994) 2766.

[106] M. V. Romalis, E154 collaboration meeting, March 1996, unpublished.

[107] G. G. Petratos, Report No. SLAC/ESA-2/93 (1993), unpublished.

[108] R. Arnold *et al.*, Report No. SLAC/ESA-4/93 (1993), unpublished.

[109] K. L. Brown, Report No. SLAC-REP-75 (1982), unpublished.

[110] J. A. Dunne, Pre-thesis project, American University, Washington, D.C. (1994), unpublished.

[111] The ASP collaboration, N. A. Roe *et al.*, *Phys. Rev.* **D41** (1990) 17.

[112] P. L Anthony and Z. M. Szalata, Report No. SLAC-PUB-7201 (1996), unpublished.

[113] J. Wang, E154 collaboration meeting, May 1996, unpublished.

[114] P. Zyla, private communication.

[115] L. Sorrell, E154 technical note # 25 (1995), unpublished.

[116] S. Incerti, E154 technical note # 30 (1996), unpublished.

[117] S. Incerti and Y. Terrien, E154 technical note # 22 (1995), unpublished.

[118] V. Breton *et al.*, *Nucl. Instrum. Methods* **A362** (1995) 478.

[119] N. V. Rabin, *Instrum. Exp. Tech.* **35** (1992) 947.

[120] Yu. Bushnin *et al.*, *Nucl. Instrum. Methods* **106** (1973) 493;
G. A. Akodopyanov *et al.*, *Nucl. Instrum. Methods* **140** (1977) 441;
F. Blanchi *et al.*, *Nucl. Instrum. Methods* **A279** (1981) 473.

[121] S. Incerti, E154 technical note # 31 (1996), unpublished.

[122] D. Kawall, Ph. D. thesis, Stanford (1995), unpublished.

[123] P. Zyla, E154 collaboration meeting, May 1996, unpublished.

[124] Yu. Kolomensky, E154 technical note # 26 (1996), unpublished.

[125] M. Olson, private communication.

[126] J. Dunne, Ph. D. thesis, American University (1995), unpublished.

[127] Yu. Kolomensky, E154 collaboration meeting, May 1996, unpublished.

[128] P. Zyla and T. Averett, E154 technical note # 43 (1996), unpublished.

[129] M. Arneodo *et al.*, *Phys. Lett.* **B364** (1995) 107.

[130] J. Gomez *et al.*, *Phys. Rev.* **D49** (1994) 4348.

[131] G. I. Smirnov, *Phys. Lett.* **B364** (1995) 87.

[132] M. Romalis, E154 technical note # 34 (1996), unpublished.

[133] I. V. Akushevich and N. M. Shumeiko, *J. Phys.* **G20** (1994) 513.

[134] I. V. Akushevich, N. M. Shumeiko and A. E. Tolkachev, POLRAD 1.5 (1996), unpublished.

[135] L. M. Stuart, private communication.

[136] D. Y. Bardin and N. M. Shumeiko, *Nucl. Phys.* **B127** (1977) 242.

[137] N. Dombey, *Rev. Mod. Phys.* **41** (1969) 236;
B. Blankleider and R. M. Woloshyn, *Phys. Rev.* **C29** (1984) 538.

[138] L. W. Mo and Y. S. Tsai, *Rev. Mod. Phys.* **41** (1969) 205;
Y. S. Tsai, SLAC-PUB-848 (1971).

[139] M. Romalis and Yu. Kolomensky, E154 technical note (1997), unpublished.

[140] D. Reyna, E154 technical note (1997), unpublished.

[141] Yu. Kolomensky and F. Sabatié, E154 technical note # 44 (1996), unpublished.

[142] F. Sabatié, E154 technical note (1996), unpublished.

[143] S. Inserti and V. Breton, E154 technical note # 36 (1996), unpublished.

[144] A. D. Martin, R. G. Roberts, and W. J. Stirling, *Phys. Lett.* **B387** (1996) 419.

[145] M. Gluck, E. Reya, and A. Vogt, *Z. Phys.* **C67** (1995) 433.

[146] J. Botts *et al.*, *Phys. Lett.* **B304** (1993) 159.

[147] T. Gehrmann and W. J. Stirling, *Phys. Rev.* **D53** (1996) 6100.

[148] H. Georgi and H. D. Politzer, *Phys. Rev.* **D9** (1974) 416;
D. J. Gross and F. Wilczek, *Phys. Rev.* **D9** (1974) 980.

[149] M. Lacombe *et al.*, *Phys. Rev.* **C21** (1980) 861;
M. J. Zuilhof and J. A. Tjon, *Phys. Rev.* **C22** (1980) 2369;
R. R. Machleid *et al.*, *Phys. Rep.* **149** (1987) 1.

[150] M. Gluck, E. Reya, and A. Vogt, *Z. Phys.* **C48** (1990) 471.

[151] G. t'Hooft and M. Veltman, *Nucl. Phys.* **B44** (1972) 189.

[152] R. Brock *et al.*, *Handbook of perturbative QCD*, *Rev. Mod. Phys.* **67** (1995) 157.

[153] S. J. Brodsky and H. J. Lu, *Phys. Rev.* **D51** (1995) 3652, and references therein.

[154] J. Kodaira, *Nucl. Phys.* **B165** (1980) 129.

[155] P. Ratcliffe, *Phys. Lett.* **B192** (1987) 309.

[156] CERN Application Software Group, *CERN Program Library Long Writeup* **D506** (1992) .

[157] See for example C. Pascaud and F. Zomer, Preprint LAL 95-05 (1995).

[158] S. Forte and G. Ridolfi, private communication.

[159] W. Vogelsang, private communication.

[160] M. A. Ahmed and G. G. Ross, *Phys. Lett.* **B56** (1975) 385;
M. B. Einhorn and J. Soffer, *Nucl. Phys.* **B74** (1986) 714.

[161] R. D. Ball, S. Forte, and G. Ridolfi, *Nucl. Phys.* **B444** (1996) 287.

[162] J. Blümlein, S. Riemersma, and A. Vogt, preprint DESY-96-131 (1996);
Nucl. Phys. Proc. Suppl. **51C** (1996) 30.

[163] D. Graudenz, M. Hampel, A. Vogt, and C. Berger, *Z. Phys.* **C70** (1996) 77.

[164] CERN Application Software Group, *CERN Program Library Short Writeup* **D107** (1992) .